

**POLITECNICO DI MILANO**  
Scuola di Ingegneria Industriale e dell'Informazione



**Development of the Effective Velocity  
Model for wind turbines aerodynamics  
numerical simulation through an  
Actuator Line approach.**

**Relatore: Prof. Alberto ZASSO**

**Co-relatore: Ing. Paolo SCHITO**

**Tesi di Laurea di:**

**Luca BERNINI, Matr. 787562**

**Corso di Laurea Magistrale in Ingegneria Meccanica**

**Matteo Maria CACCIALANZA, Matr. 783909**

**Corso di Laurea Magistrale in Ingegneria Meccanica**

**Anno Accademico 2013-2014**



## Abstract

Day by day wind energy is acquiring more and more importance in the worldwide renewables energy scenario, not only in terms of market expansion or installed capacity, but also in terms of a more accurate study of power generation devices. Among the various aspects that involve a high knowledge of a wind turbine, it is very important the ability of correctly modeling the interaction between the blades and the incoming flow, the generated loads and the evolution of the wake.

This thesis work proposes an innovative CFD model to simulate a wind turbine aerodynamics basing on the well-known Actuator Line technique, implemented in OpenFOAM. The idea of the work stems from the fact that an Actuator Line model is valid only if the algorithm estimates correctly the true generated aerodynamic forces by the turbine in the same operational conditions. For this reason, first of all it is advanced a 2-dimensional analysis of the blade section of a wind turbine, comparing the proposed model to a fully resolved airfoil simulation, checking their equivalence in terms of loads and wake. It must be noticed that the force in the Actuator Line model is smeared among the domain cells by means of a regularization kernel function. A detailed "effective velocity" model is then presented, since the key issue of the aerodynamic loads reproduction is the correct estimation of the angle of attack between the wind and the airfoil profile. Then the 2-dimensional model has been tested also in a non-steady state flow condition, showing the potential of the proposed model.

From this first version of the code, a second one is developed to simulate in a 3-dimensional computational domain the complete wind turbine rotor and its interaction with the incoming flow. To validate this model are provided comparisons between the obtained results and previous experiences made in Wind Tunnel or coming from the application of a traditional BEM approach, analyzing both the turbine performances and the generated wake.

**Keywords:** *wind energy, wind turbine loads and wake, angle of attack, CFD, OpenFOAM, Actuator Line Model, regularization kernel, Effective Velocity Model*



## Sommario

Giorno dopo giorno l'energia eolica sta acquistando sempre più importanza all'interno del panorama mondiale delle energie rinnovabili, non solo in termini di espansione dei mercati o della crescente potenza installata, ma anche nello studio sempre più accurato dei sistemi di generazione di potenza. Fra i vari aspetti che coinvolgono la conoscenza approfondita di una turbina eolica è di particolare importanza la possibilità di modellare correttamente l'interazione delle pale con il flusso incidente, i carichi nati da essa e la successiva evoluzione della scia.

Dopo aver accennato i momenti salienti dell'evoluzione dell'energia eolica nel corso della Storia, la sua posizione attuale all'interno del mercato internazionale dell'energia e le prospettive future, il primo capitolo di introduzione spiega brevemente il funzionamento di una turbina eolica. Nello specifico si tratta di turbine eoliche ad asse orizzontale, sistemi di generazione di energia elettrica che estraggono energia dal vento per mezzo della rotazione indotta alle pale, connesse fra loro per mezzo di un albero rotante orizzontalmente. Una turbina eolica è composta da una torre, in cima alla quale si trova la navicella, connessa poi tramite l'albero alle pale. L'altezza della torre è tanto più importante tanto è più in alto la velocità del vento è maggiore, mentre la lunghezza delle pale permette di spazzare aree più o meno vaste, influenzando quindi la potenza generata. Il funzionamento di una turbina eolica si basa sui dati rilevati da un anemometro posto in sommità alla torre: a partire da questi il controllore agisce come freno sulla rotazione delle pale, per mantenerle nel range di velocità ottimo, oppure modificando gli angoli di *yaw* o di *pitch*. Il primo allinea l'asse di rotazione alla direzione prevalente del vento incidente, il secondo contribuisce a modificare l'angolo di attacco della pala rispetto al vento. All'interno della navicella una trasmissione permette il collegamento dell'albero rotante a bassa velocità (quello trascinato dalle pale) a quello ad alta velocità, a cui è connesso l'alternatore per la produzione di energia elettrica.

Il lavoro di tesi propone la riproduzione del comportamento di una turbina eolica ricorrendo alla fluidodinamica computazionale (CFD), uno strumento molto utile basato sull'analisi virtuale di sistemi che possono coinvolgere fenomeni chimici, trasferimenti di calore, o come in questo caso l'evoluzione di un fluido e la sua interazione con gli oggetti circostanti. All'interno del secondo capitolo è sintetizzata la costruzione di una tipica simulazione, effettuata mediante CFD

e che essenzialmente è composta di tre parti: fase di introduttiva, detta di *pre-processing*, in cui viene disegnato l'ambiente di simulazione, caratterizzato il fluido e definiti i modelli da applicare per la simulazione; fase intermedia, *processing*, nella quale il codice CFD lavora e sviluppa i calcoli secondo gli algoritmi scelti; fase conclusiva o di *post-processing*, nella quale si analizzano i risultati ottenuti anche con l'aiuto di opzioni di visualizzazione e si operano eventualmente dei confronti con altre esperienze (ad esempio sperimentali o analitiche). In seguito vengono passate in rassegna le equazioni che governano gli algoritmi di cui è composta la CFD e quelle inerenti ai modelli di turbolenza impiegati, ovvero RANS (Reynolds Averaged Navier-Stokes equations) e LES (Large Eddy Simulations) e la loro implementazione in OpenFOAM, il programma CFD adottato, basato sul linguaggio di programmazione *C++*.

La simulazione dell'aerodinamica di una turbina eolica è un problema ancora molto aperto; al giorno d'oggi ci sono diversi approcci che condividono questo intento. Il terzo capitolo comincia presentando l'attuale stato dell'arte in questo campo: il primo classico metodo di analisi è il metodo Blade Element Momentum, un modello molto semplice per calcolare i carichi, la spinta e la potenza per diversi valori di velocità del vento, di rotazione e di angolo di *pitch*. Solo negli ultimi anni però sono stati fatti degli sforzi per lo sviluppo di nuovi modelli più raffinati, basati sulla CFD, per un'accurata riproduzione fisica dell'interazione del fluido con il rotore di una turbina a vento. Essenzialmente tre sono i diversi approcci esistenti: il modello Actuator Disk, secondo cui la turbina è modellata come una forza disposta su un disco (rappresentante del rotore), che viene aggiunta come termine sorgente nelle equazioni di Navier-Stokes; il modello Actuator Line, simile al primo, ma che distribuisce la forza su delle linee, rappresentative delle singole pale e non più dell'intera area spazzata dal rotore; l'approccio che propone una simulazione completa dell'esatta geometria della pala. In questo ultimo caso non è necessario inserire il termine di forza, poiché tutte le grandezze vengono risolte dal codice. Nel caso dei modelli di Actuator Disk ed Actuator Line, la forza inserita viene calcolata analiticamente, a partire dai coefficienti aerodinamici dei vari profili impiegati per le pale, dipendenti dall'angolo di attacco, e dal valore di velocità incidente, le cui informazioni sono ricavate per mezzo della risoluzione diretta del campo di moto ad opera del codice CFD. Ad oggi però tutte queste tecnologie presentate soffrono ancora notevoli problemi di inaccuratezza: negli ultimi anni sono stati organizzati diversi blind-test, ovvero analisi comparative della capacità

dei codici partecipanti di simulare correttamente il comportamento di modelli di turbina provati in galleria del vento. In tutti i casi generalmente è emersa una certa discrepanza fra i risultati aspettati e quelli ottenuti per via sperimentale, sia in termini di forza scambiata fra il fluido e le pale, sia in termini di scia generata dalla presenza della turbina. Il lavoro di tesi prende come base il modello Actuator Line e si propone di migliorarlo, focalizzando in particolare l'attenzione su una delle sue criticità: la stima della velocità incidente alla pala, finora probabilmente trattata con eccessiva leggerezza. Due sono i metodi impiegati correntemente: il primo è quello impiegato comunemente dal Blade Element Momentum, che sfrutta come unica informazione la velocità campionata in un punto posizionato distante e molto avanti rispetto al rotore della turbina. In caso di vento turbolento però questo metodo non risulta affidabile, portando ad un'anticipazione del carico applicato sulla pala rispetto all'effettivo impatto del fenomeno turbolento sulla pala stessa. Il secondo metodo consiste nella semplice valutazione locale del campo di velocità rispetto alla pala e del suo quasi istantaneo impiego nel calcolo della forza. Questo metodo co-localizzato non tiene conto della deflessione del flusso in prossimità dell'ostacolo, pertanto comporta un inserimento non corretto dell'angolo del vettore di velocità relativa.

Innanzitutto si presenta un'attenta validazione del modello Actuator Line in un dominio bidimensionale, considerando una sezione di pala, ovvero l'evoluzione del flusso intorno ad un profilo alare, nel caso esposto, il profilo NACA0012. Una serie di simulazioni stazionarie del profilo completamente modellato hanno costituito il riferimento per quelle ottenute mediante il modello Actuator Line, la cui linea collassa però in questo caso in un punto, detto Actuator Force. Per il profilo completo sono stati testati diversi angoli d'attacco e da sono state estratte le curve polari dei coefficienti aerodinamici  $C_L$  e  $C_D$ , verificate a loro volta con quelle ottenute per via sperimentale. Ampio studio è stato fatto anche attorno alla funzione del Regularization Kernel, un artificio matematico utile per la distribuzione della forza generata su più celle confinanti con quella effettivamente contenente il punto di applicazione della forza. Ricorrere a questo strumento è stato indispensabile per evitare la comparsa di oscillazioni spaziali nella soluzione numerica CFD. Obiettivo prefissato ed ottenuto di questa fase iniziale della tesi è ottenere una simulazione Actuator Line in dominio bidimensionale che ben riproduca la simulazione del profilo completo, in termini di scia (per cui si è campionato il campo di velocità a valle del profilo su diverse linee) e di forza generata (analizzando il campo di

pressione su cerchi di raggio diverso). Basandosi su questa similitudine, il passo successivo consiste nella definizione di un modello di velocità effettiva (Effective Velocity Model), ovvero di un modello che fosse in grado di stimare il corrispondente valore di velocità indisturbata (sia per quello che riguarda il modulo che l'angolo) a partire dalla velocità rilevata localmente rispetto al punto rappresentante l'Actuator Force. La costruzione di questo modello è riportata in dettaglio all'interno della tesi, ma sostanzialmente si tratta della disposizione di una linea di una lunghezza arbitrariamente scelta posizionata anteriormente rispetto al profilo e perpendicolarmente al flusso medio incidente, lungo la quale la velocità è campionata in un dato istante di tempo. Dal valore di velocità relativa restituito dalla linea, tramite una correzione sul valore dell'angolo, si giunge allo stimato valore indisturbato usato come input per il calcolo della forza. L'efficacia dell'Effective Velocity Model è stata dimostrata sia per il profilo analizzato NACA0012, sia nel caso di un profilo non simmetrico del tipo NACA63.4, così come la sua convenienza rispetto al modello di campionamento locale. A questo punto il passo successivo consiste nel test del modello immergendo l'Actuator Force in un regime di flusso non stazionario, osservandone ancora una volta il comportamento rispetto ad un'omologa simulazione svolta sul profilo alare completamente modellato.

Affermata e dimostrata la validità del modello bidimensionale, questo è stato trattato come base per la scrittura di un codice di simulazione del comportamento del rotore della turbina eolica ad asse orizzontale. Come spiegato in precedenza, la tecnica impiegata è quella dell'Actuator Line, per cui le pale della turbina non sono direttamente modellate all'interno del dominio computazionale, ma sono rappresentate da linee virtuali sulle quali viene distribuita la forza analiticamente calcolata. Nel caso in questione le linee sono discretizzate da punti che corrispondono alle intersezioni della griglia della mesh con la linea stessa. Ovviamente, come le pale, la posizione delle linee cambia istante dopo istante poiché il rotore sta ruotando. Considerando ciascun punto appartenente alla linea rappresentante la pala, l'applicazione della forza segue un procedimento analogo a quello esposto per l'Actuator Force, ovvero ricorrendo all'Effective Velocity Model per ogni punto ed al Regularization Kernel per la distribuzione della forza. Noto quindi il contributo delle forze di volume, le equazioni di Navier-Stokes sono poi risolte dal solutore adottato: nel caso di questa tesi ci si è basati su `pisoFoam`, ovvero l'implementazione dell'algoritmo numerico PISO in OpenFOAM. Facendo riferimento alle simulazioni prodotte l'idea è stata quella di riprodurre, per poi confrontare,



le prove effettuate nella camera veloce della Galleria del Vento del Politecnico di Milano su un modello scalato di turbina Vestas V90 3 MW, i cui risultati sono disponibili in letteratura. L'ambiente computazionale perciò riprende le dimensioni della camera di prova, un condotto a sezione quadrata di 4x4 m lungo 20 m, in cui a 5 m dall'ingresso è stato posto il rotore modellato della turbina. Esattamente come stato fatto nel caso sperimentale, sono stati testate diverse configurazioni, ad esempio facendo variare il parametro TSR (Tip Speed Ratio - definito come  $\frac{\omega R}{V_\infty}$ , dove  $\omega$  indica la velocità di rotazione,  $R$  il raggio del rotore all'estremità esterna delle pale e  $V_\infty$  il valore di velocità indisturbata del vento) oppure l'angolo di *pitch*. Per verificare la qualità del codice prodotto sono state confrontate le prestazioni di spinta e coppia del generatore eolico: quelle misurate sperimentalmente verso quelle sviluppate dai calcoli del codice. In generale si è assistito ad un buon accordo fra i dati raccolti, con errori tanto più contenuti quanto più il valore di TSR aumenta, ovvero tanto più allontanandosi dal rischio che alcuni profili alari lavorassero in condizioni di stallo. Per quello che riguarda i diversi valori di *pitch* testati, anche in questo caso vale una considerazione simile: per bassi valori di *pitch* (anche negativi) i profili alari lavorano nelle regioni stallate, così la turbina mostra chiaramente un peggioramento delle prestazioni. Un altro confronto neuralgico riguarda l'analisi della scia: si è andati a verificare una somiglianza nel profilo del deficit di velocità rispetto al valore indisturbato prodotto dalla presenza della turbina. Anche in questo caso sono rilevabili discrete somiglianze fra il caso sperimentale e quello simulato: le differenze sono da imputarsi ad una differente distribuzione delle forze lungo la pala che provoca delle leggere discrepanze fra i risultati ottenuti. Proprio per questo, dal momento che i dati di distribuzione della forza lungo la pala non erano disponibili per i casi testati in Galleria del Vento, si è pensato allora di approfondirne la conoscenza tramite un ultimo paragone, quello relativo alle simulazioni prodotte dal codice proposto nella tesi verso i risultati ottenuti per via analitica sfruttando l'approccio Blade Element Momentum. Sfruttando un dominio con sezione doppia rispetto a quello impiegato finora per ridurre il valore del rapporto di bloccaggio, sono state eseguite simulazioni con due diversi valori di TSR e si è indagata più a fondo la distribuzione della forza lungo la pala. Si nota un buon accordo fra i dati, sebbene le simulazioni mostrino una leggera sovrastima dei valori aspettati, in particolare là dove le sezioni di pala presentano valori di corda più lunghi. Si vede come in corrispondenza di queste sezioni, l'angolo di velocità rilevato e riveduto dall'Effective Velocity Model sia leggermente superiore rispetto a quello aspettato. Questo fatto mostra che la cor-

reazione proposta dell'Effective Velocity Model, mutuata dal caso bidimensionale, sembra debole e non riesca a riportare il valore d'angolo letto localmente a quello effettivo caratteristico del flusso indisturbato. Tale evidenza non compromette però la validità del modello proposto, ma suggerisce l'idea di continuare lo studio in questa direzione in particolare approfondendo uno studio tridimensionale del modello.

In conclusione, si può riassumere il lavoro di tesi come la proposta di un nuovo metodo per la simulazione del comportamento di una turbina eolica attraverso la produzione di un codice numerico funzionante e testato: sono stati ottenuti buoni risultati con ancora, ovviamente, margini di miglioramento. Oltre al miglioramento del codice, sforzi futuri vanno fatti soprattutto nello studio del moto turbolento e della simulazione della turbina in questo regime di moto.

**Parole chiave:** *energia eolica, scia e carichi delle turbine eoliche, angolo di attacco, CFD, OpenFOAM, Actuator Line Model, regularization kernel, Effective Velocity Model*





# Table of Contents

<b>1</b>	<b>Introduction</b>	<b>1</b>
1.1	Historical remarks . . . . .	1
1.2	Wind turbine overview . . . . .	6
1.3	Wind turbine operation . . . . .	8
<b>2</b>	<b>Introduction to CFD</b>	<b>13</b>
2.1	Computational Fluid Dynamics . . . . .	13
2.1.1	CFD code operation . . . . .	15
2.1.2	OpenFOAM . . . . .	18
2.2	CFD governing equations and OpenFOAM implementation . .	18
2.2.1	Governing equations . . . . .	18
2.2.2	OpenFOAM implementation of Navier-Stokes equations	20
2.3	Turbulence modeling . . . . .	21
2.3.1	Turbulence implementation in OpenFOAM . . . . .	23
<b>3</b>	<b>Wind turbine numerical simulation</b>	<b>25</b>
3.1	Turbine numerical simulation overview . . . . .	25
3.2	BEM foundation . . . . .	27
3.3	Actuator Disk Model . . . . .	31
3.4	Actuator Line Model . . . . .	34
3.5	Turbine model performance analysis . . . . .	36
3.6	Effective velocity evaluation . . . . .	44
<b>4</b>	<b>AL methods validation in 2D and Effective Velocity Model set-up</b>	<b>47</b>
4.1	2-Dimensional study of AL method . . . . .	47

4.2	FRA simulation . . . . .	49
4.2.1	Turbulence model . . . . .	50
4.2.2	Boundary definition . . . . .	51
4.2.3	Polar curves extraction . . . . .	52
4.3	AF simulation . . . . .	53
4.3.1	Regularization Kernel application . . . . .	55
4.4	Flow reproduction . . . . .	60
4.4.1	Wake reproduction . . . . .	64
4.5	Aerodynamic force estimation . . . . .	66
4.5.1	Description and tuning of the EVM . . . . .	67
4.6	Non-stationary test case . . . . .	81
4.6.1	Wind time history simulation . . . . .	81
4.6.2	Blade wind relative velocity . . . . .	83
4.6.3	FRA and AF simulation of airfoil section in oscillating inflow condition . . . . .	86
<b>5</b>	<b>Wind turbine simulation with Effective Velocity Model</b>	<b>95</b>
5.1	Wind turbine of wind tunnel . . . . .	95
5.2	OpenFOAM solver . . . . .	97
5.3	Simulation set-up . . . . .	100
5.3.1	Computational domain . . . . .	101
5.3.2	Turbulence modeling . . . . .	102
5.3.3	Turbine modeling . . . . .	103
5.3.4	Boundary and initial conditions . . . . .	104
5.4	Turbine performance analysis . . . . .	105
5.4.1	Mesh sensitivity robustness . . . . .	107
5.4.2	Turbine performance analysis under different TSR con- dition . . . . .	108
5.4.3	Turbine performance analysis under different pitch angles	110
5.5	Wake analysis . . . . .	112
5.5.1	Wake deficit . . . . .	112
5.5.2	Wake vorticity . . . . .	118
5.6	Comparison between AL solver and BEM approach . . . . .	119
5.6.1	Computational domain . . . . .	119

5.6.2 Turbine performance analysis . . . . .	121
<b>6 Conclusions and future efforts</b>	<b>127</b>
6.1 Future efforts . . . . .	129
<b>Bibliography</b>	<b>131</b>





# List of Figures

1.1	Global cumulative installed wind capacity 1996 - 2013. . . . .	3
1.2	European targets for wind energy, fuel saving, job opportunities, CO2 reductions and investments for future. . . . .	4
1.3	Large wind turbines design and construction. . . . .	5
1.4	A wind turbine complex in southern Wyoming, USA. . . . .	7
1.5	Wind turbine nacelle layout. . . . .	7
1.6	Vestas V90 power curve. . . . .	10
1.7	Definition of the aerodynamic angles on a blade section. . . . .	11
2.1	An ANSYS simulation of the airflow around the left side of the Ferrari 458 Italia. . . . .	14
2.2	The OpenFOAM logo. . . . .	18
2.3	The considered control volume. . . . .	19
2.4	Mixing effectiveness in the laminar flow and in the turbulent one. . . . .	22
3.1	Velocity over homogeneous rotor. . . . .	28
3.2	Typical blade axial load distribution. . . . .	29
3.3	BEM annular analysis. . . . .	29
3.4	The rotor force is insert in CFD cells belonging to grey area. . . . .	32
3.5	The rotor force is inserted in cells inside AD circular area. . . . .	32
3.6	Relative velocity on blade section. . . . .	33
3.9	MexNext results: loads of CFD codes. . . . .	40
3.10	MexNext results: loads of lifting line codes. . . . .	41
3.11	MexNext results: axial velocity. . . . .	42
3.12	MexNext results: turbine torque-thrust. . . . .	42

3.13	Nowitech and Norcowe Blind Test 1. . . . .	43
4.1	Turbine blade and AL blade line model. . . . .	48
4.2	Turbine blade section and AL line intersection point (AF section model). . . . .	48
4.3	NACA0012 symmetrical airfoil shape. . . . .	49
4.4	Mesh of NACA0012 profile. . . . .	50
4.5	2-dimensional case boundaries. . . . .	51
4.6	NACA0012 computed polar curves vs literature experimental data. . . . .	53
4.7	Regularization Kernel width analysis. . . . .	57
4.8	Regularization kernel distribution function and visualization in the computational domain. . . . .	59
4.9	Pressure field on surrounded contours: comparison between FRA and AF calculations. . . . .	61
4.10	AF - FRA relative velocity error. . . . .	62
4.11	AF - FRA velocity relative error. . . . .	63
4.12	AF - FRA velocity relative error. . . . .	63
4.13	A series of probe lines are placed in both FRA and AF simulation for wake comparison. . . . .	64
4.14	AF vs FRA wake analysis. . . . .	65
4.15	EVM sampling line set-up. . . . .	68
4.16	Comparison between the FRA and the AF simulations on U (magnitude and angle) function of the coordinate $s$ , detected on the line placed 1.5 m in front of the AF point. . . . .	69
4.17	Trends of the errors on U relative to the AF simulation compared to FRA. . . . .	70
4.18	Difference between $\Delta\alpha$ detected by FRA and AF simulations and their computed absolute difference function of the coordinate $q$ . . . . .	71
4.19	EVM line and AF position in the computational domain. . . . .	72
4.20	Influence of $C_L$ and $C_D$ on $\Delta\alpha$ value. . . . .	73
4.21	Minor influences of EVM: influence of chord length on $\Delta\alpha$ (a) and influence of $C_L$ and $C_D$ on the absolute value of $\mathbf{U}$ . . . . .	75

4.22	Estimation of the undisturbed AOA: the EVM is compared to the LM with a regularization kernel width $\epsilon = \sqrt{2}l_{cell}$ .	76
4.23	Estimation of the undisturbed AOA: the EVM is compared to the LM with a regularization kernel width $\epsilon = l_{cell}$ .	77
4.24	Estimation of the undisturbed AOA: the EVM is compared to the LM without regularization kernel.	77
4.25	Fluid angle sampled on an horizontal line crossing the domain.	79
4.26	AF + EVM reproduction of forces delivered by different wing profiles.	80
4.27	Eurocode terrain table.	82
4.28	Wind simulation points grid.	84
4.29	Wind simulation statistical characteristics.	84
4.30	PSD of blade incoming wind.	85
4.31	Logarithmic wind speed variation.	87
4.32	Oscillating blade angle analysis.	88
4.33	Oscillating inlet case.	90
4.34	Non stationary force with EVM.	91
4.35	Non stationary velocity with EVM.	92
4.36	Non stationary velocity with EVM.	93
4.37	Non stationary velocity with EVM.	94
5.1	Scaled model of Vestas V90 3 MW wind turbine.	96
5.2	Discretization of the blades.	98
5.3	Aerodynamic coefficients $C_L$ , $C_D$ of an airfoil of the modeled wind turbine.	100
5.4	The computational domain reproducing the high-speed duct of the Wind Tunnel at the Politecnico di Milano.	102
5.5	Turbulence generates from the blade rotation only (the rotor plane is grey highlighted) and develops in the wind turbine wake.	103
5.6	Thrust, torque and blade area PSD curves for TSR = 7 case.	107
5.7	Thrust, torque and power measured function of time, for different mesh cases.	108

5.8	Thrust and power for fixed pitch angle (0 deg) generated by the wind turbine as a function of TSR. Comparison between our solver and experimental data. . . . .	109
5.9	Thrust and power for TSR 7 generated by the wind turbine as a function of pitch angle. Comparison between our solver and experimental data. . . . .	111
5.10	Vertical profiles of axial wind velocity in the wake of the wind turbine. Simulation and experimental result are compared probing the velocity field at different distances $x/D$ downstream of the rotor. . . . .	112
5.11	Volume force cylindrical distribution. . . . .	114
5.12	Evolution of the wake downstream the rotor plane for different TSR conditions. . . . .	116
5.13	Wake detected at fixed distance values for different TSR conditions. . . . .	117
5.14	Iso-vorticity visualization of the wind turbine wake. . . . .	119
5.15	Computational domain adopted to compare our solver with BEM (red) vs the original domain reproducing the high speed duct of the Wind Tunnel (black). . . . .	120
5.16	Detected AOA for TSR = 7 simulation case. . . . .	122
5.17	Blade loads for TSR = 7 simulation case. . . . .	123
5.18	Detected AOA for TSR = 9 simulation case. . . . .	125
5.19	Blade loads for TSR = 9 simulation case. . . . .	126

# List of Tables

4.1	NACA0012 mesh characteristics . . . . .	49
4.2	FRA boundary condition . . . . .	52
4.3	NACA0012 polar curves simulation . . . . .	52
4.4	AF mesh characteristics . . . . .	54
4.5	Blade wind oscillation describing value. . . . .	89
4.6	FRA and AF oscillating boundaries. . . . .	89
4.7	FRA-AF boundary condition oscillating inlet . . . . .	90
5.1	TSR tested values and corresponding rotational and incoming flow velocities . . . . .	104
5.2	Tested TSR values and corresponding discrepancies between experimental and simulated results in terms of thrust and torque.	110
5.3	Tested pitch angles and corresponding discrepancies between experimental and simulated results in terms of thrust and torque.	111
5.4	Tested TSR values and corresponding discrepancies between BEM and simulated results in terms of thrust and torque. . .	124



# Chapter 1

## Introduction

This work wants to contribute to the modeling of the interaction of the wind turbine rotor with the incoming flow, by an innovative numerical modeling. The aim has been pursued through the development of an appropriate code (already existing in some of its parts) and then validated with a continuous comparison with a reference simulation, based on the fully discretization of a common wing profile. Ending, the validated code is used as a basis of a successive reproduction of a full-scale operating condition, in uniform flow and using the correct geometrical and aerodynamic wind turbine features.

### 1.1 Historical remarks

As it is witnessed by the ancient mythology, wind has always played an important role in the humans' life and activities. In the most ancient societies wind was seen as a divinity, that people pray, respect and sometimes fear. Anyway, does not exist people who do not make curious from the possibilities and the advantages given by the control of the wind: even if it could be defined simply as "air in motion", it is an "ever-green" challenge for people extract energy from it. Historical sources show that sailing was the first scope for wind employment, but also the extraction of energy by means of a first kind of turbine was very old. Wind turbines are known since

the 17th century B.C. when Babylon was in its golden age: they are the oldest device to capture wind energy on land and Hammurabi used them for a big irrigation project. The first application of windmills were in Sistan (Afghanistan) between the 7th and the 9th century A.D. where vertical axis wind turbines were built to grind corn and to pump water [1].

Windmills successively diffused in Asia, Middle East and Europe, as reports of European crusaders coming back home. In Europe the first horizontal axis windmills appeared in the 12th century, as an alternative to watermills, located typically on the rivers that were property of nobility and clergy, giving an important resource to the new middle class. Windmills, in addition, can work in any climate also when a very cold winter freezes the water. By the 14th century in the Netherlands windmills were fundamental to drain areas of the Rhine delta.

After the Industrial Revolution of the 18th century and through the great technological conquests of the early years of the succeeding one, the demand for electrical power for industrial purposes spread out, giving the idea of using turbines to convert wind into electrical energy. The first electricity-generating wind turbine was a battery charging machine installed in 1887 by Scottish professor J. Blyth to light his holiday cottage. Some months later American inventor Charles F. Brush built the first automatically operated wind turbine, a rotor diameter of 17m producing 12kW [2].

Wind turbines diffusion increased progressively during the 20th century: in Denmark by 1900, there were about 2500 windmills for mechanical loads such as pumps and mills, producing an estimated combined peak power of about 30MW. Around the time of World War I, American windmill makers were producing 100,000 farm windmills each year, mostly for water pumping. By the 1930s, wind generators for electricity were common on farms, mostly in the United States where distribution systems had not yet been installed. Despite these encouraging improvements, developments in fossil fuel systems almost entirely eliminated any wind turbine systems larger than micro size. In the early 1970s, however, the first oil crisis induced the world to look for alternative energy sources. The research and development of new materi-



als, technologies and engineering brought to the realization of the first multi MW wind turbine in 1978: the 54 m rotor diameter "Tvindkraft" windmill was constructed and financed by a group of schools of Tvind (Denmark), to show an alternative to nuclear power, that was at the time an attractive power source. This windmill has a quite modern design and is still working after nearly 34 years. The oil crisis lasted until 1987, when the largest wind turbines had a rotor diameter of 100m and a nominal power of 3.5MW [3]. In early 21th century global warming, fossil fuel reserves and energy security were the most important issues stimulating the interest in renewable energies. All over the world new companies formed and specialized in the construction of wind turbines and huge studies were undertaken by many universities and researchers to better understand the possibilities of profiting by wind energy and to design more powerful and more efficient turbines. Recent statistics, provided by GWEC [4] show the wind energy growth during last decades: despite the strong economical crisis of the early 2010s, wind energy industry is currently expanding: in the last years (2009-2013) all around the world were installed new turbines, for a capacity of more or less 40 GW per year.

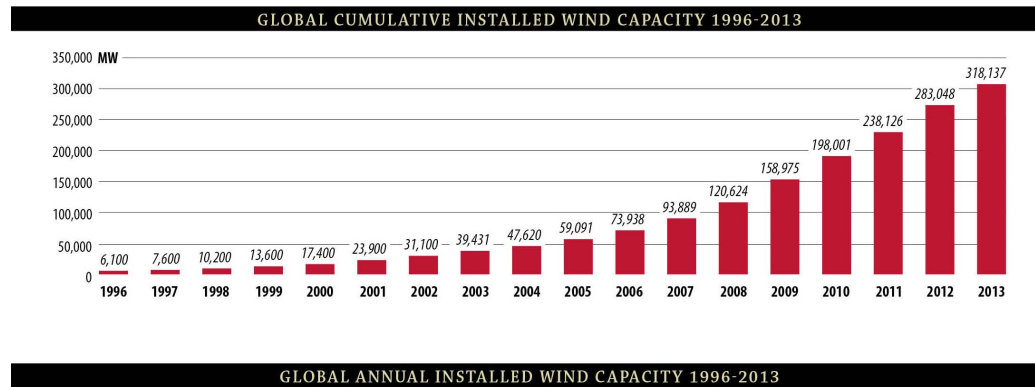


FIGURE 1.1: *Global cumulative installed wind capacity 1996 - 2013 (courtesy GWEC).*

From the global statistics of fig 1.1, trends show that the expansion will continue in the next years, even actual predictions state a bit decrease of

the grow rate. An icon of the possibilities given by the renewable sources of energy, and in particular the wind one, is represented by Denmark. Actually 30% of Denmark's electricity consumption is covered by wind energy. The Danish government aims to get 50% of its electricity from wind by 2020 and 100% from renewable energy by 2050. European countries engage themselves in an ambitious programme to reduce the dependence by fossil source of energy and to turn to renewable ones. This plan involves obviously wind energy, but other important aspects that are taken into account are environment preservation and new job opportunities [5], as briefly summarized in fig. 1.2.

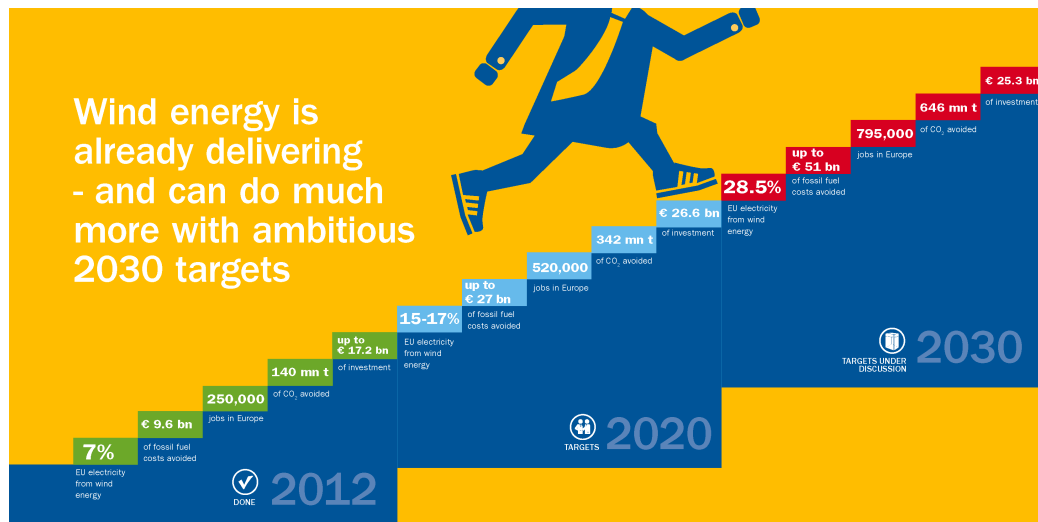


FIGURE 1.2: *European targets for wind energy, fuel saving, job opportunities, CO<sub>2</sub> reductions and investments for future (courtesy EWEA).*

By 2030 one third of European energetic need will be supplied by wind turbines and similarly it will happen around the world: more powerful wind turbines are currently under study, predictions say that in the next decades 10-20MW very large turbines will be designed (fig. 1.3), [6].

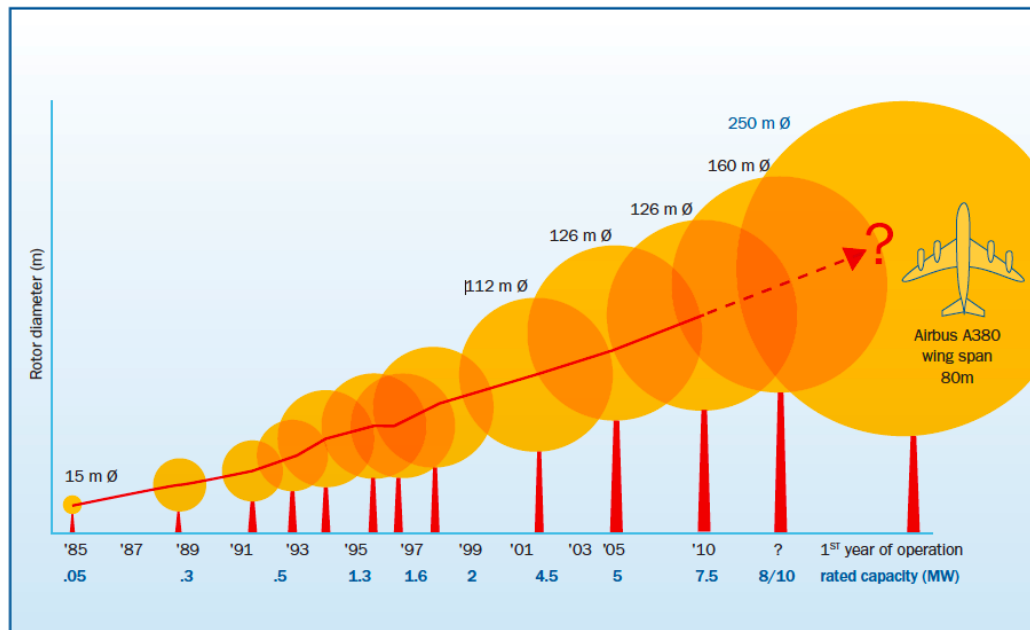


FIGURE 1.3: *Large wind turbines design and construction (courtesy EWEA).*

To reach the ambitious purposes, must be remarked also the important role that will be played by offshore wind energy production. This is a relatively new technology, which main key benefits are that the wind resource offshore is generally much greater, thus generating more energy from fewer turbines, and that most of the world's largest cities are located near a coastline. Offshore wind is suitable for large scale development near the major demand centers, avoiding the need for long transmission lines. It is reasonable to image that costs will reduce and the technology will advance, helping offshore wind to be more efficient and cost competitive in the near term. More than 90% of the world's offshore wind power is currently installed off northern Europe, in the North, Baltic and Irish Seas, and the English Channel. Most of the rest is in two "demonstration" projects off China's east coast. Offshore wind is an essential component of Europe's binding targets and China has set itself a target of 30 GW of installations off its coast by 2020. The United States has excellent wind resources offshore, and many projects are under development [4].

## 1.2 Wind turbine overview

Wind turbines transform the kinetic energy in the wind to mechanical energy in a shaft and finally into electrical energy in a generator. The maximum available energy,  $P_{max}$ , is thus obtained if theoretically the wind speed could be reduced to zero:

$$P = \frac{1}{2}\dot{m}V_{\infty}^2 = \frac{1}{2}\rho AV_{\infty}^3 \quad (1.1)$$

where  $\dot{m}$  is the mass flow,  $V_{\infty}$  is the undisturbed wind speed,  $\rho$  the density of the air and  $A$  the area where the wind speed has been reduced. The equation shows that power increases with the cube of the wind speed and only linearly with density and area. The available wind speed at a given site is therefore often first measured over a period of time before a project is initiated. In practice one cannot reduce the wind speed to zero, so a power coefficient  $C_p$  is defined as the ratio between the actual power obtained and the maximum available power as given by the above equation. A theoretical maximum for  $C_p$  exists, denoted by the Betz limit,  $C_{p,max} = 16/27 = 0.593$ . Modern wind turbines operate close to this limit, with  $C_p$  up to 0.5, and are therefore optimized. Sailors discovered very early on that it is more efficient to use the lift force than simple drag as the main source of propulsion. Lift and drag are the components of the force perpendicular and parallel to the direction of the relative wind respectively [1], as it will be better shown in section 3.2.



FIGURE 1.4: A wind turbine complex in southern Wyoming, USA (courtesy Ed Stoddard/Reuters).

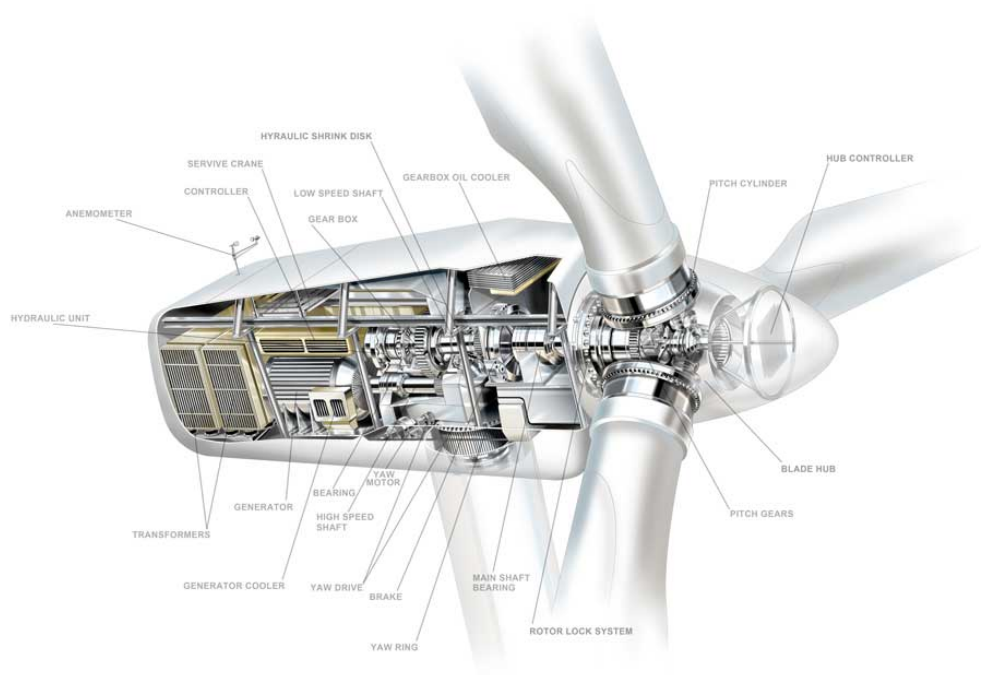


FIGURE 1.5: Wind turbine nacelle layout.

This thesis work focuses on the horizontal axis wind turbine (HAWT), visible in fig. 1.4, where blades are connected to a horizontal rotating shaft. A HAWT is composed by a tower at whose top there is the nacelle, connected to which there are the blades. The importance of the tower height is in the fact that wind speed increases with height above the ground, while the rotor diameter influences the area swept by the blades and so the power production. Internally to nacelle, as visible in fig. 1.5, the mechanical energy of the blades is converted in electricity through the generator and also there are the controllers responsibly of the wind turbine operation.

The anemometer in the rear part of the nacelle gives information to the controller. It can act as a brake on the rotation of the blades, maintaining the turbine in its optimal speed operation range, or can regulate the yaw angle aligning the turbine axes to the direction of the incoming wind. The controller is also responsible of the modification on the pitch angle, that contributes to modify the angle of attack of the blade respect to the incident flow. The gearbox is used to link the low-speed rotor shaft (generally rotating in the range of 20-50 rpm) and the high-speed generator shaft (the rotation regime is reached in the range 1000-3000 rpm). Connected to the rotor shaft there are the blades, usually two or three. Three-bladed turbines are more expensive and heavier than two-bladed ones, but on the other side they present a higher aerodynamic efficiency, they are more powerful, and their movement appears more pleasant to the eyes. Obviously, the blades have a crucial importance on the performances of wind turbines, so they are object of advanced researches. The optimizing processes involve mainly the increase of the aerodynamic efficiency (for example, the first modern wind turbine adopted airplane wings as blades) and the materials quality. In fact blades must be sufficient strong and stiff, have a high fatigue endurance limit and be as cheap and light as possible. Today the most part of turbine blades are built of glass fibre reinforced plastic.

### **1.3 Wind turbine operation**

The power output of a wind turbine varies with wind speed, so as a first general approximation it could be traced a characteristic power performance

curve function of the incoming flow velocity at hub height (an example is reported in fig. 1.6). It is possible to predict the energy production of a wind turbine without considering the technical details of its various components. There are three key points on the velocity scale, covering a particular importance on the turbine operation:

- cut-in speed value: the minimum wind speed at which the machine will deliver useful power, typically [3; 5] m/s;
- nominal wind speed value: the wind speed at which the rated power (generally the maximum power output of the electrical generator) is reached;
- cut-out speed value: the maximum wind speed at which the turbine is allowed to deliver power (usually limited by engineering design and safety constraints), typically 25 m/s [7].

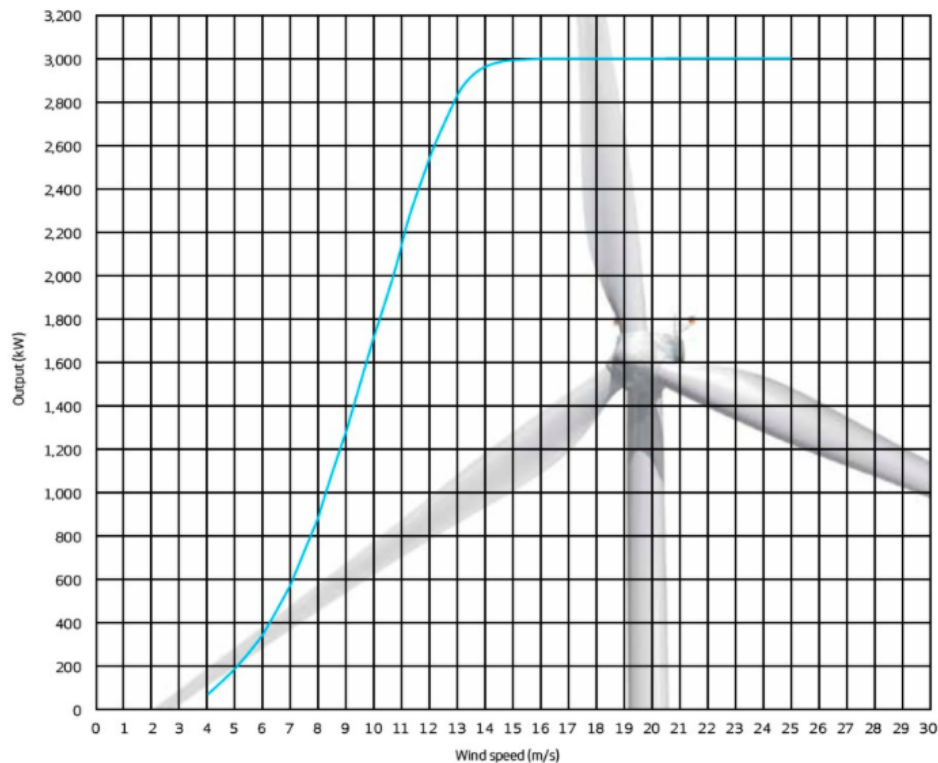


FIGURE 1.6: *Vestas V90 power curve (courtesy Vestas).*

To optimize the power output of the turbine for wind velocities internal to the operational range, the control laws act adjusting the rotor speed and the pitch angle of the blades, modifying the angle of attack and the load in each section of the blades. This consideration justifies a very deep study of the aerodynamic interaction between the fluid and the turbine: the relative velocity of the incident flow seen by the blade section is function of the combination of the undisturbed incoming air speed vector and the rotational speed of the rotor. The relative wind speed vector on each airfoil of the blade can be decomposed in two components: its magnitude and, particularly important, its incidence angle, that depends on the local wind angle and the local rotational velocity. The design of the blade must take into account this characteristic of the machine.



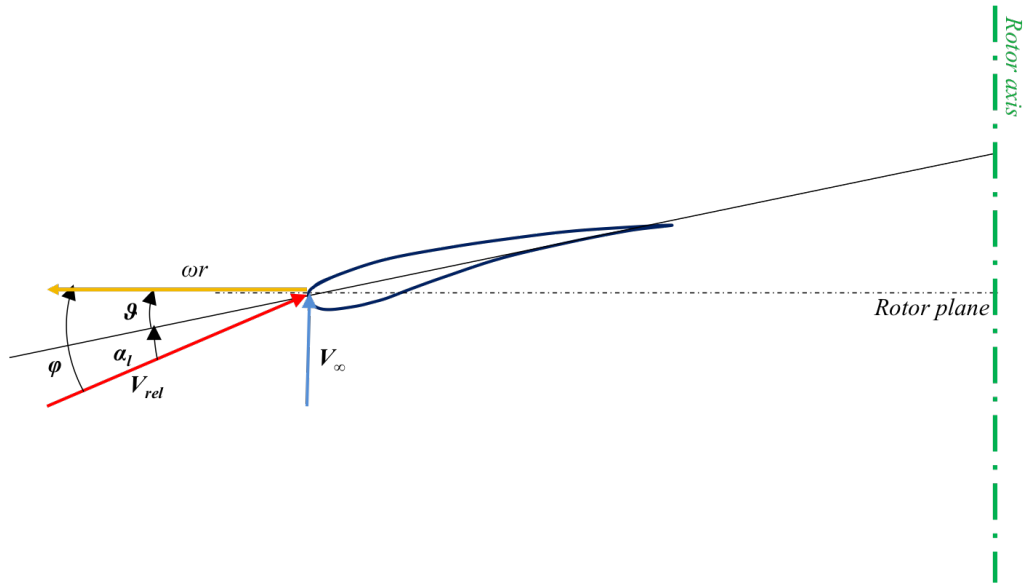


FIGURE 1.7: Definition of the aerodynamic angles on a blade section:  $\phi$  is the incidence angle respect to the rotor plane composed by  $\alpha_l$ , the local angle of attack and  $\vartheta$ , the local pitch angle. Deeper  $\vartheta$  is composed by  $\beta$ , the twist angle of the considered section, and  $\vartheta_p$ , the controlled pitch angle.

Relating to fig. 1.7, the control of a wind turbine acts on the blade pitch angle that changes substantially the angles of attack between the blade local airfoil and the relative wind speed. In this way the wind incidence angle changes of a constant value on the entire blade generating a higher or lower driving force to speed up or slow down the rotor speed. In general the local angle of an airfoil is defined as:

$$\alpha = \phi - \vartheta = \phi - (\beta + \vartheta_p) \quad (1.2)$$

where  $\phi$  is the relative wind incidence angle respect to the rotor plane,  $\vartheta$  is the local pitch angle, sum of  $\beta$  and  $\vartheta_p$ . Clearly the blade pitch  $\vartheta_p$  directly influences the angle of attack and hence the aerodynamic forces on the blade. As said before, the control of the turbine has also the possibility to modify the angle of the incident velocity, acting on the rotational speed of the blades. A marker largely used to have an idea of the kinematics of the system is the non-dimensional parameter TSR (Tip Speed Ratio) defined as:

$$TSR = \frac{\omega R}{V_\infty} \quad (1.3)$$

where  $\omega$  indicates the rotational speed of the rotor,  $R$  the tip radius of the turbine blade, while  $V_\infty$  is the velocity of the undisturbed incoming flow. TSR is useful during the design phase of the blades, when a reference TSR value is an input for the optimization process, customized on the particular installation site. Given this basic information, the control law can be implemented. The easiest control is just a stall regulation: wind turbines are designed to reach the stall condition to maximize the lift generation at a particular value of the angle of attack and, enslaved to this, of TSR. The pitch regulated technique is active control method, adjusting the pitch angle of the blades during the turbine operation. This way lets to optimize the load generation in every situation, both when running in shear or in turbulent flow. The highest control law relates the first two: active law modify the pitch angle in order to make able the blade to work in stall condition only.

# Chapter 2

## Introduction to CFD

The aim of this chapter is to propose a short overview about main aspects of CFD and its governing equations, the open-source software OpenFOAM adopted to perform the simulation tests of this thesis work and some superficial considerations about turbulence modeling.

### 2.1 Computational Fluid Dynamics

Computational fluid dynamics (CFD) is a very useful computer-based tool for the analysis of systems involving fluid flow, heat transfer or other chemical phenomena. CFD applications smear on a wide range including both industrial design of products or processes and the world scientific community of researchers. From the historical point of view, first CFD applications involved aerospace industry in the 1960s and only in a second time other fields began to look at CFD as a suitable way to investigate their problems. CFD has lagged behind for a long period since the tremendous complexity of the fluid behavior. Currently CFD is experiencing a strong period of growth, because its advantages become more evident than the other alternative techniques and computational power increases day by day. Of course, CFD now could be considered equivalent to other computer aided-engineering (CAE) softwares, such as stress analysis codes. Some CFD application areas are:

- aerodynamics of mechanical systems (e.g. aircrafts or vehicles, see fig.

- 2.1): lift and drag evaluation;
- turbomachinery and internal combustion engines;
  - meteorology;
  - chemical process engineering;
  - civil engineering: wind loads evaluation on large structures as bridges or buildings;
  - marine engineering: ship hydrodynamics, loads on offshore structures;

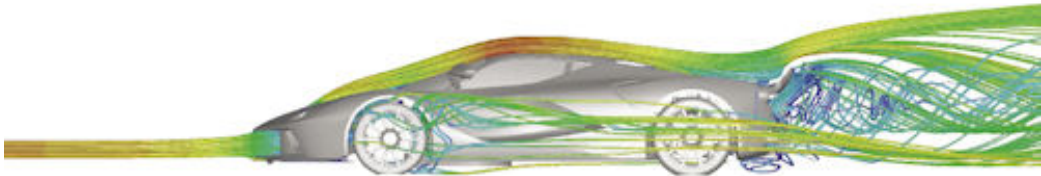


FIGURE 2.1: *An ANSYS simulation of the airflow around the left side of the Ferrari 458 Italia (courtesy ANSYS Corp.).*

Similarly to other CAE softwares, CFD ones let to produce extremely large volumes of results and are particularly suitable for parametric studies, because they do not add extraordinary costs. Also from the point of view of data collection and result analysis, CFD proposes itself as the cheapest

way to gather different data without the necessity of a qualified measurement equipment. Compared to the alternative technologies, such as full-scale measurements or Wind Tunnel tests on scaled model, the most evident advantages token by CFD are:

- substantial reduction of lead times and costs for new design;
- ability to study systems where controlled experiments are difficult or impossible to perform;
- ability to study systems under hazardous conditions at and beyond their normal performance limits (e.g. safety studies and accident scenarios);
- practically unlimited level of detail of results.

### **2.1.1 CFD code operation**

CFD codes are structured around the numerical algorithms that can tackle fluid flow problems. Every CFD test case is composed essentially in three different phases, through which the simulation environment is firstly designed, then the simulation is performed and in the final phase the collected data are elaborated and the final results are extrapolated.

#### **Pre-processing phase**

The first phase concerns with the input of the flow problem definitions to a CFD program and their transformation into a form suitable to be used by the solver. The user is involved in several basilar activities: carefulness and experience are the keys to build a test case able to predict accurate and consistent results. First of all, the computational domain must be defined: this means design the region of interest reproducing the correct geometry of the components of the studied system. To this aim CAD softwares result fundamental in helping the user.

After design, the second operation involves the mesh generation: the computational domain is divided into a number of smaller and non-overlapping sub-domains, called cells. Fluid dynamics equations (hence the solution of velocity, pressure and temperature values) implemented in the second phase act on the nodes inside each cells: it is obvious that the definition in term on numbers and dimension of these control volume is crucial. The accuracy of a CFD solution is governed by the number of a cells in the grid. In general, the larger is the number of cells, the better is the solution accuracy. On the other side, increasing the cell numbers means a higher requirement of computational resources: high-performance computers are necessary to succeed in the simulation results. It must often be found a compromise between the dimension of cells (that should be as smaller as possible), and their number (also them should be small): the solution is a local refinement in different important regions, for example where a strong fluid-structure interaction is expected, close to sharp edges or where could be interesting to have a detailed knowledge about the fluid behavior.

From the fluid point of view, in the first phase the user must specify the fluid properties, such as the viscosity or the turbulence properties, and define the boundary and initial conditions for all the sides and the patches of the computational domain. Also this phase deals with the choice of the mathematical models adopted to integrate the fluid equations or to model the turbulent eddies of the flow.

As it could be seen the pre-processing phase asks for a high-skilled user, with wide spacing-over knowledges: just to have an idea, this phase can cover 50% of the time spent in industry on a CFD problem [8]. Here the user takes into account the identification and the formulation of the flow problem, in terms of the physical and chemical phenomena that will be considered. Introduced approximations and the level of accuracy are determined in this section (e.g. choice of solving the turbulent flow or neglecting the effects of small air bubbles). It is also a good habit to perform a grid dependence study, to make sure that the results are not afflicted by the mesh coarseness.

## Solving phase

The second stage concerns the numerical solution of the fluid dynamic equations: different techniques are possible, but commercial codes usually relies on the finite volume method (FVM), a special finite difference formulation, such as OpenFOAM. The clear relationship between the fundamental physical principles and the numerical algorithm, that makes its concepts much more simple to understand, is one of the reason of the success of FVM. The solution is reached through the following steps:

- integration of the governing equations of fluid over all the control volumes (cells);
- discretization of the resulting integral equations into a system of algebraic equations;
- solution of the algebraic equations by an iterative method.

Commercial softwares propose a wide variety of solvers, involving some approximations (e.g. if the fluid is compressible or not), that are more or less suitable to different test conditions. For example, this thesis work proposes a new solver based on the already-existent PIMPLE solver of OpenFOAM, a large time-step transient solver for incompressible, turbulent flow, while SIMPLE solves only steady-state condition, but with compressible flow.

## Post-processing phase

As in the first phase, also in the latest stage the user must interact with the software. Results often must be not only extrapolated, but also presented in a clear way to people that might not be CFD confident. All CFD packages are now equipped with versatile data visualization tools. After having performed the simulation, these let to show the computational domain and the adopted mesh, vector, surface and contour plots of interesting quantities, such as pressure, velocity or, for example, vorticity. At the end of the simulation the user must make a judgement whether the results are "good enough", so become important the possibility to compare them with previous experience or conclusions worked out with other different methods, such as analytical approaches or experimental tests.

### 2.1.2 OpenFOAM

The logo for OpenFOAM, featuring the word "Open" in a blue serif font, a blue downward-pointing triangle, and the word "FOAM" in a blue sans-serif font.

*The Open Source CFD Toolbox*

FIGURE 2.2: *The OpenFOAM logo (courtesy OpenCFD).*

This thesis work is developed on OpenFOAM (Open Field Operation and Manipulation), a free and open-source CFD toolbox which has a large user base across most areas of engineering and science. OpenFOAM has an extensive range of features to solve anything from complex fluid flows involving chemical reactions, turbulence and heat transfer, to solid dynamics and electromagnetics. By being open, OpenFOAM offers users complete freedom to customize and extend its existing functionality, either by themselves or through support from OpenCFD. It follows a highly modular code design in which collections of functionality (e.g. numerical methods, meshing, physical models, . . .) are each compiled into their own shared library. Executable applications are then created that are simply linked to the library functionality. The core technology of OpenFOAM is a flexible set of efficient *C++* modules. These are used to build a wealth of: solvers, to simulate specific problems in engineering mechanics; utilities, to perform pre- and post-processing tasks ranging from simple data manipulations to visualization and mesh processing; libraries, to create toolboxes that are accessible to the solvers/utilities, such as libraries of physical models [9].

## 2.2 CFD governing equations and OpenFOAM implementation

### 2.2.1 Governing equations

The intention here is to present just a quote of the fundamental governing equations of fluid dynamics; more complete and depth explanations could



be found in several books, such as [8], [10] or [11]. The continuity and the momentum equations are the mathematical statements relying on the fundamental physical principles upon which all of fluid dynamics is based. Considering an appropriate control volume, such as the infinitesimal volume of fluid  $dV$  represented in fig. 2.3 fixed in space and crossed by the flow, equations (2.1) and (2.3) can be written.

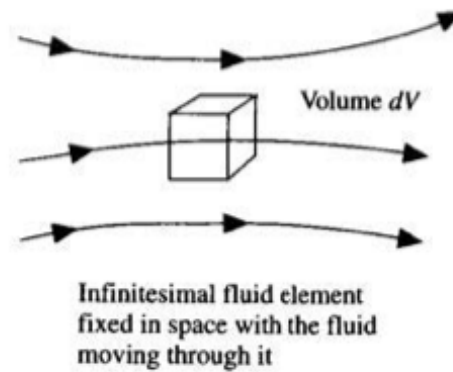


FIGURE 2.3: *The considered control volume.*

### The continuity equation

Referring to the presented control volume, the conservation of mass principle states that the net mass flow out of the element through its surface  $S$  is equal to the time rate of decrease of mass inside the control volume. Thus, the equation written in conservation form is:

$$\frac{\partial \rho}{\partial t} + \nabla \cdot (\rho \mathbf{U}) = 0 \quad (2.1)$$

where  $\rho$  is the fluid density,  $\mathbf{U}$  is the velocity vector, and the operator  $\nabla$  represents the divergence. In the case of incompressible fluid previous equation reduces to:

$$\nabla \cdot \mathbf{U} = 0 \quad (2.2)$$

## Navier-Stokes equations

Navier-Stokes equations are mathematical formulations describing a real fluid motion. They consider each contribution given by all the forces acting on the infinitesimal control volume of fig. 2.3 and its surface. Considering a small volume of fluid, two kinds of force act on it: the first are forces proportional to the considered volume (called body forces), while the second, the surface forces, are due to the interaction between the surface of the element and the surrounding environment. The application of Newton's second law  $\mathbf{F} = m \mathbf{a}$  leads directly to the writing:

$$\frac{\partial \rho \mathbf{U}}{\partial t} + \nabla \cdot (\rho \mathbf{U} \mathbf{U}) - \nabla \cdot \mu \nabla \mathbf{U} = -\nabla(p) \quad (2.3)$$

Eqn. (2.3) is the vectorial form of Navier-Stokes equations and it is yet presented in a way to be written in *C++* language, adopted by OpenFOAM.

### 2.2.2 OpenFOAM implementation of Navier-Stokes equations

As said before in section 2.1.2, the code is written in *C++*, an object oriented programming (OOP) language. This is an advantage, since it lets the top-level code to be intuitive to the user. The implementation of Navier-Stokes equations (2.3) in OpenFOAM is obtained as in the following, where it is easy to recognize the corresponding forms:

```
solve
(
    fvm::ddt(rho, U)
  + fvm::div(phi, U)
  - fvm::laplacian(mu, U)
  ==
  - fvc::grad(p)
);
```

## 2.3 Turbulence modeling

Turbulence is one of the key aspect in Wind Engineering applications. A good knowledge of turbulent phenomena and their modeling is still an open challenge. A good definition of turbulence, that gives the idea of its complexity, was provided by G.I. Taylor and T. von Karman [12]: *"Turbulence is an irregular motion which in general makes its appearance in fluids, gaseous or liquid, when they flow past solid surfaces or even when neighboring streams of the same fluid flow past or over one another"*.

Perhaps the main characteristics of a turbulent flow are:

- **Randomness:** since turbulent flows are strongly influenced by the boundary and the initial conditions. Small differences lead to a fully-different evolution of the fluid in the time history, making a turbulent flow distinguish due to its instability. In addition, in turbulent flow occur some particular phenomena called coherent structures or eddies, which are well defined sequences of events associated with organized motion, whose occurrence location and time is random.
- **Vorticity:** it is defined as the curl of the velocity vector: all turbulent flows are rotational distinguished by a high level of vorticity, typically associated to the coherent structures.
- **Mixing:** the third characteristic refers to the high attitude to of turbulent to heighten the transport of mass, momentum and energy due to the macroscopic scale of the randomness in turbulent flow. In fig. 2.4, this property is briefly reproduced, comparing the laminar and turbulent flow. In the first case, mixing happens only at a molecular scale, while in the second mixing occurs at a higher scale and it is more effective.

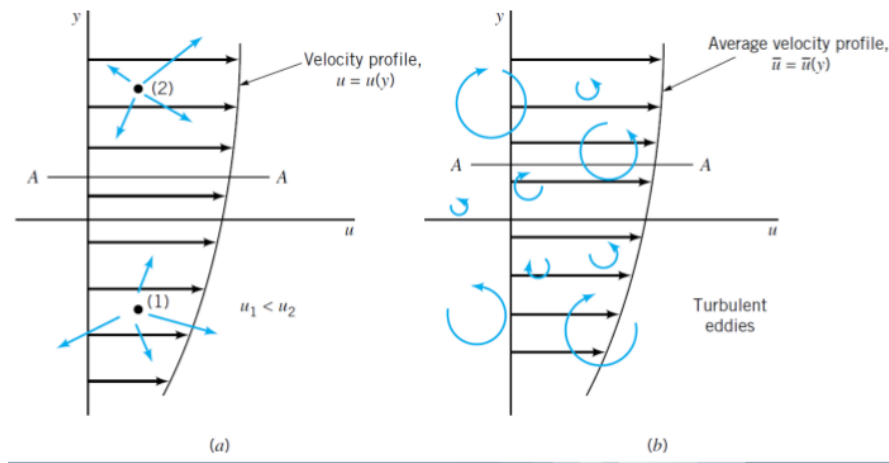


FIGURE 2.4: *Mixing effectiveness in the laminar flow (a) and in the turbulent one (b).*

Turbulence modeling in CFD codes follows some numerical approaches that do not require to solve directly the Navier-Stokes equations: they limit to solve only a part of them (arbitrarily chosen), while, for the other different models are applied. As stated in [13], flows that must be analyzed usually are turbulent, time and space dependent. In contrast to Direct Numerical Simulations (DNS), generally the small scale turbulent component is treated separately and appropriately modeled. On the other side large scales phenomena, depending by the considered geometry, are fully simulated. The two main techniques alternative to DNS are:

- Reynolds Averaged Navier-Stokes (RANS): the aim is to solve the mean field of a generic quantity and to model the Reynold stresses deriving from the average operator on the Navier-Stokes equations;
- Large-eddy Simulation (LES): it is an intermediate approach between DNS and RANS, based on the assumption that small-scale turbulent eddies are responsible mostly for energy dissipation in the mean than the large-scale ones, while the main contributions in momentum and energy equations belong to large turbulent scales [14]. A filtering operation is required to determine the minimum resolved scale and then a model is adopted to take into account the inferior scale impact.

The presented approaches let the users to investigate more complicated problem, even if it is mandatory to be careful in the model choice. Various levels of approximation, yielding more or less detailed descriptions of the state of the flow can be reached function of the adopted model, the working fluid, the boundary and the initial conditions.

### 2.3.1 Turbulence implementation in OpenFOAM

As done in section 2.2.2 the implementation in OpenFOAM of the different turbulence models is quite simple due to the flexibility of the code. For the applications of this work, the working fluid could be considered as incompressible. So, eqn. 2.3 reduces to:

$$\frac{\partial \overline{\mathbf{U}}}{\partial t} + \nabla \cdot \overline{\mathbf{U} \mathbf{U}} - \nu \nabla^2 \overline{\mathbf{U}} = -\nabla(\overline{p}) \quad (2.4)$$

The filtered convection term  $\nabla \cdot \overline{\mathbf{U} \mathbf{U}}$  requires the knowledge of the exact solution since it is nonlinear. It is not possible to know the exact solution, so it must be modeled. The fluctuating part of velocity generates the Reynolds stresses term, treated together with the diffusive term:

$$\frac{\partial \overline{\mathbf{U}}}{\partial t} + \nabla \cdot \overline{\mathbf{U} \mathbf{U}} + 2\nu_{eff} \nabla(\nabla \overline{\mathbf{U}} + (\nabla \overline{\mathbf{U}})^T) = -\nabla(\overline{p}) \quad (2.5)$$

The solver equation changes into:

```
solve
(
  fvm::ddt(U)
  + fvm::div(phi, U)
  + turbulence->divDevReff(U)
  ==
  - fvc::grad(p)
);
```

The Boussinesq assumption states that the Reynolds stress tensor is pro-

portional to the trace-less mean strain rate tensor, that means:

$$\tau_{ij} \propto -\overline{u'_i u'_j} = \nu_T \left( \frac{\partial \overline{U}_i}{\partial x_j} + \frac{\partial \overline{U}_j}{\partial x_i} \right) - \frac{2}{3} \kappa \delta_{ij} \quad (2.6)$$

where  $\nu_T$  represent the eddy cinematic viscosity and contributes to  $\nu_{eff}$  of eqn. (2.5). The RANS approach prescribes different ways to estimate this quantity, from very simple models like Spalart-Allmaras to a more complicated ones like  $\kappa - \epsilon$  [15], or the  $\kappa - \omega$  *SST*. The last one is adopted for RANS simulations performed during the course of the work.

Using a LES approach, the nonlinear part is modeled through a Smagorinsky model: the term of the code `turbulence->divDevReff(U)` contains the Sub-Grid Scale (SGS) model:

$$2\nu_{eff} \nabla(\nabla \overline{\mathbf{U}} + (\nabla \overline{\mathbf{U}})^T) \quad (2.7)$$

where the effective viscosity  $\nu_{eff}$  is given by the sum of the eddy viscosity  $\nu_{SGS}$  and the kinematic viscosity of the fluid  $\nu$ :

$$\nu_{eff} = \nu + \nu_{SGS} \quad (2.8)$$

The eddy viscosity  $\nu_{SGS}$  directly comes from the applied Smagorinsky model and it is given by:

$$\nu_{SGS} = (C_s \Delta)^2 (\nabla \overline{\mathbf{U}} + (\nabla \overline{\mathbf{U}})^T) \quad (2.9)$$

where  $\Delta$  is the grid size and  $C_s$  the Smagorinsky constant for isotropic turbulence.

# Chapter 3

## Wind turbine numerical simulation

This chapter propose an overview of HAWT simulation models, from classical BEM method to advanced CFD simulations, pointing the focus on body force methods like the Actuator Line one that is the model used in this thesis work. A quick overview of accuracy level of existent implemented aerodynamics codes is also inserted as motivation of current research effort is this field of study.

### 3.1 Turbine numerical simulation overview

The first and classical analytical methods of HAWT operation analysis is the Blade Element Momentum method (BEM) which is a very quick tool useful to calculate loads, thrust and power for different settings of wind speed, rotational speed and pitch angle [1]. BEM was developed by Glauert in 1935 and it is essentially very similar to the normal tools of analysis used in the study of traditional fluid machines: momentum conservation in integral form is applied to the control volume containing the turbine, starting far upstream the rotor and ending in the far wake zone. The changes in velocity of the fluid investing the turbine are calculated function of generated thrust and torque. Being a method based on integral momentum conservation, it

makes the BEM a very fast but also quite simplified analysis instrument, in particular BEM is not able to reproduce in detail the interaction between the various incoming flow condition and the wind turbine generator [16].

In the last few years a lot of effort was spent in the development of new much more refined turbine models able to correctly reproduce the exact physics of the flow interaction with turbine rotor. The motivation of such effort is the need to develop tools to predict with accuracy the behavior of HAWTs operating in special conditions not studied using the BEM; conditions such as those encountered by turbines clustered in wind farms that are subject to not uniform flow for the presence of the upstream turbines [17] or the interaction between ABL shear and unsteady flow with new generation multi-MW wind turbine prototype.

Essentially three different approaches have been developed for advanced analysis based on CFD [18]:

- *Actuator Disk (AD)*: wind turbine is modeled as a disk force added as source term in CFD discretized Navier-Stokes momentum equation.
- *Actuator Line (AL)*: very similar to AD but instead of a disk turbine rotor blade are singly modeled as force lines.
- *Fully Resolved Wind turbine rotor (FRW)*: wind turbine rotor shape is entirely modelled in CFD computational mesh.

Different studies have been done to test the actual capacity of each one of these methods, from blind-tests [19], [20] and wind tunnel modeling experience FRW appears to be the CFD analysis method that can predict with best accuracy both loads and wake dynamics of wind turbine [20]. The serious FRW problem is the high computational cost that limits the possibility to use this method as common analysis tool of various operational condition or where there is the need of simulating big domain and multiple turbine like in wind farm power prediction and design [18]. For this reason AD and AL methods are today studied by numerous research centers (such as NREL and DTU) being less numerical expensive but potentially very accurate simulation methods. The following sections will present these two methods after an introduction to the fundamentals of the BEM.



AL, AD and BEM are in fact closely related and similar to each other, for all three methods the turbine is not a machine with a particular design and shape but a series of tabulated data about rotor diameter, speed of revolution, blade twist, chord and airfoil type. All three methods with different tools, integral momentum equation (BEM) or CFD (AD - AL), predict the flow established around operative turbine by the application of equivalence force to the elaborated wind flux.

## 3.2 BEM foundation

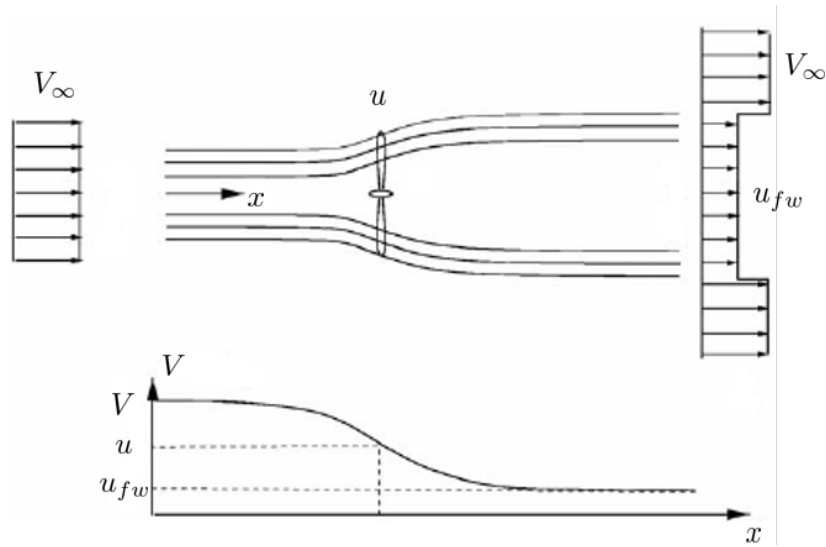
This BEM foundation is mainly inspired by M. Hansen in [1].

As said BEM is based on momentum conservation law, the turbine rotor is substantially modeled as a permeable disk where blade forces are distributed, the flow physically interacts with these distributed forces exchanging momentum with turbine loads. BEM theory originates from two different theories, the blade-element and the one-dimensional momentum theory [21]. The momentum theory parametrizes the thrust and torque applying the conservation of linear and angular momentum equation to the control volume of annular stream tube through the wind turbine. The simplest case of one-dimensional momentum theory application is a perfect homogeneous rotor loaded only axially, reported in fig. 3.1, the rotor thrust is equally distributed on the entire turbine swept area, in this case the rotor equally slows down the fluid: assuming perfect efficiency all the lost kinetic energy by wind flow is transformed in power output. The thrust  $T$  and power output  $P$  are simply equal to:

$$T = \dot{m}(V_\infty - u_{fw}) \quad (3.1)$$

$$P = \frac{1}{2}\dot{m}(V_\infty^2 - u_{fw}^2) \quad (3.2)$$

In eqn. (3.1)  $T$  is equal to the momentum deficit of turbine mass flow,  $\dot{m}$ , from velocity far upstream  $V_\infty$  and velocity in the far wake zone  $u_{fw}$ . Velocity on rotor plane,  $u$ , is different from  $V_\infty$  for rotor loads acting on wind flow, the axial induction factor,  $a$ , in (3.3) is defined as the fraction of lost

FIGURE 3.1: *Velocity over homogeneous rotor.*

speed. In (3.4)  $a$  is linked to the turbine thrust or equally to coefficient of thrust,  $C_T$ , in (3.5).

$$u = (1 - a)V_\infty \quad (3.3)$$

$$a = \frac{T}{2\dot{m}V_\infty} \quad (3.4)$$

$$4a(1 - a) = C_T \quad (3.5)$$

For a homogeneous rotor the coefficient  $C_T$  is sufficient for describing turbine wind interaction. The knowledge of  $C_T$  allows to estimate velocity on rotor and in far wake zone and consequently generated thrust and power are calculated.

However in general turbine loads are not homogeneously distributed due to change in blade characteristics along radial span and tip and root aerodynamics effect, see fig. 3.2. In this case the blade-element theory asserts that the force of each blade section can be evaluated separately as it is done for 2-dimensional airfoil. The flow passing through the turbine rotor is consequently divided in  $N$  annular elements each of them supposed to be totally independent from the other; then for each annular element the momentum conservation theory is applied, like in homogeneous rotor case, allowing to

find the flow velocity over rotor plane.

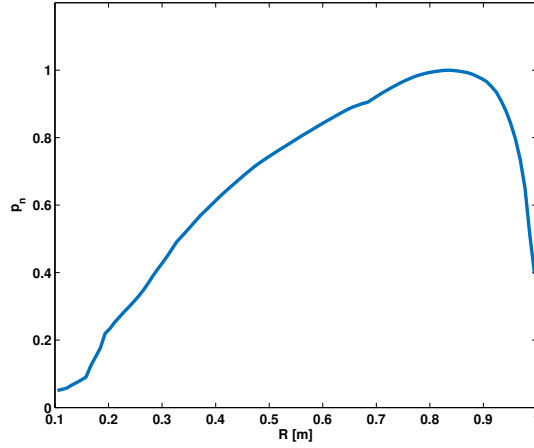


FIGURE 3.2: *Typical blade axial load distribution.*

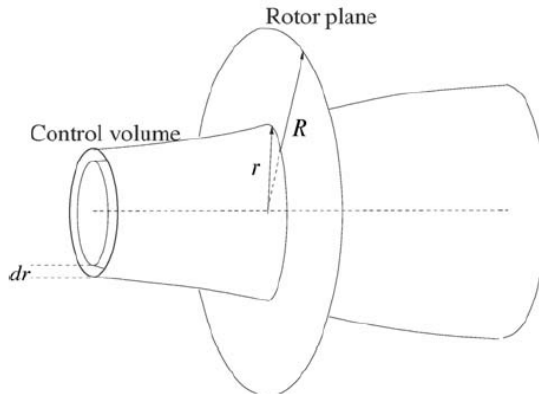


FIGURE 3.3: *BEM annular analysis.*

For the  $i$ -th annular element the portion of generated thrust ( $dT$ ) and torque ( $dM$ ) are expressed in (3.6) and (3.7).

$$dT = d\dot{m}(V_\infty - u_{fw}) \quad (3.6)$$

$$dM = r d\dot{m} \Theta_{fw} \quad (3.7)$$

$$d\dot{m} = u(2\pi r dr) \quad (3.8)$$

In BEM the rotation induced in wake from torque extraction is taken in consideration, in (3.7)  $\Theta_{fw}$  is wind rotational speed in the far wake (rotational speed is assumed to be zero upstream the rotor), so the tangential induction factor,  $a'$  is defined as:

$$\Theta_{fw} = 2a'\omega r \quad (3.9)$$

having defined both axial and tangential induction factor the velocity on rotor plane,  $\mathbf{u}$ , and correspondent relative velocity,  $\mathbf{V}_{rel}$ , are equal to:

$$\mathbf{u} = (1 - a)V_\infty \mathbf{n} - a'\omega r \mathbf{t} \quad (3.10)$$

$$\mathbf{V}_{rel} = \mathbf{u} - \omega r \mathbf{t} = (1 - a)V_\infty \mathbf{n} - (1 + a')\omega r \mathbf{t} \quad (3.11)$$

where  $\mathbf{t}$  and  $\mathbf{n}$  are direction tangential and normal to rotor plane, see fig. 3.6, the annular mass flow,  $dm$ , in (3.8) is the wind speed at rotor times the annular area. The axial and tangential induction factors are functions of coefficients of axial,  $C_n$ , and tangential,  $C_t$ , forces as defined in:

$$a = \frac{1}{\frac{4 \sin^2 \phi}{\sigma(r)C_n} + 1} \quad (3.12)$$

$$a' = \frac{1}{\frac{4 \sin \phi \cos \phi}{\sigma(r)C_t} - 1} \quad (3.13)$$

where  $\phi$  is the wind angle on rotor plane as reported in fig. 3.6,  $C_n$  and  $C_t$  are calculated for every annular section as:

$$C_n = \frac{F_n}{\frac{1}{2}\rho V_{rel}^2 c} \quad (3.14)$$

$$C_t = \frac{F_t}{\frac{1}{2}\rho V_{rel}^2 c} \quad (3.15)$$

where  $F_n$  and  $F_t$  are force projections on  $\mathbf{n}$  and  $\mathbf{t}$  of blade lift and drag as:

$$F_n = L \cos \phi + D \sin \phi \quad (3.16)$$

$$F_t = L \sin \phi - D \cos \phi \quad (3.17)$$

finally lift and drag are defined like normal force generated by 2-dimensional airfoil as:

$$\mathbf{L} = \frac{1}{2}\rho V_{rel}^2 BC_L(\alpha)c\mathbf{l} \quad (3.18)$$

$$\mathbf{D} = \frac{1}{2}\rho V_{rel}^2 BC_D(\alpha)c\mathbf{d} \quad (3.19)$$

$$\phi = \angle \mathbf{V}_{rel} \quad (3.20)$$

$$\tan \phi = \frac{(1-a)V_\infty}{(1+a')\omega r} \quad (3.21)$$

$$\alpha = \phi - \beta \quad (3.22)$$

angles  $\phi$ ,  $\beta$  and  $\alpha$  are angles of relative velocity, twist plus pitch and attack as defined in fig. 3.6,  $c$  is the local value of blade chord and  $B$  is the number of blade, lift and drag are forces per blade unit length, total generated force can be integrated along blade radial extension. Equations from (3.14) to (3.22) allow to find rotor loads from velocity  $\mathbf{u}$ , which can be calculated from  $V_\infty$  known induction factors using (3.12) and (3.13), that are derived from integral momentum conservation equation.

### 3.3 Actuator Disk Model

As described in previous section BEM can find the relationship between  $V_\infty$  and velocity-loads on rotor, the main limitation is that upstream flow is described with  $V_\infty$  only, so it is supposed to be a uniform not turbulent inflow condition, nor ABL nor possibility of previous turbines wake are taken in consideration. The BEM limitations have been treated with the development of the Actuator Disk methods first presented by Soresen [22], this methods apply thrust and torque as body force directly in Navier-Stokes set of equations solvable with a CFD approach thus permitting a greater flexibility of application.

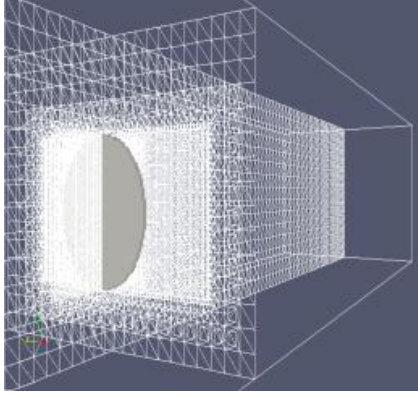


FIGURE 3.4: *The rotor force is inserted in CFD cells belonging to grey area.*

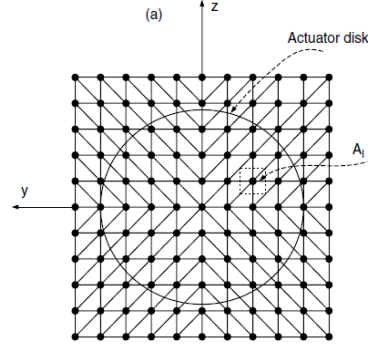


FIGURE 3.5: *The rotor force is inserted in cells inside AD circular area.*

The Navier-Stokes incompressible equations with body force insertion are in the form:

$$\frac{\partial \mathbf{u}}{\partial t} + (\mathbf{u} \cdot \nabla) \mathbf{u} + \frac{1}{\rho} \mathbf{f} = -\frac{1}{\rho} \nabla p + \mu \nabla^2 \mathbf{u} \quad (3.23)$$

$$\nabla \cdot \mathbf{u} = 0 \quad (3.24)$$

In (3.23) the inserted source force  $\mathbf{f}$  is put at first member and represents the aerodynamic force applied by fluid on the rotor or rather the generated lift and drag on rotor blade.

Force  $\mathbf{f}$  to be inserted can be chosen with different level of desired accuracy, it is possible to model the turbine as an homogeneous rotor, like described above, so thrust is calculated from  $C_T$  as:

$$T = \frac{\rho V_\infty^2}{2} A_{cell} C_T \quad (3.25)$$

where  $A_{cell}$  is the frontal area of the computational cell where the disk force is inserted [21], in this case the wake does not rotate and flow passing through turbine is evaluated only on average value.

A more detailed method is the blade loads calculation like in BEM, using blade-element theory. Loads are calculated independently for every blade section, the blade relative velocity is estimated along the entire blade span

and the force is found using local tabulated blade data.

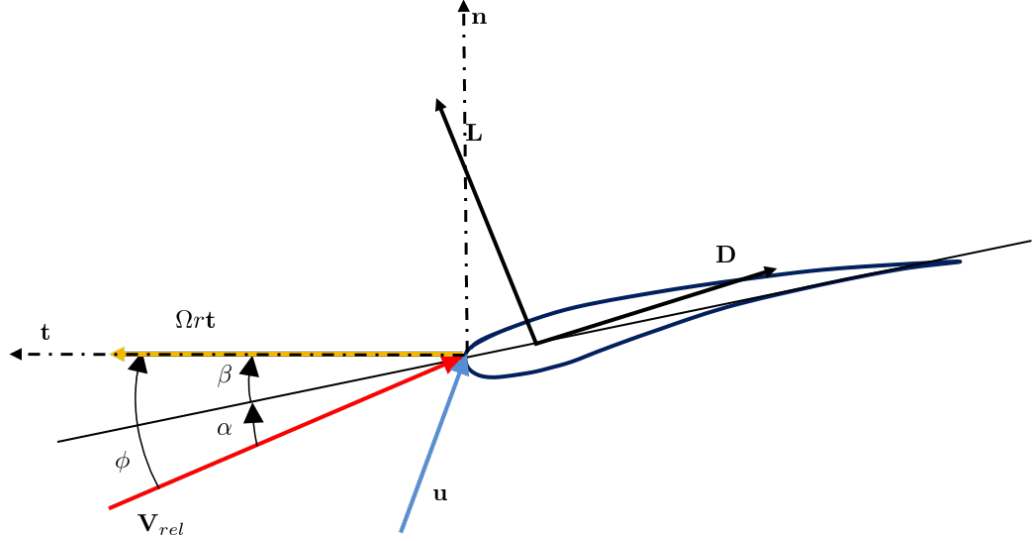


FIGURE 3.6: *Relative velocity on blade section.*

From  $\mathbf{u}$ , relative velocity of every disk cell is calculated:

$$\mathbf{V}_{rel} = \mathbf{u} - \omega r \mathbf{t} = (u_t - \omega r) \mathbf{t} + u_n \mathbf{n} + u_r \mathbf{r} \quad (3.26)$$

where  $\mathbf{t}$  and  $\mathbf{n}$  have already been defined and reported in fig. 3.6 while  $\mathbf{r}$  is direction tangential to blade span. Blade forces are therefore calculated as 2-dimensional loads:

$$\mathbf{V}_{rel}^{2D} = \mathbf{u}^{2D} - \omega r \mathbf{t} = (u_t - \omega r) \mathbf{t} + u_n \mathbf{n} \quad (3.27)$$

$$\mathbf{L} = \frac{1}{2} \rho (V_{rel}^{2D})^2 BC_L(\alpha) c \mathbf{l} \quad (3.28)$$

$$\mathbf{D} = \frac{1}{2} \rho (V_{rel}^{2D})^2 BC_D(\alpha) c \mathbf{d} \quad (3.29)$$

$$\phi = \angle \mathbf{V}_{rel}^{2D} \quad (3.30)$$

$$\alpha = \phi - \beta \quad (3.31)$$

the applied force on disk is thus:

$$\mathbf{F}_{2D} = \mathbf{L} + \mathbf{D} \quad (3.32)$$

Where  $\mathbf{F}_{2D}$  is the cross-sectional element force per spanwise unit length. In eqn. (3.23)  $\mathbf{f}$  like the other terms have the dimension of force per unit volume [ $N/m^3$ ], the force per unit volume is made explicit in (3.33), where  $dx$  is rotor disk thickness in axial direction.

$$\mathbf{f} = \frac{\mathbf{F}}{dV} = \frac{\mathbf{L} + \mathbf{D}}{2\pi r dx} \quad (3.33)$$

In every computational cell inside the rotor area, see fig.3.4 - 3.5,  $\mathbf{f}$  is then inserted and update at every time-step.

The insertion of force directly in NS equation allows a much better and detailed wake reproduction. This AD ability can be useful for simulating misaligned-yawed working condition [23], wind farm behavior [24] or in [25] where AD has been used in unsteady ABL flow condition.

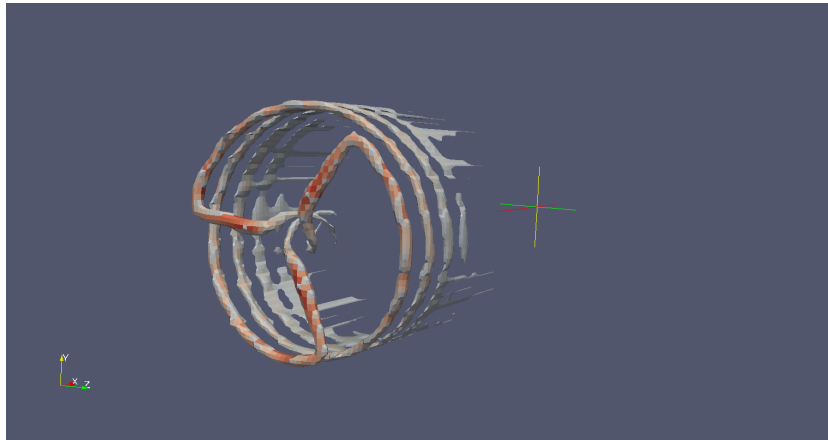
### 3.4 Actuator Line Model

Citing directly Troldborg's PhD thesis [17]:

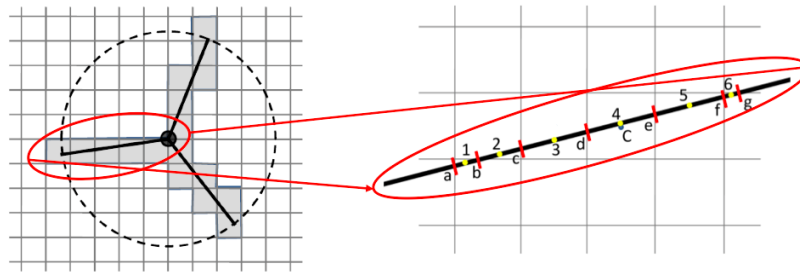
*The main limitation of the actuator disk method is that, strictly speaking, it is only valid for rotationally symmetric flow conditions since the forces at each spanwise section are distributed evenly in the azimuthal direction. This also imply that the presence of the blades is taken as an integrated part in the circumferential direction and hence the method cannot capture the influence of the tip vortices*

To overcome these AD limitations Sorensen presented the AL method [16].





(A) *AL vorticity plot*



(B) *blade force is inserted in cells intersecting blade line*

The AL method distributes the force along blade and not on the entire rotor area, and though it is a complication, line force distribution allows to reproduce tip and root generated vortices and consequently a better wind turbine wake [26]. In fig. 3.7b only for cells intersecting the blade line the force is calculated, the flow is deflected around a line force similarly to real blade flow, in fig. 3.7a is clearly visible the vorticity created around blade line forces, with AD those vortex structures are not visible since the flow is deviated by a "wall" of force. For every cell in the blade line the wind velocity,  $\mathbf{u}$  is evaluated to calculate the relative velocity, the blade line is therefore divided in multiple segment according to mesh intersections, every segment is studied as a 2-dimensional airfoil according to blade-element theory, lift

and drag for each blade segment is calculated as:

$$\mathbf{V}_{rel}^{2D} = \mathbf{u} - \omega r \mathbf{t} = u_t - \omega r \mathbf{t} + u_n \mathbf{n} \quad (3.34)$$

$$\mathbf{L} = \frac{1}{2} \rho (V_{rel}^{2D})^2 C_L(\alpha) c t \mathbf{l} \quad (3.35)$$

$$\mathbf{D} = \frac{1}{2} \rho (V_{rel}^{2D})^2 C_D(\alpha) c t \mathbf{d} \quad (3.36)$$

$$\phi = \angle \mathbf{V}_{rel}^{2D} \quad (3.37)$$

$$\alpha = \phi - \beta \quad (3.38)$$

where  $c$  is the local value of chord and  $t$  is the length of line segment belonging to cell, force is then inserted in correspondent cell as force per unit volume:

$$\mathbf{f} = \frac{\mathbf{L} + \mathbf{D}}{V_{cell}} \quad (3.39)$$

At every time-step the position of the blade have to be updated, the cells intersecting the line are recalculated and so the volume forces are inserted. For this continuous blade position update AL implementation is more developing and numerical challenging than AD, but for the much better wake reproduction ability AL appears to be the best compromise between computational cost and simulation performance, in fact AL does not need the complex grid of FRW model but nonetheless it potentially can reach a similar level of simulation accuracy. So, these are among the other reasons for which the code of this thesis is based on AL.

Current most important implementations of the AL method are those studied by Technical University of Denmark (DTU) based mainly on work of J.N. Sorensen and R. Mikkelsen and by National Renewable Energy Laboratory (NREL), University of Colorado based on the work of M. Churchfield using the OpenFOAM framework.

### 3.5 Turbine model performance analysis

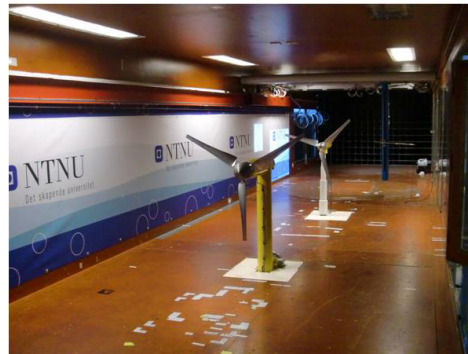
Various studies have been performed to evaluate the actual capacity of the different turbine simulation methods. Two very recent comparison of simulated predictions to measurements turbine data are:

- **MexNext project:** joint project of 20 participants from 11 countries, from different university research centers. The focus of the project was to understand the level of accuracy of current state of art of turbine aerodynamic model, a first comparison result available in June 2011 [27].
- **Nowitech and Norcowe Blind Test 1-2:** Norwegian research programs Nowitech and Norcowe organized a workshop on wind turbine wake modeling, various participants from academic and industrial worlds tested their turbine models against the measurement performed on the NTNU (Norwegian University of Science and Technology) wind turbine model, Blind test 2 workshop results held in October 2012 [29].

These two studies are very similar, the goal of both was to test effective reproduction capacity of nowadays available HAWT aerodynamic model using as benchmark the wind tunnel experimental measurements.



(A) *MexNext* wind tunnel model, test performed at LLF.



(B) *Nowitech and Norcowe blind test* wind tunnel model, two rotors have been studied in NTNU wind tunnel facility.

The IEA (International Energy Agency) Wind task 29, or MexNext, purpose was a deep investigation of the Mexico project experimental data and a comparison with participants' aerodynamic codes. European Union project

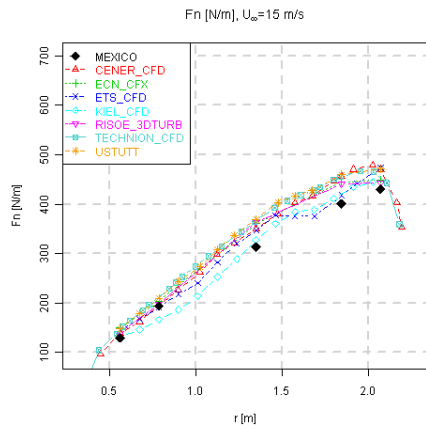
Mexico (Model Rotor Experiments In Controlled Conditions) was a wind tunnel measurement experimental test performed in 2006 in the open section of the Large Low-speed Facility (LLF) of DNW in the Netherlands, tunnel section measured 9.5x9.5 m while model turbine rotor diameter was 4.5 m [27], visible in fig. 3.8a. The Mexico project can be considered as the successor of the NREL Phase VI (NASA - Ames) experiment [28], since both Mexico and NREL experience aims were to provide detailed data from very big wind turbine model tunnel tests, with particular attention to blade loads, estimated with pressure taps applied at different radial positions, and wake structure, for which sampling Mexico project also includes a direct flow field measurement with PIV technique. The available data from Mexico experience MexNext project are both about blade loads and wake, to the turbine aerodynamic code of participants was asked for a prediction of both. MexNext participants were divided in two groups: lifting line codes, the ones that need input of the aerodynamic coefficients like AD and AL, and CFD codes for which the actual geometry of the blade surface is taken into account.

Nowitech and Norcowe Blind Test 1-2 were organized by the two Norwegian offshore turbine research centers at NTNU 2.7x1.8 m wind tunnel with 0.9 m rotor turbine model [29] Although it is a much simpler and small project then MexNext, since nor blade pressure nor wake PIV measurement was performed, Nowitech and Norcowe Blind Tests were interesting for heterogeneity of participants that came not only from academic centers but also from industrial world and and for the fact that in the 2nd blind test a turbine tandem set-up was studied [20]. Participants'codes were based on various models: BEM, AD, AL and FRW.

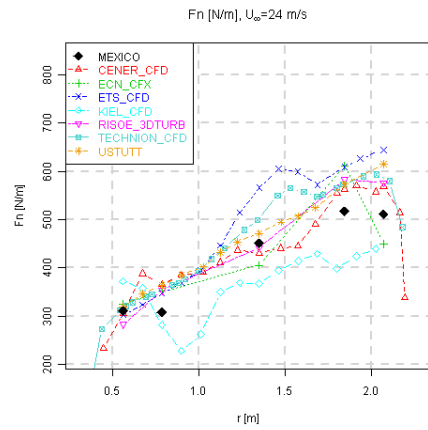
The results of this two comparison project are interesting for the understanding of nowadays ability to predict wind turbine loads and wind turbine generated wake. Results discussion can be found in [27] and [30] for MexNext and in [19] and [20] for Nowitech and Norcowe Blind Test 1 and 2. It does, however, note that the analysis for the Blind Test 2 is still in progress, conclusive scientific articles are still in publication process. MexNext loads and wake comparison data are reported in fig. 3.9, 3.10 and 3.11. Nowitech and Norcowe Blind Test 1 comparison data are reported in fig. 3.13.

In MexNext the comparison results as a poor agreement between calculated and measured loads was found, the lifting line codes in general over predict the normal force at the design operation condition,  $TSR = 10$ , while a under prediction was found for stalled-condition,  $TSR = 6.5$ . An overall better reproduction quality was found in CFD codes, also in wake reproduction the error between measurements and code predictions was high with no correspondence between codes that can better predict blade loads and codes that can better predict turbine wake [30], [27]. Poor agreement in predictions and measurements was found also in Nowitech and Norcowe Blind Test 1-2: in the first a turbine in steady state inflow condition was tested and a large spread was observed, both in blade loads and turbine wake. There was not found an 'optimal' simulation code and in the 2nd blind test with turbine tandem set-up was even more difficult to find agreement in prediction and measurement [19], [20].

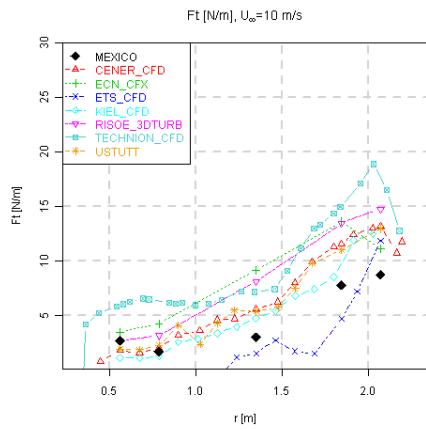
The most advanced AL code presents in both comparison projects was the DTU one, named *DTU\_MEK\_AL\_OAD* in MexNext data and *Sorensen & Mikkelsen Les* in Nowitech and Norcowe Blind Test data. In both comparisons the DTU AL code reproduces well both the wake and the velocity deficit, as visible in fig. 3.11, 3.13c - 3.13d and in wake turbulent kinetic energy estimation [29], [19]. However in fig. 3.10, 3.13a - 3.13b the load results are similar or worse then other less refined method like BEM.



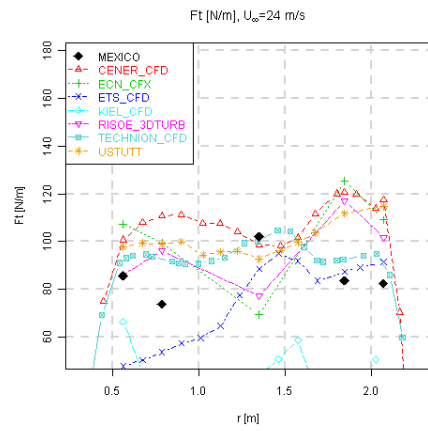
(A)  $F_n$  at  $TSR=10$



(B)  $F_n$  at  $TSR=6.67$

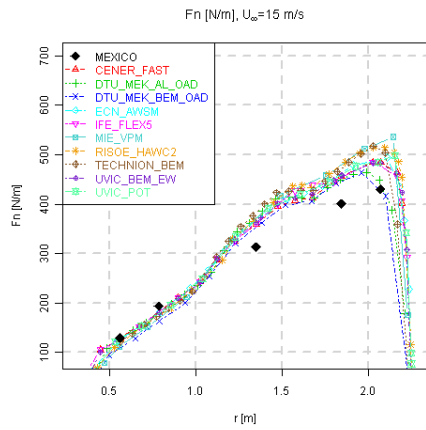


(C)  $F_t$  at  $TSR=10$

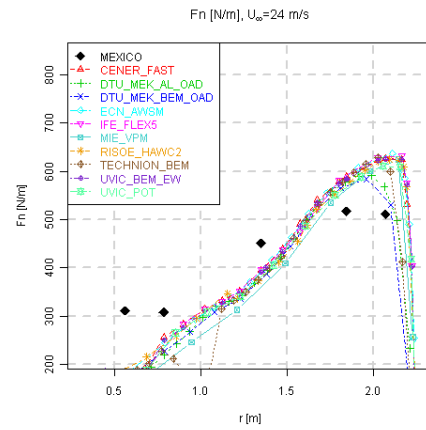


(D)  $F_t$  at  $TSR=6.67$

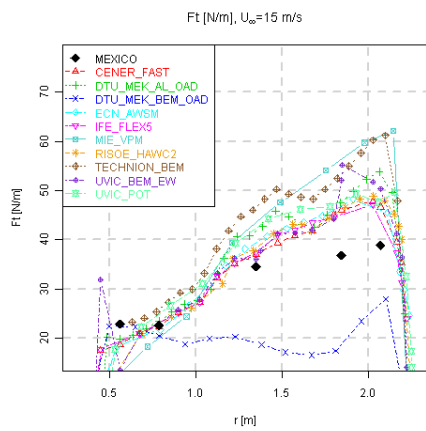
FIGURE 3.9: Normal and tangential force comparison from MexNext result analysis: CFD codes.



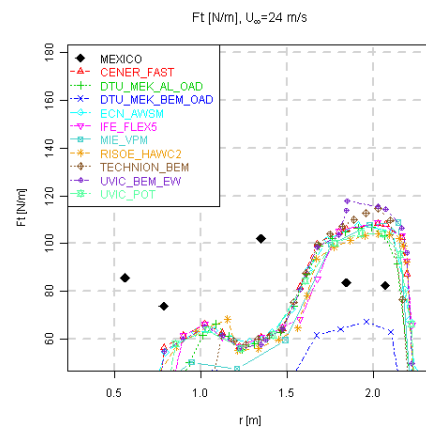
(A)  $F_n$  at  $TSR=10$



(B)  $F_n$  at  $TSR=6.67$



(C)  $F_t$  at  $TSR=10$



(D)  $F_t$  at  $TSR=6.67$

FIGURE 3.10: Normal and tangential force comparison from MexNext result analysis: lifting line codes.

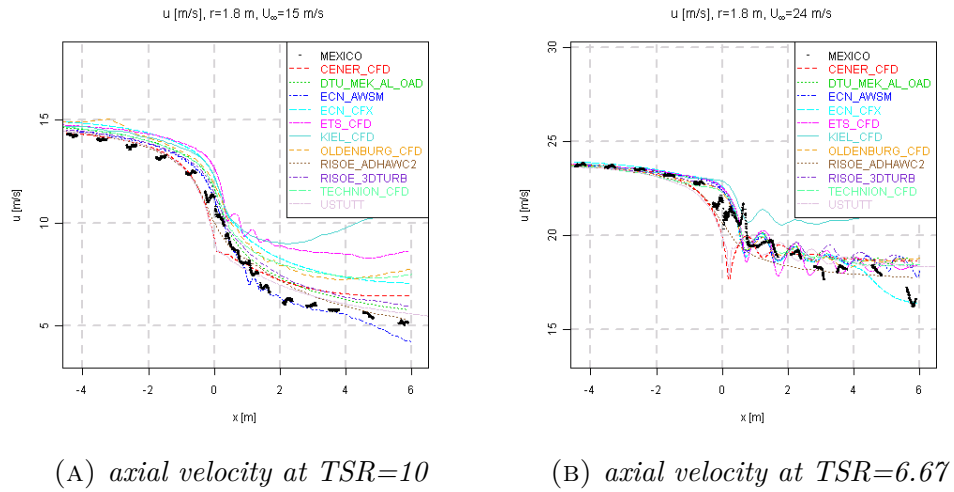


FIGURE 3.11: Axial velocity sampled on a line perpendicular to rotorplane at 80% blade span, CFD and lifting line codes are compared.

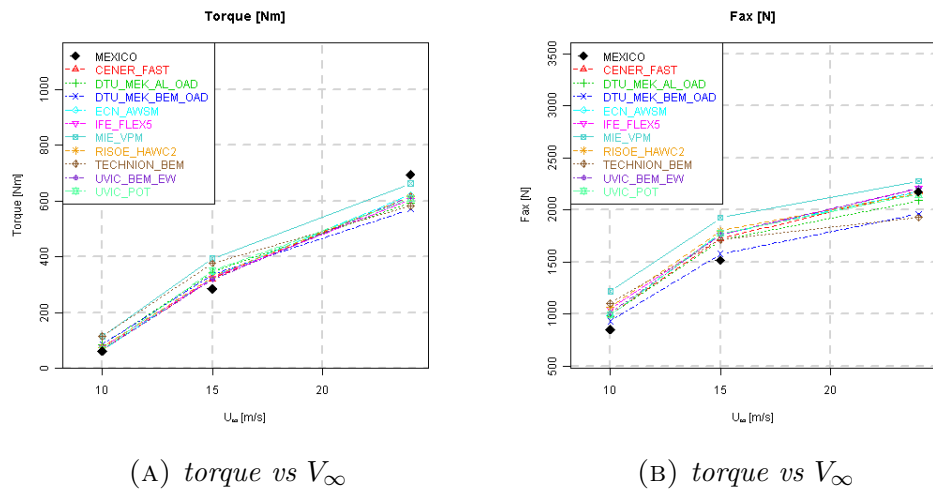


FIGURE 3.12: Turbine torque and thrust for various inflow velocity  $V_{\infty}$ .



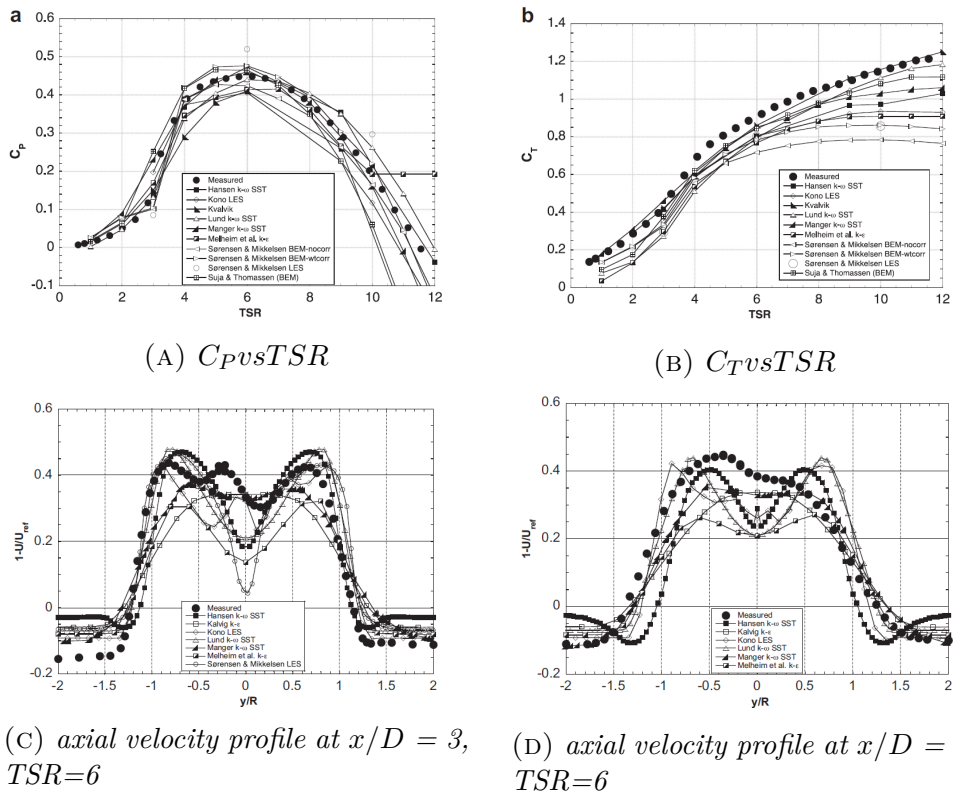


FIGURE 3.13: *Nowitech and Norcowe Blind Test 1*, measurement was made about coefficients of power and thrust vs  $TSR$ (a,b) and wake structure downstream the rotor(c, d)

## 3.6 Effective velocity evaluation

The poor results achieved by the existing codes in the above aerodynamic blind comparison tests motivate this thesis, in particular AL codes seem to work well in wake structure reproduction, for the localized force distribution, but the performance on loads reproduction is not of good level.

In AL, and also AD, the blade loads are directly calculated from tabulated airfoil data and blade relative velocity, a not correct estimation in force can be due to one of either this two factors. Blade data are inputs and then their correctness leaves aside the implementation of the code. However the correct estimation of the blade relative velocity can be seen as the core task of every aerodynamic model. In sections 3.3 and 3.4 it was said that the velocity on rotor or on the blade has to be evaluated, existing model implementations perform this evaluation in two ways:

- **BEM theory evaluation:** velocity on rotor plane can be calculated "a-priori", known mean wind inflow speed, one can calculate axial and tangential induction factor, relative velocity and blade lift and drag like described in section 3.3 and directly apply these forces in Navier-Stokes momentum equation. Literature examples of this velocity evaluation method can be found in [21], [31], [25], [32] and also numerous commercial codes [29], [19] use this approach because as said BEM theory is a well validated method. These methods however retain all the critical BEM aspects with unsteady inflow condition that can not be represented by a unique velocity value. Blades in logarithmic unsteady profile experience a strong variation in velocity value during their revolution that this method can fail. Furthermore evaluating loads from upstream undisturbed velocity is bad coupled with the the intention of interfacing the aerodynamic model with a structural one for aeroelastic analysis, for which it is necessary that loads are evaluated from local blade motion.
- **Local evaluation:** The main difference with BEM evaluation is that the link between the applied force on fluid is not provided by integral momentum conservation but directly from CFD resolved wind veloc-

ity field. The velocity over rotor  $\mathbf{U}$  of fig. 3.6 is not calculated from  $V_\infty$  with induction factors but sampling directly over rotor location from numerical solved velocity field [22], [23]. Sampling directly on rotor plane lets to evaluate the effective wind velocity impacting the blade for an higher coherency between actual flow encountered by blade and generated aerodynamics force. This method is presented in [16] from which numerous works derived, like [17], [23], [18] and code implementations are the DTU EllipSys3D and the NREL SOWFA open-source code [33].

The local velocity sampling is thus a more refined method, however it should be noticed that in AD method the force is distributed on the entire rotor area, this means that for every point on rotor plane the velocity can be sampled and used as reference wind velocity, in AL method this is true only on the azimuthal average, so it is necessary to correctly evaluate where to sample the velocity field. The loads applied by blade indeed deflect the flow making difficult a correct estimation of relative velocity angle. This is the problem of the determination of the angle of attack (AOA), the blade acts on the fluid modifying principally the angle of the relative velocity around the blade itself. This is explained by Kutta-Joukowski law, [34] the lift generated by blade defines the intensity of bound circulation around the blade section, for this reason if one samples the field just in front of the blade section will not find the effective relative velocity and AOA but something modified by bound circulation. Cited AL codes take as reference for relative velocity computation the wind speed sampled on the effective point of AL force application (eventually interpolating with various methods: linear or gradient correction). In theory the effect of vortex related to bound circulation is null at the precise force application point, but this assumption can not be absolutely true for various reasons related to CFD numerical approximation or unsteadiness of incoming flow. In this thesis a new method for evaluating the effective wind velocity seen by blade is proposed based to the work done by P. Schito [3]. This velocity evaluating method is called Effective Velocity Model (EVM) exactly as the output that it propose to provide a more robust and correct relative velocity evaluation trough the sampling of multiple points near the blade section position, in the next chapter a detailed EVM

derivation description will be proposed.

# Chapter 4

## AL methods validation in 2D and Effective Velocity Model set-up

In the previous chapter AL method was presented, applying the blade-element theory the force is computed on the blade cross-sectional plane, as for a 2-dimensional airfoil, and applied to the generic blade segment. For this reason AL model consistency has to be verified for a 2-dimensional case representative of the generic blade segment.

After having verified the correct reproduction of blade section with AL technique, the EVM methods will be detailed explained and derived. The last part of the chapter is dedicated to the non-steady analysis of the AL 2-dimensional case, showing the benefits deriving from the EVM application in this particular flow regime.

### 4.1 2-Dimensional study of AL method

In fig.4.1 turbine blade on the left is modeled in AL method with a line on which force is applied on the right, their equivalence have to be valid in every blade section.

For verifying this equivalence a comparison CFD test is performed, blade

section aerodynamics is simulated with a fully meshed airfoil section while AL section model is a single actuator force point, intersection of AL line with blade cross-sectional plane.

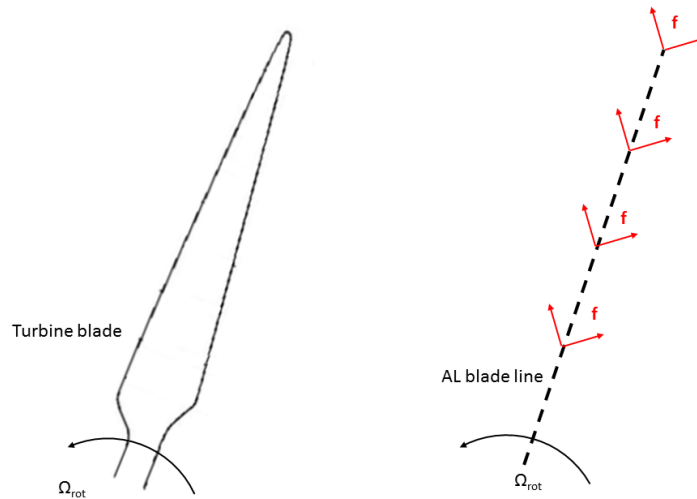


FIGURE 4.1: *Turbine blade and AL blade line model.*

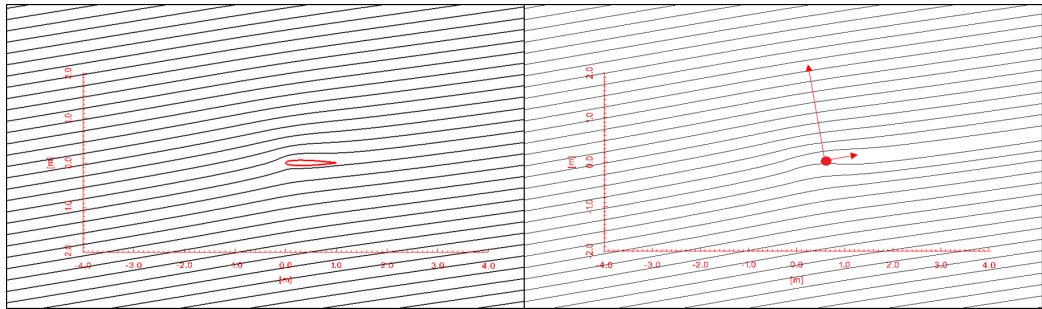


FIGURE 4.2: *Turbine blade section and AL line intersection point (AF section model).*

The fully meshed airfoil (FRA) and the actuator force (AF) point simulation are 2-dimensional simulation, both will be carried out with OpenFOAM incompressible steady solver SimpleFoam (based on simple algorithm). The goal of this comparison is to test the effective correspondence of the flow generated by AF force insertion and the flow established around the fully modeled airfoil section. Airfoil simulation are well established analysis in

CFD with small experimental error, this justify its use as blade section reference data and allow to assert that if the AF simulation can correctly model force and flow of FRA simulation then it can also model the behavior of a real blade section at least in steady simulation.

## 4.2 FRA simulation

Turbine blade are normally modeled using known and tabulated airfoils, in this exposition a NACA0012 airfoil, reported in fig.4.3, is arbitrary used as reference.

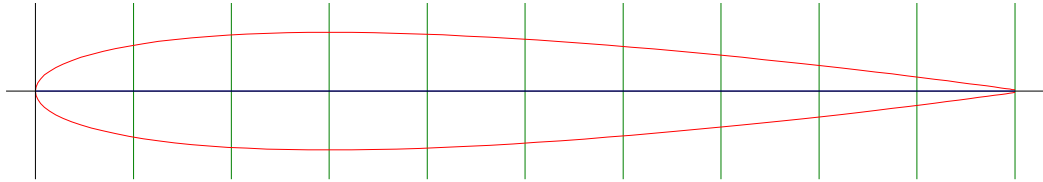


FIGURE 4.3: *NACA0012 symmetrical airfoil shape.*

From normed NACA0012 shape, fig.4.3, the computational mesh is generated and imported in OpenFOAM, airfoil chord is set equal to 1 m, the domain is square with a thickness of 0.01 m in plane normal direction, cells are prismatic with triangular base. Mesh structure is reported in fig. 4.29, while its characteristic are reported in tab. 4.1.

Table 4.1: NACA0012 mesh characteristics

mesh domain	50mx50m
number of cells	~430000
number of cell faces on airfoil patch	~1700
chord length(c)	1m
airfoil leading edge pos.	(0,0,0)

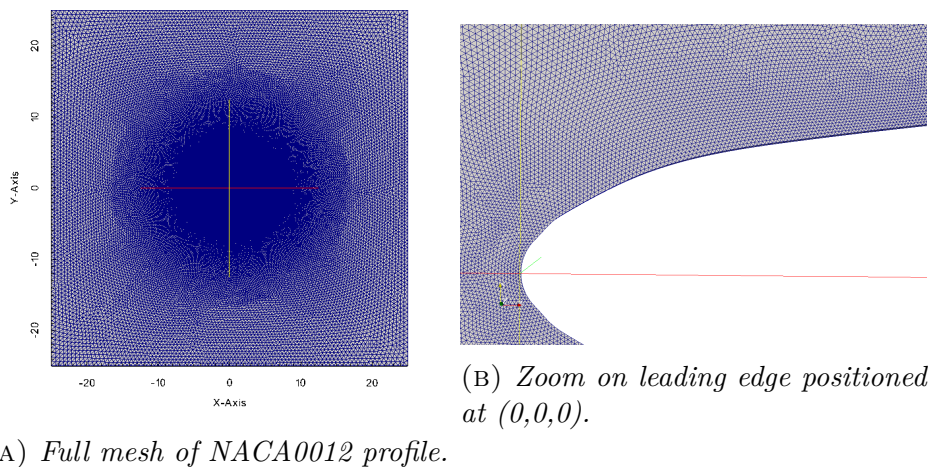


FIGURE 4.4: Mesh of NACA0012 profile.

### 4.2.1 Turbulence model

For FRA simulation Reynolds Averaged Navier-Stokes turbulence models are a common choice, in particular the  $\kappa - \omega$  *SST* model can give the best result in term of experimental data reproduction [35].  $\kappa - \omega$  *SST* is a two equations turbulence model, one in turbulent kinetic energy,  $k$ , and one in specific dissipation rate,  $\omega$ :

$$\frac{\partial k}{\partial t} + U_j \frac{\partial k}{\partial x_j} = P_k - \beta^* k \omega + \frac{\partial}{\partial x_j} \left[ (\nu + \sigma_k \nu_T) \frac{\partial k}{\partial x_j} \right] \quad (4.1)$$

$$\frac{\partial \omega}{\partial t} + U_j \frac{\partial \omega}{\partial x_j} = \alpha S^2 - \beta \omega^2 + \frac{\partial}{\partial x_j} \left[ (\nu + \sigma_\omega \nu_T) \frac{\partial \omega}{\partial x_j} \right] + 2(1 - F_1) \sigma_\omega \frac{1}{\omega} \frac{\partial k}{\partial x_i} \frac{\partial \omega}{\partial x_i} \quad (4.2)$$

$$\nu_T = \frac{a_1 k}{\max(a_1 \omega, SF_2)} \quad (4.3)$$

Resolving the two scalar fields  $k$ ,  $\omega$  allows to estimate the turbulent viscosity,  $\nu_T$ , and closes the RANS equation by modeling Reynolds stresses tensor according to Boussinesq hypothesis. In particular the  $\kappa - \omega$  *SST* model is very powerful for its capacity to combine the best of  $k - \epsilon$  and  $k - \omega$  models: the function  $F_1$  has unit value near surface wall, so this activates the  $k - \omega$  model that perform well in reproducing Reynolds stresses in wall



boundary layer, while assume zero value in free stream zone activating the  $k - \epsilon$  model. The model works well not only in reproduction airfoil boundary layer stress, but also in the free wake zone. Detailed description about all the model variables can be found in Menter [36] which is the theoretical base of OpenFOAM  $\kappa - \omega$  *SST* model implementation.

#### 4.2.2 Boundary definition

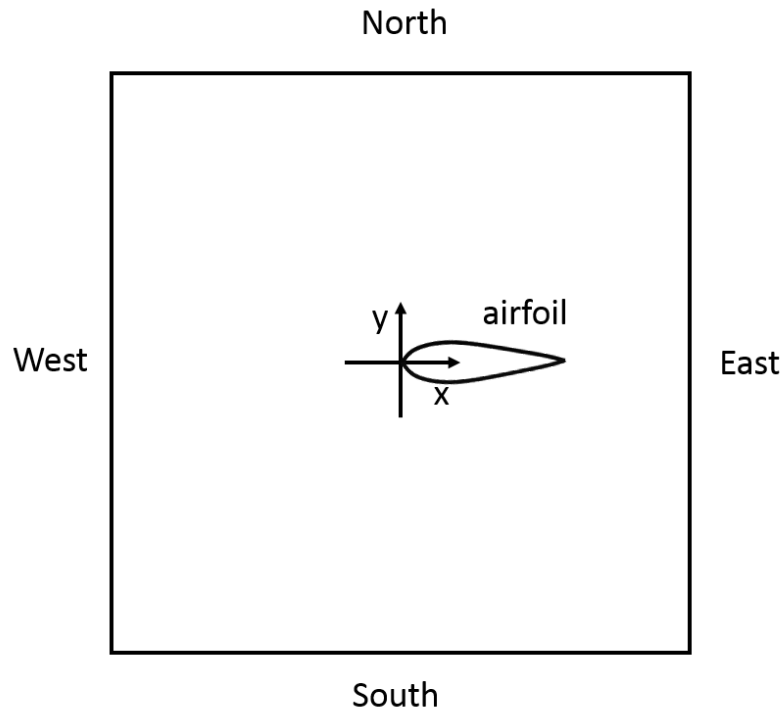


FIGURE 4.5: *2-dimensional case boundaries.*

In FRA a total of five boundary patches are present, see fig. 4.5, the three walls West, North and South are set as inlet boundaries, while East patch is the outlet boundary, see tab.4.7 for details.

Being the inlet on West, North and South boundaries a Dirichlet condition is imposed, on East boundary a Neumann null gradient condition is applied, on the airfoil patch no-slip condition is set for velocity, wall function were used for  $k$  and  $\omega$  and the  $Y^+$  maximum value is approximately 15.

Table 4.2: FRA boundary condition

boundary	U	p	k	$\omega$
West	fixedValue= $\mathbf{V}_\infty$	zeroGradient	fixedValue=0	fixedValue=1
North	fixedValue= $\mathbf{V}_\infty$	zeroGradient	fixedValue=0	fixedValue=1
South	fixedValue= $\mathbf{V}_\infty$	zeroGradient	fixedValue=0	fixedValue=1
East	zeroGradient	fixedValue=0	zeroGradient	zeroGradient
Airfoil	fixedValue=0	zeroGradient	kqRWallFunction	omegaWallFunction

### 4.2.3 Polar curves extraction

As first step a series of steady state simulations, for different angles of attack were carried out. These first phase allowed the construction of reference polar curves for the NACA0012 profile, together with the flow field generated around the airfoil at every incidence angle, such data will be later used for AF comparison.

Table 4.3: NACA0012 polar curves simulation

$V_\infty$	10 <i>m/s</i>
$\nu$	$1.78 \times 10^{-5}$
$\text{Re}=(V_\infty c)/\nu$	$5.5 \times 10^5$
tested AOA	-20:2:20 deg

At this stage it was not searched for an absolute correspondence between the simulated and experimental values of the studied airfoil. The main goal was only to build up a reference dataset for the fully meshed profile case, however the founded curves for coefficient of lift and drag, reported in fig.4.6, show a good agreement with Abbott and Von Doenhoff (1959) [37] and Johansen (1997) [38] literature experimental data for NACA0012 airfoil.

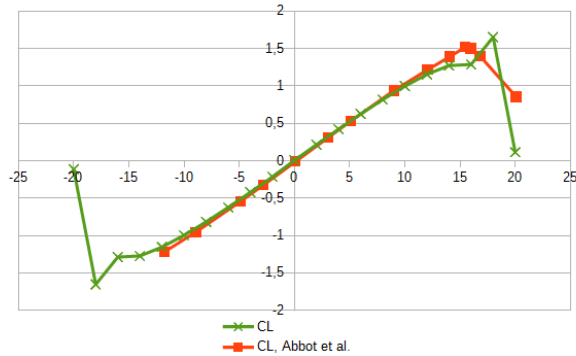
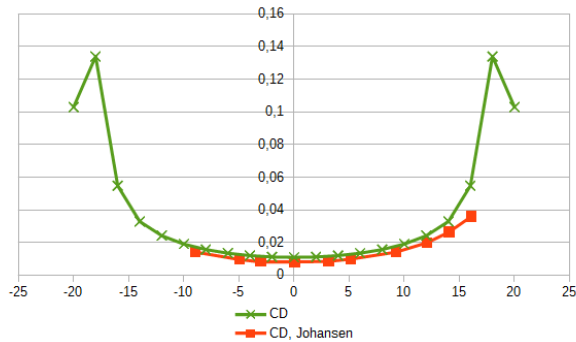

 (A) *NACA0012, lift coefficient  $C_L$ .*

 (B) *NACA0012, drag coefficient  $C_D$ .*

 FIGURE 4.6: *NACA0012 computed polar curves vs literature experimental data.*

### 4.3 AF simulation

The same NACA0012 studied in FRA simulation was then simulated using AF method. For AF simulation the mesh was a fully regular one, with only square base hexagonal cells, the overall domain is equal to FRA one and so are the boundary conditions and the used turbulence model. Obviously the airfoil boundary is no more present and a volume force is instead inserted in Navier-Stokes equation like in (3.23), OpenFOAMs `simpleFoam` solver momentum equation is modified for force insertion as:

```
tmp<fvVectorMatrix> UEqn
(
    fvm::div(phi, U)
```

```

+ volumeForce
+ turbulence->divDevReff(U)
==
fvOptions(U)
);

```

Known the angle of attack `volumeForce` is calculated from FRA extracted polar curves as:

$$\mathbf{L} = \frac{1}{2} \rho V_{rel}^2 C_L(\alpha) c t \mathbf{l} \quad (4.4)$$

$$\mathbf{D} = \frac{1}{2} \rho V_{rel}^2 C_D(\alpha) c t \mathbf{d} \quad (4.5)$$

$$volumeForce = \frac{L + D}{V_{cell}} \quad (4.6)$$

where  $C_L(\alpha)$ ,  $C_D(\alpha)$  are the coefficients of lift and drag of NACA0012 airfoil tabulated in section 4.2.3,  $V_{rel}$  is the relative velocity seen by AF modelled airfoil and  $t$  is the mesh thickness in plane normal direction. AF simulation

Table 4.4: AF mesh characteristics

mesh domain	50mx50m
number of cells	2550-10100-40200
$l_{cell}$	1m-0.5m-0.25m
force point.	(0.25m,0m,0m)

has been carried out with different mesh refinement levels, reported in tab. 4.4, an important parameter is the ratio between the simulated airfoil section chord,  $c$ , and AF computational cell length,  $c/l_{cell}$ , this is a non-dimensional value describing the level of AF mesh refinement relatively to the airfoil dimension. The force point position of AF simulation is placed at the airfoil pressure center, which is located approximately at the chord quarter. This location is chosen due to the fact that it is impossible to reproduce an aerodynamic moment with a concentrated force, so the point with zero aerodynamic moment is the pressure center.

### 4.3.1 Regularization Kernel application

Although the more physical place to insert the body force in AF simulation is the singular cell containing the airfoil pressure center, this is however not recommended due to numerical problems in CFD integration. Indeed a concentrated source force in discrete solved momentum equation leads to great gradient in the solution that can induce numerical oscillations that affect solution accuracy. This is a known problem in CFD applications always present in resolving sharp gradient conditions [39], already faced by Sorensen in his first AD implementation [22]. An interesting consideration can be found in Masson's studies [25] of numerical oscillation in AD implementations: Masson pointed out that a direct application of source force in numerical solved Navier-Stokes equation will inevitably produce a solution with unrealistic spatial oscillations near the permeable surfaces formed by applied force computational cells.

The spatial oscillation problem afflicts co-located numerical methods for CFD equation solving, like the used OpenFOAM. Different methods to treat numerical oscillations exist and have been applied by various researchers. For example a non linear filter can be applied that searches for the oscillation peaks and suppress them in post-processing [22]; Masson managed to suppress oscillations by applying the force source not as volume force in Navier-Stokes momentum equation but as pressure discontinuity on the desired CFD cells. The most utilized oscillations treatment option [16], [21], [23], [17], [33] is however the adoption of a smearing function, which prescribes that the force is not directly inserted in the cells where rotor or blade yields but it is distributed on multiple cells to avoid too much steep gradient in solution.

The normal used smearing function is a 3-dimensional Gaussian function called Regularization Kernel (RK):

$$\eta^{RK}(r) = \frac{1}{\epsilon^3 \pi^{3/2}} \exp\left[-\left(\frac{d^2}{\epsilon}\right)\right] \quad (4.7)$$

where  $d$  is the generic CFD cell distance from applied force application point and  $\epsilon$  is the RK width parameter.

Applying a smearing function means that in every domain cell the total

inserted force is the discrete convolution of computed disk or blade line force and  $\eta^{RK}$  :

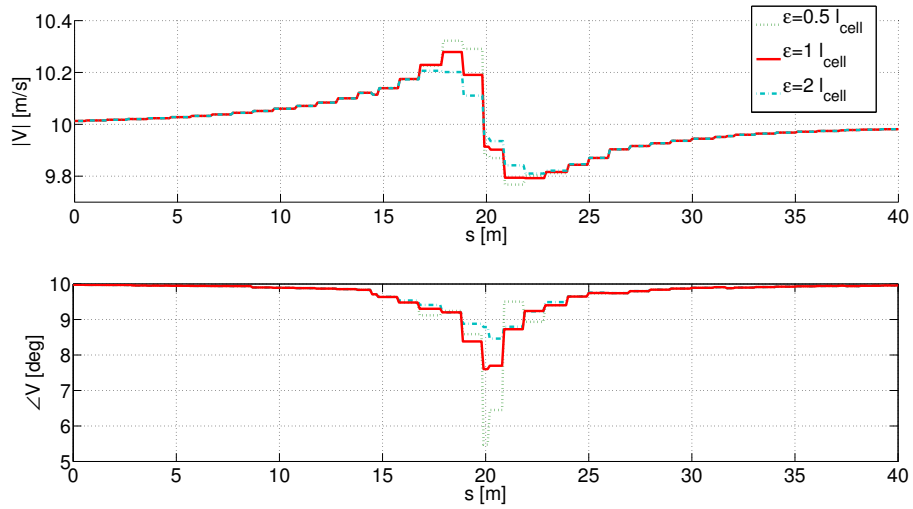
$$\mathbf{f}(\mathbf{x}) = \sum_i \mathbf{f}^i \eta^{RK} (|\mathbf{x} - \mathbf{x}^i|) \quad (4.8)$$

where  $i$  is the index of all the rotor disk or line cell,  $\mathbf{x}^i$  is the cell position and  $\mathbf{f}^i$  is the associated applied force, on the other hand  $\mathbf{x}$  is the position of the generic CFD cell and  $\mathbf{f}(\mathbf{x})$  is the resultant force. Applying a regularization kernel function surely makes the numerical solution more robust but also decrease the capacity of AD and in particular AL to grasp local aerodynamic effect, in a few words makes them "less sharp instruments".

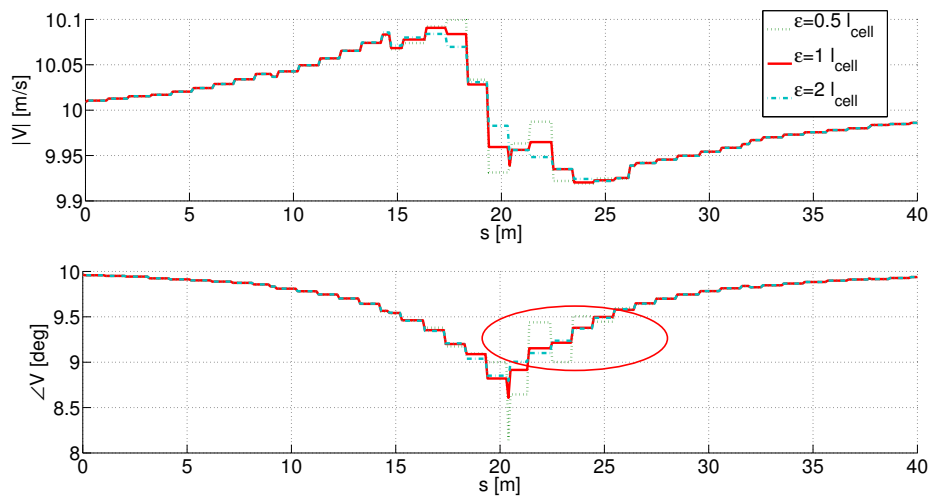
For AF simulation of blade section a 2-dimensional  $\eta^{RK}$  is used based on normal Gaussian distribution of two independent variables:

$$\eta^{RK}_{2D}(r) = \frac{1}{\sqrt{\epsilon^4(2\pi)^2}} \exp \left[ - \left( \frac{1}{2} \frac{d^2}{\epsilon^2} \right) \right] \quad (4.9)$$

being based on bi-variate normal function the force distribution area imposed by  $\eta^{RK}_{2D}$  is easy to calculate, 68.3% of force is contained in circle of radius  $\epsilon$ , 95.5% in a  $2\epsilon$  radius circle and 99.7% when the radius is equal to  $3\epsilon$ . Regularization kernel width has to be related to the computational cell dimension: in literature different optimal values can be found, but usually  $\epsilon$  is prescribed to be at least 2 times the computational cell length to avoid numerical errors. In this work the value of  $\epsilon$  is set with a precise method. For a cell length,  $l_{cell}$ , fixed to 1 m,  $\epsilon$  in the range  $[0.5; 2] l_{cell}$  were tested and the smallest value for which spatial oscillations in velocity were not observed is taken as optimum.



(A) Probe line  $d = 2c$

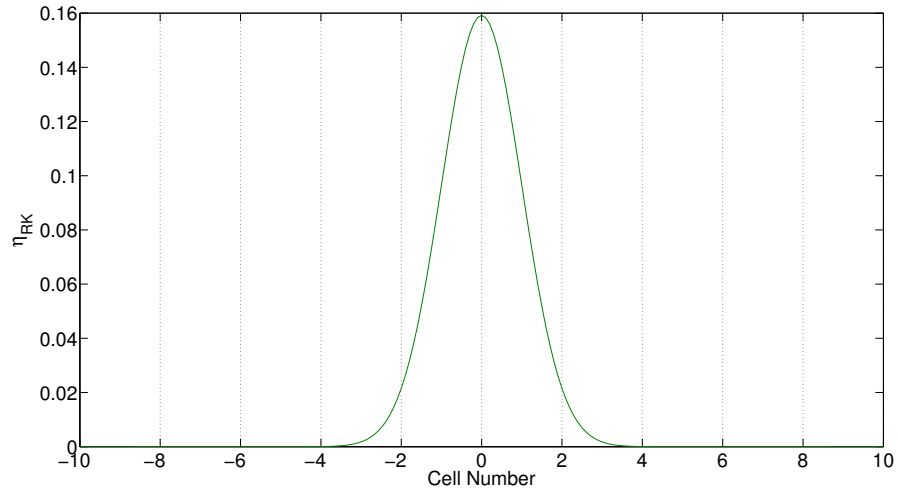


(B) probe line  $d = 5c$

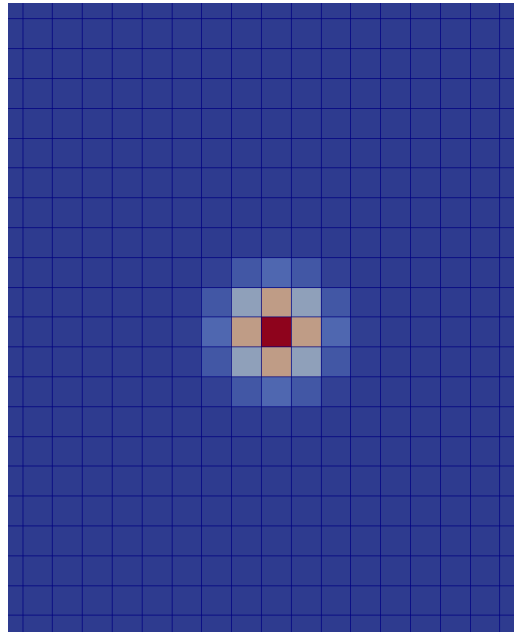
FIGURE 4.7: Velocity sampled of downstream probe lines is plotted in magnitude (upper sub-plots) and phase (lower sub-plots) for 2 m and 5 m downstream the probe lines.

In fig. 4.7 velocity sampled on two lines, described in section 4.4.1, is reported, while in the highlighted red ellipse of fig. 4.7b are clearly visible some oscillations mainly in velocity phase but also in magnitude. As said, this output comes from steady state simulations, so these differences in velocity from two layer of fluids do not have physical explanation, since viscosity should cancel the relative velocity between the adjacent fluid layers. This numerical test optimize the Regularization Kernel width, so the smallest  $\epsilon$  for which this phenomenon is not observed was found to be  $1l_{cell}$ . From this point  $\eta^{RK}$  width is kept constant to  $1l_{cell}$  in every successive simulation and reported in fig. 4.8.





(A) Analytical curve of the regularization kernel.



(B) Force smearing effect on computational cells. Red means high volume force value, blue corresponds to the minimum.

FIGURE 4.8: Regularization kernel distribution function and visualization in the computational domain.

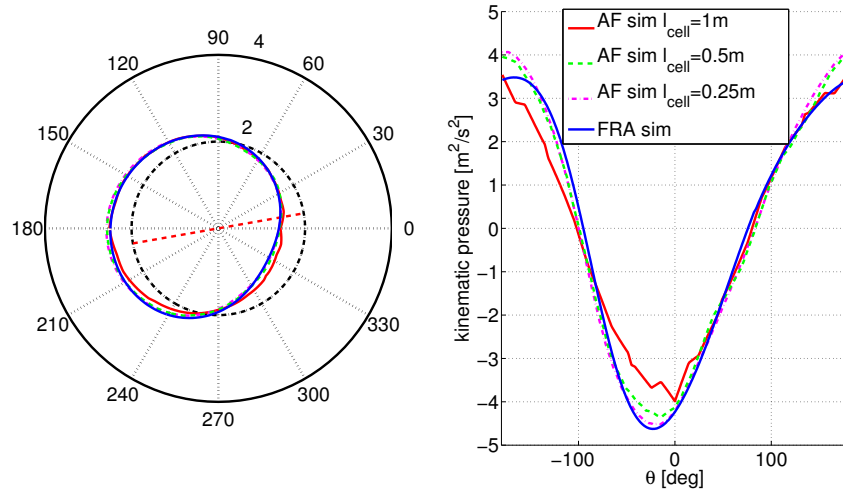
## 4.4 Flow reproduction

After Regularization Kernel optimization, the first thing to be verified is the correctness of flow computed with the AF model against the FRA one. For a fixed  $\mathbf{V}_\infty$  the force integrated on NACA0012 boundary in FRA simulation is inserted as volume force term in AF:

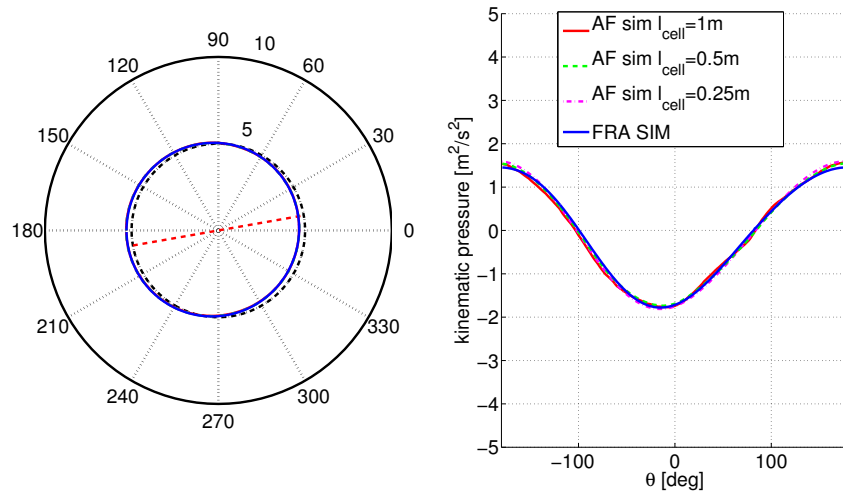
$$volumeForce = F_x^{FRA} \mathbf{x} + F_y^{FRA} \mathbf{y} \quad (4.10)$$

where  $F_x^{FRA}$  and  $F_y^{FRA}$  were found for different angles in sect.4.2.3. It should be noticed that it would be the same to substitute  $V_{rel} = V_\infty$  and  $\alpha = \angle V_\infty$  in (4.4)-(4.6). Then, for a chosen  $\mathbf{V}_\infty$  angle of  $10^\circ$  and magnitude of 10 m/s, the AF simulation reached convergence and the flow computed is directly compared to the FRA one. With OpenFOAMpost-processing sampling tools the pressure field around FRA airfoil boundary and AF force point is sampled on circle paths, reported in fig.4.13, if AF volumeForce has the correct value the pressure fields of the two simulation have to be very similar.

The pressure probes circle contours of radius 2 m and 5 m are centered on the mesh origin for both AF and FRA simulation. The pressure distributions, plotted in fig.4.9a and 4.9b, show a good agreement between FRA and AF model, the pressure profile of the two models do not have angular misalignment thanks to the correspondence of AF force point and FRA pressure center. Agreements in results increase for increasing mesh refinement level which is a sign of effectiveness of the model.



(A) Pressure on circle contour of radius  $R = 2$  m: on the left pressure distribution is plotted non-dimensionally over the probe circle, on the right the kinematic pressure is plotted against azimuthal coordinate.



(B) Pressure on circle contour of radius  $R = 5$  m: on the left pressure distribution is plotted non-dimensionally over the probe circle, on the right the kinematic pressure is plotted against azimuthal coordinate.

FIGURE 4.9: Pressure field on surrounded contours: comparison between FRA and AF calculations.

A direct velocity field comparison is made possible with OpenFOAM application `mapFields`, that permits numerical computed fields interpolation between different mesh with different structures. The FRA results are interpolated on AF mesh and the relative error between the two simulations is calculated in every computational cell, reported as:

$$err_{|\mathbf{V}|}(cell_i) = \frac{(|\mathbf{V}|_{AF}(cell_i) - |\mathbf{V}|_{FRA}(cell_i))}{|\mathbf{V}|_{FRA}(cell_i)} \quad (4.11)$$

$$err_{\angle \mathbf{V}}(cell_i) = \frac{|\angle \mathbf{V}_{AF}(cell_i) - \angle \mathbf{V}_{FRA}(cell_i)|}{|\angle \mathbf{V}_{FRA}(cell_i)|} \quad (4.12)$$

where  $\mathbf{V}_{FRA}(cell_i)$  is the velocity value from FRA simulation interpolated on  $cell_i$  cell of AF simulation,  $\mathbf{V}_{AF}(cell_i)$  is the velocity value from AF simulation in  $cell_i$ . The results are reported in fig. 4.10, 4.11 and 4.12 and once again it is found a good agreement between AF and FRA results: the computed velocity field error is globally small and concentrated very near the airfoil position where it is almost impossible to correctly reproduce the correct flow with a simplified method like AF.

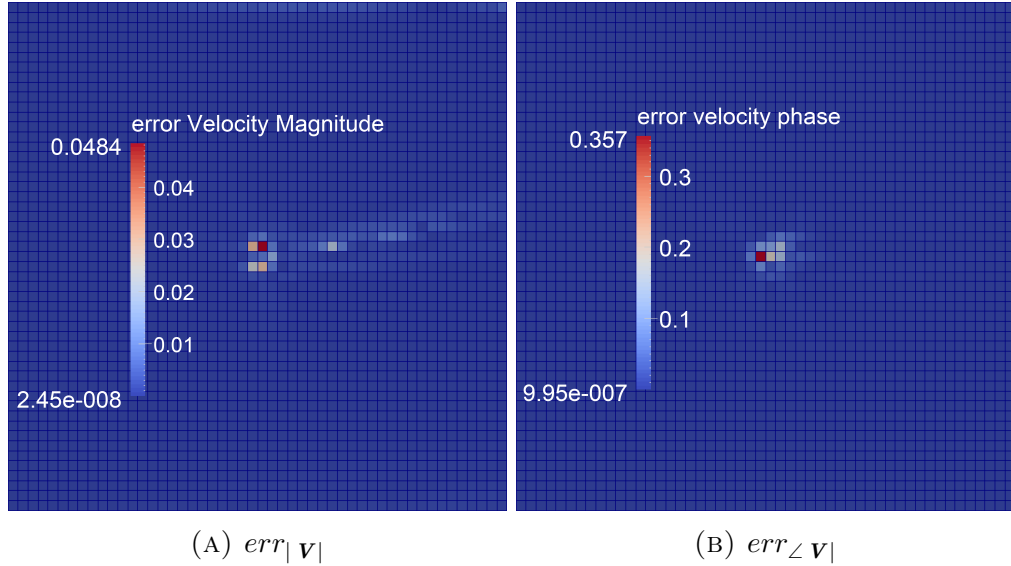


FIGURE 4.10: *AF - FRA relative error on velocity for AF  $c/l_{cell} = 1$  ( $l_{cell} = 1$  m).*

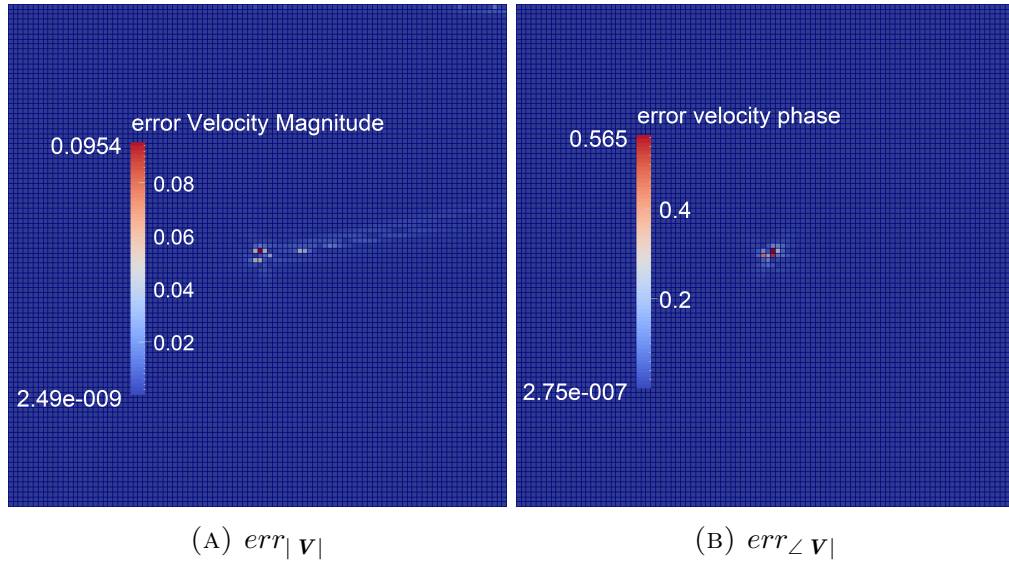


FIGURE 4.11: *AF-FRA relative error on velocity for AF  $c/l_{cell} = 2$  ( $l_{cell} = 0.5$  m).*

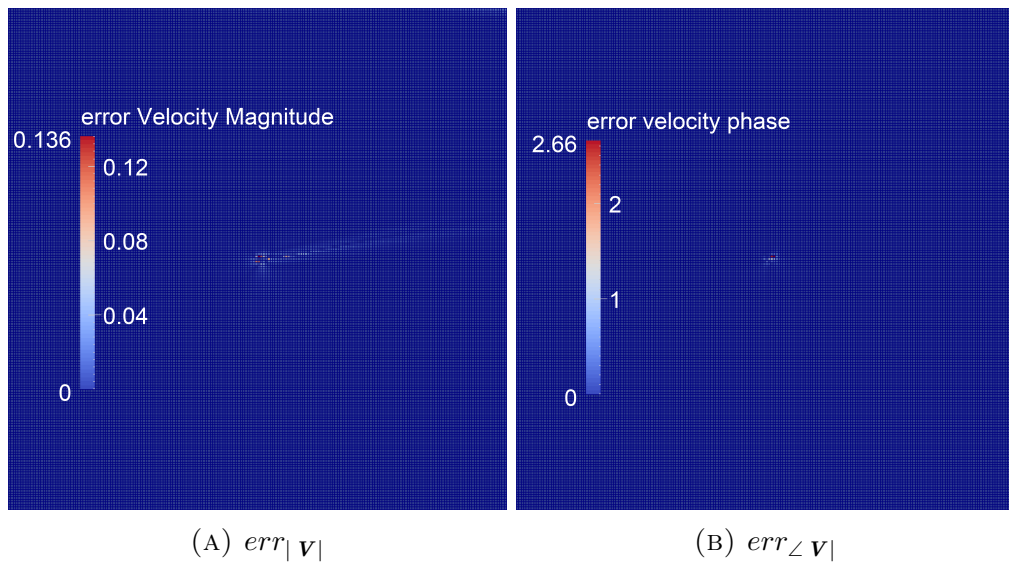


FIGURE 4.12: *AF - FRA relative error on velocity for AF  $c/l_{cell} = 4$  ( $l_{cell} = 0.25$  m).*

### 4.4.1 Wake reproduction

As said in chapter 3 a fundamental task for turbine aerodynamic model is the correct reproduction of the generated wake. Therefore it was performed a detailed comparison of the wake generated by AF simulation against wake generated by FRA simulation, the correct reproduction of wake of airfoil section is the foundation of the correct reproduction of the entire turbine wake. For this comparison velocity probes line are placed downstream the airfoil or the force application point, in the same position for FRA and AF simulations. Lines are defined to be perpendicular to boundary  $V_\infty$ , the line length measures 40 m with 401 probe points per line. Lines mid point is placed at the center of the wake. A total of 6 lines are placed at 1; 2; 3; 5; 10; 20 m downstream, reported in fig. 4.13 as red dashed lines. In fig.

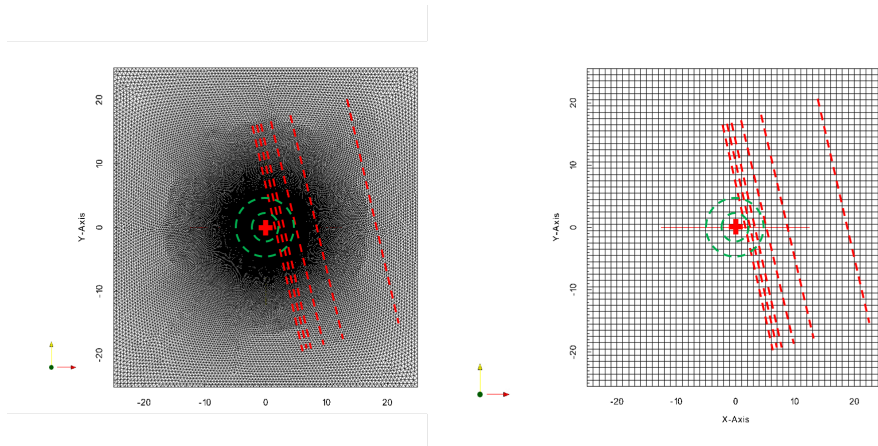
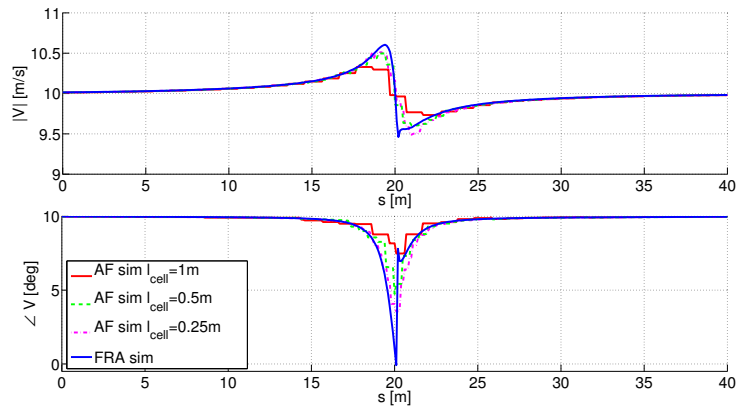


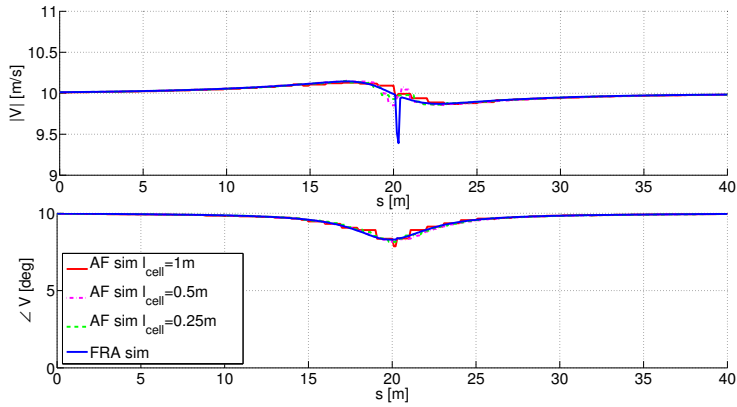
FIGURE 4.13: A series of probe lines are placed in both FRA and AF simulation for wake comparison.

4.9 and 4.14 the comparison results are again reported for  $V_\infty = 10m/s$  and  $\angle V_\infty = 10^\circ$  and different mesh refinement levels.

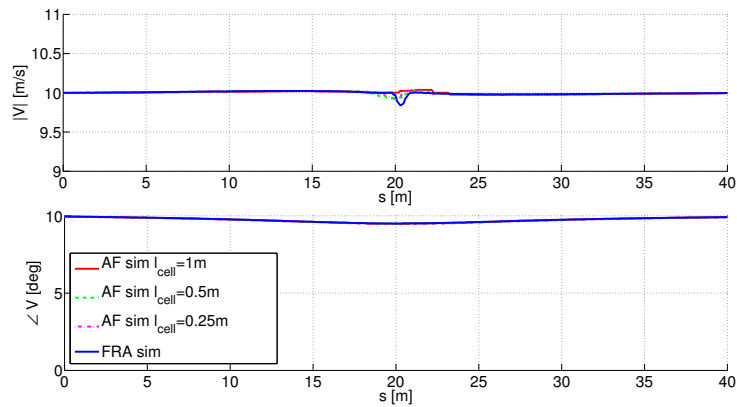
From the wake sampled velocity in fig.4.14a-4.14b, error decreases for mesh refinement increasing level and as one samples farther in the wake. In fig.4.14a the AF simulation with  $l_{cell} = 0.25$  m is the one that better captures the down-wash in wake velocity phase.



(A) Velocity sampled in wake 1m downstream, top sub-plot refers to the magnitude, bottom sub-plot to the phase.



(B) Velocity sampled in wake 3m downstream, top sub-plot refers to the magnitude, bottom sub-plot to the phase.



(C) Velocity sampled in wake 10m downstream, top sub-plot refers to the magnitude, bottom sub-plot to the phase.

FIGURE 4.14: Wake velocity comparison between FRA and AF calculation wake velocity, on the x-axis the coordinate  $s$  is the distance on sampling line from line upper extreme point.

## 4.5 Aerodynamic force estimation

In section 4.4 the correctness of AF model flow reproduction has been proved, however the inserted force in AF simulation was directly put equal the correspondent force integrated in FRA simulation for the same magnitude and angle of  $\mathbf{V}_\infty$ , in other words the airfoil relative velocity was considered known from the boundary conditions. In turbine simulation with AL methods the force to be inserted can not be known "a-priori", the velocity on rotor is not equal to the one defined at boundary (see section 3.2) and it have to be evaluated directly at runtime. This means that there is the necessity of an algorithm able to correctly output the relative velocity of every blade section reproduced with AL model and thus uses this data for the force estimation with blade section tabulated airfoil data, as reported in eqn. (3.34) and eqn. (3.38).

In section 3.6 an overview of exiting methods for force evaluation in AL models were proposed, excluding the BEM theory evaluation for the motivation already expressed, a possible method is, as said, the "Local evaluation" one (LM). This method takes as hypothesis the Biot-Savart together with Kutta-Joukowski law [40] and makes the assumption of null effect of bound vortex induced velocity if one samples on the force application point [18]. This approach has three main weakness:

- **Velocity gradient:** lift generated bound vortex involves an up-wash (local velocity angle increase) in front lift generation point and a down-wash (local velocity angle decrease) behind the point, thus local angle must pass to undisturbed value in somewhere near the force point. However the area near force point is also characterized by the strongest value in velocity angle gradient, this means that a small error in velocity sampling point can lead to great errors in velocity angle evaluation.
- **Potential flow:** both Biot-Savart and Kutta-Joukowski laws are formulated in potential inviscid flow theory and then their validity is not full in turbulent viscid unsteady flow, like the one encountered by wind turbine in normal operation, moreover using CFD discretized method is another big difference from analytic framework behind those theory



and thus another motivation of not precisely valid assumption.

- **Turbulent flow:** sampling on local application point means sampling on a single point, in strong turbulent flow (like in up-stream turbine wake) there is not the certainty that the velocity in this point can represent the entire unsteady incoming flow information, since turbulence is a spatial phenomenon and thus it is somehow difficult to characterize it with a single sample.

This limitation in LM can justify the poor results achieved by existing code described in section 3.5. For this reason the EVM model is here proposed. Its name, Effective Velocity Model, recalls the idea of evaluating from inflow velocity field the equivalent undisturbed incident velocity to the airfoil and then to use this value to correctly interpolate the airfoil tabulated polar curves. In the next subsections the fundamental assumptions and the set-up of the EVM will be presented in detail.

#### 4.5.1 Description and tuning of the EVM

The core of EVM is to effectively use the big amount of information provided by CFD code about blade incoming flow, this method was conceived by P. Schito [3], and can be somehow considered as a middle way between "BEM theory evaluation" and LM. Velocity is not sampled far upstream the rotor to keep the time coherency of flow-force but neither is sampled on the very blade point, velocity is evaluated a little upstream (some chord length) the blade position, this permits to sample on an area with less strong velocity angle gradients, see fig.??, and consequently build up a more robust algorithm anyhow without losing too much flow-force time coherency. Furthermore velocity is evaluated on a sample segment, and thus on multiple points, positioned perpendicular to the mean relative velocity direction, this allows a more complete representation in non-uniform flow of incoming wind characteristics. Blade relative velocity evaluation based on close upstream sampling have already been presented [40] but they use a single sample point and also use the Biot-Savart vortex law for compute the induced velocity to be purified from sample one, in fig. ???. In this work the synthesis of the

EVM is not based on analytical theory but is calibrated with a series of numerical simulation based on the equality of the flow fields between the simulation of the FRA and the one related to the AF. The first goal was to define the sample line through which the incoming velocity is evaluated. In the following, the construction of the EVM is explained step by step.

### Positioning the sample line

The first step involves the setting of the sample line and its position in the computational domain relating to the AF point. In section 4.4 the error between AF and FRA simulation has been mapped, in this work the FRA simulation was considered representative of the real flow around a physical airfoil, hence where the AF error is high the AF calculated velocity have no physical meaning. For this reason the EVM sampling line has to be placed where there is good agreement in AF and FRA computed value.

An analysis identical to the one proposed in section 4.4.1, where the sampling line is perpendicular to  $\mathbf{V}_\infty$  with length of 40m, was carried out with the difference that the sampling line is placed in front and not behind the airfoil position in FRA and force point in AF. Sampling lines are reported in fig. 4.15. In this phase only AF mesh with  $l_{cell} = 1\text{m}$  was considered.

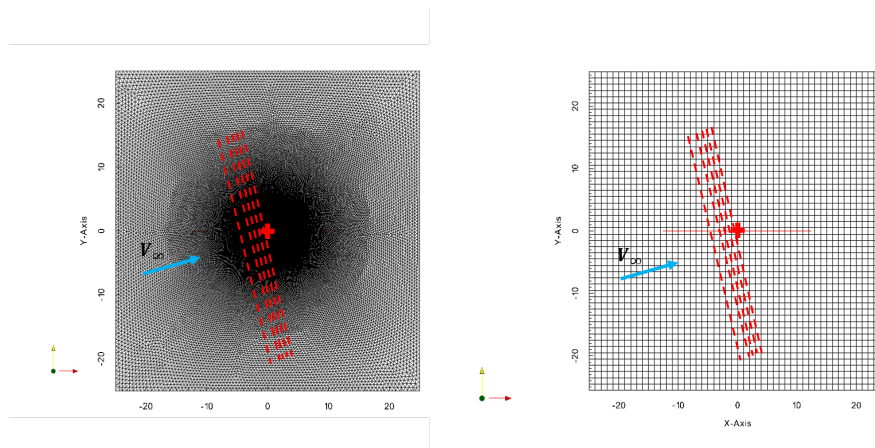


FIGURE 4.15: *EVM sampling line set-up: sampling lines (red dashed lines) placed upstream for both AF and FRA simulation, at distance = 0.5; 1; 1.5; 2; 3 m*

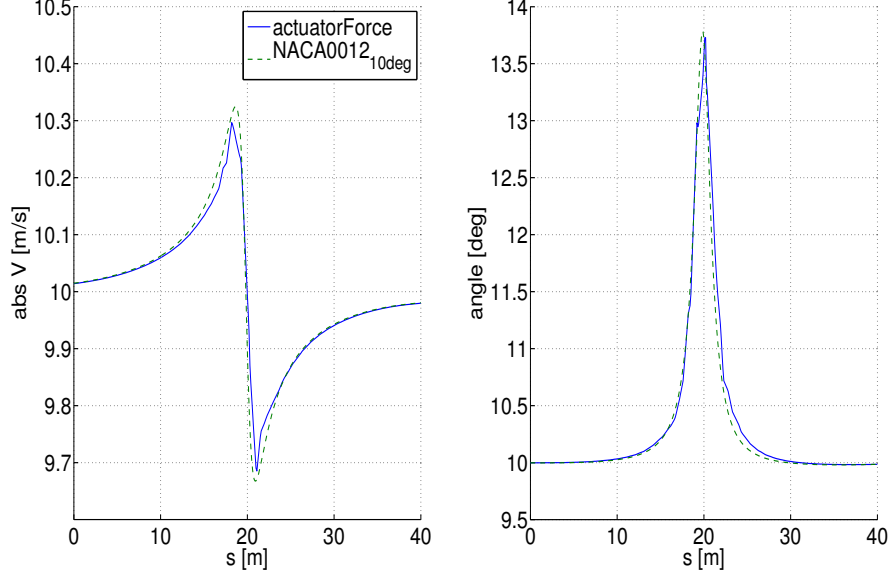


FIGURE 4.16: Comparison between the FRA and the AF simulations on  $U$  (magnitude and angle) function of the coordinate  $s$ , detected on the line placed 1.5 m in front of the AF point.

In order to establish the best position for the sampling line of the EVM, the relative errors in terms of absolute value and angle of the velocity between the FRA and the AF simulations have been integrated on the sample lines length,  $l_{sp}$ :

$$err_{|\mathbf{v}|}(d) = \int_0^{l_{sp}} \frac{(|\mathbf{V}|_{AF}(s) - |\mathbf{V}|_{FRA}(s))}{|\mathbf{V}|_{FRA}(s)} ds \quad (4.13)$$

$$err_{\angle \mathbf{v}}(d) = \int_0^{l_{sp}} \frac{(\angle \mathbf{V}_{AF}(s) - \angle \mathbf{V}_{FRA}(s))}{|\angle \mathbf{V}_{FRA}(s)|} ds \quad (4.14)$$

where  $d$  is the upstream distance of the sampling line. An example is shown in fig. 4.16

Especially taking into account the angular error, the tested AF case shows that a good compromise between the error values and the distance of the line, that should be as close as possible to better represent the instantaneous velocity value investing the AF point, is reached when the sampling line is positioned at a distance equal 1.5 m, as can be deduced from the plot of fig.

4.17.

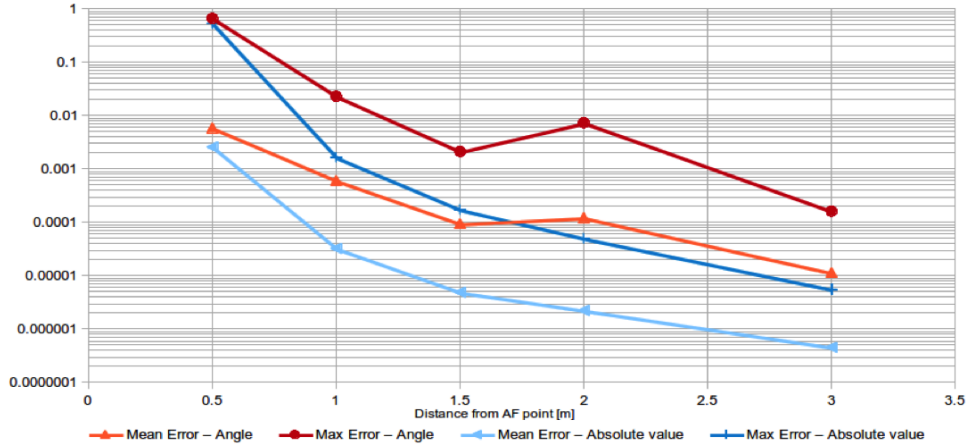


FIGURE 4.17: Trends of the errors on  $U$  relative to the AF simulation compared to FRA. The values are normalized respect to their maximum.

### Length of the sample line

The second step deals again with a comparison between the FRA and the AF simulation, but the purpose now is the definition of the length of the EVM sampling line. Focusing on the chosen line placed at a distance of 1.5 times the mesh dimension upstream the AF point and set a new coordinate  $q$  (representative of the portion of the line that is considered), a new examination of the two simulations is done. For each value of  $q$ , between 0 and the total length of the line,  $\Delta\alpha$  is calculated, where

$$\Delta\alpha = \text{mean}(\alpha(q)) - \alpha_\infty \quad (4.15)$$

both for FRA and the AF. As can be easily supposed, the relative difference between the curves decreases increasing the portion of sampling line considered coordinate, because a long segment takes into account also the information given by the cells that are far from the airfoil position. Also in this case a good compromise is needed and through the analysis of the second plots on fig. 4.18, it is arbitrary chosen a width of 5 times the mesh dimension  $l_{cell}$  for the EVM sampling segment. As can be seen by the mentioned

plot for a segment of 5 m the descendant trend of the relative difference between FRA and AF simulations is clearly visible. In fig. 4.19 is represented the chosen position of the EVM sampling line in the computational domain respect to the AF point.

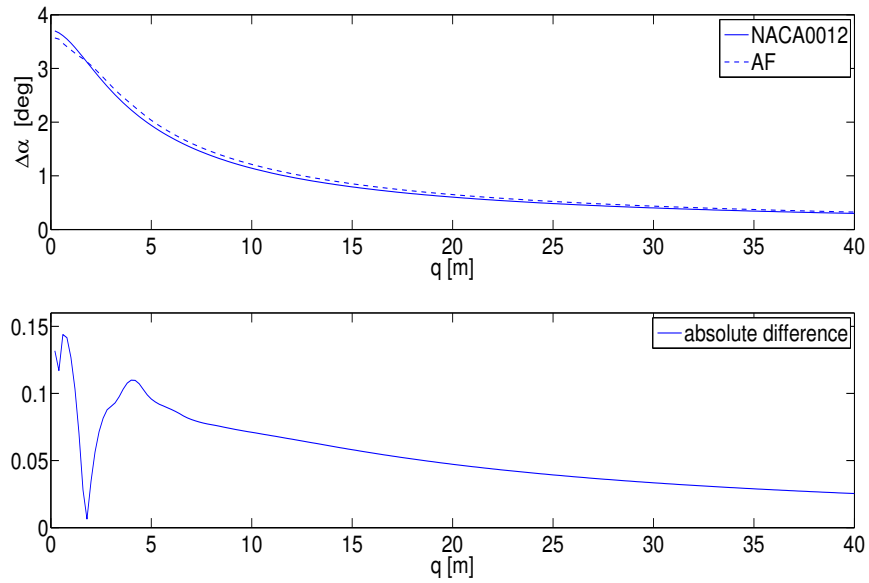


FIGURE 4.18: *Difference between  $\Delta\alpha$  detected by FRA and AF simulations and their computed absolute difference function of the coordinate  $q$ .*

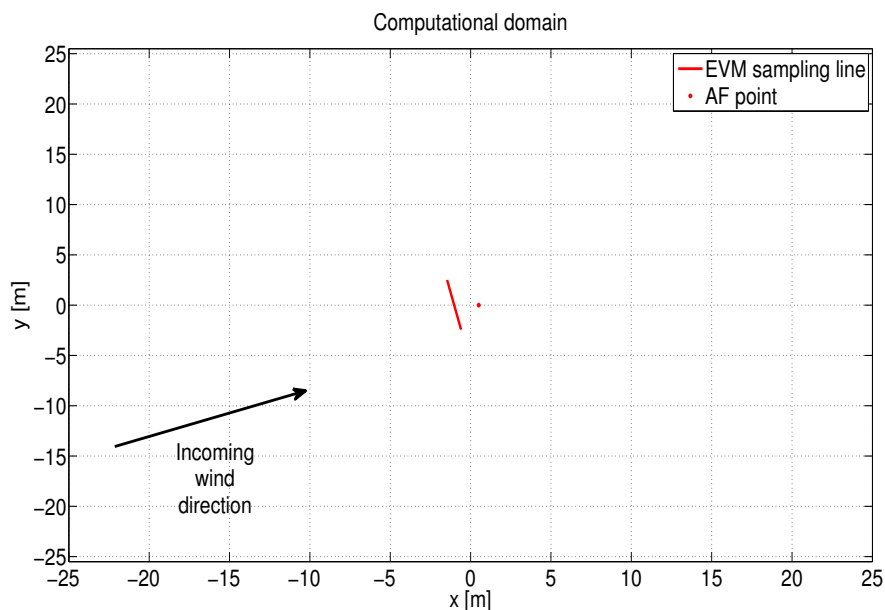


FIGURE 4.19: *EVM line and AF position in the computational domain.*

### Relationship between the local and undisturbed AOA

The aim of the third phase of the EVM construction is the definition of the empirical formula relating the angle detected by the EVM close to the profile and the undisturbed angle used to calculate and then to apply the aerodynamic forces delivered by the airfoil. The idea for this model is that the mentioned formula is given in terms of a correction that must be applied to the angle of  $\alpha$  provided by the EVM. Considering that the generic aerodynamic force (lift or drag) is defined as prescribed in eqn. (3.18) and (3.19), it is intuitive to suppose that the  $\Delta\alpha$  relation is dependent by the parameters directly influencing the forces:

$$\Delta\alpha = \alpha_{EVM} - \alpha_{\infty} = \Delta\alpha(C_L, C_D, \frac{c}{l_{cell}}) \quad (4.16)$$

where  $\alpha_{EVM}$  is the calculated angle of attack from EVM,  $\alpha_{\infty}$  the undisturbed one,  $C_L$  and  $C_D$  are the aerodynamic coefficients of the considered airfoil and  $c$  is the chord length,  $l_{cell}$  the characteristic mesh dimension, so  $c/l_{cell}$  is a non-dimensional value properly chosen to represent the chord im-

pact over the intensity of the forces. To quantify the  $\Delta\alpha$  correction a huge test campaign was made considering a large variation for all the comparing parameters: different test cycles were made to study the influence of varying  $C_L$  (within the cycle), while  $C_D$  and  $c/l_{cell}$  were fixed for the considered cycle itself. Since the flow is stationary, the validation of the EVM just requests to compare the detected  $\alpha_{EVM}$  with the undisturbed angle  $\alpha_\infty$ , that is known a priori. So here are presented the different tests made:

- $C_L$  varying in the range from 0 to 2, step 0.2, with  $C_D$  fixed once equal to 0, once equal to 0.25, once equal to 0.5;
- fixed  $C_L = 1, C_D = 0$ , a test cycle was made varying the profile chord from 0.1 to 1, step 0.1. These tests give an idea of the influence of the parameter  $c/l_{cell}$ , even if it is quite obvious the linear influence of this parameter, because the forces depend linearly by  $c$ , when  $C_L, C_D$  and  $\mathbf{U}$  are fixed.

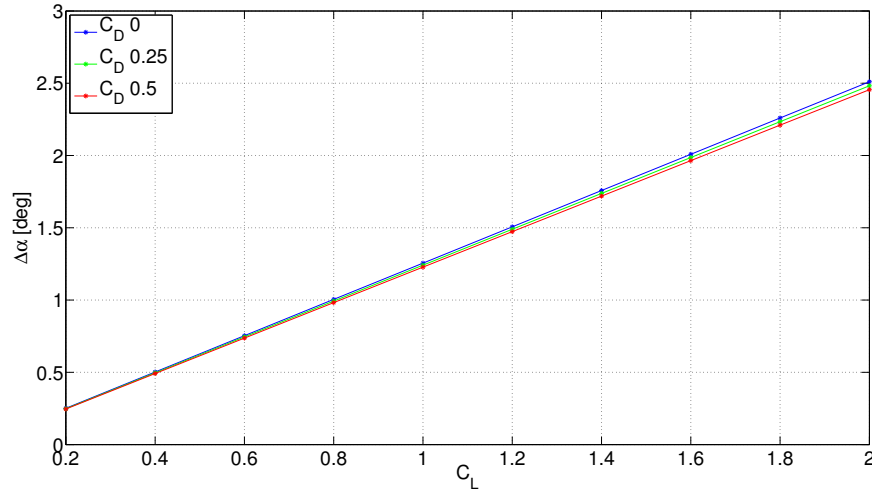


FIGURE 4.20: Influence of  $C_L$  and  $C_D$  on  $\Delta\alpha$  value.

For all tests  $l_{cell}$  was equal to 1 m and the initial condition for  $\mathbf{U}$  is horizontally directed, magnitude of 10 m/s. Relating to fig. 4.20 the following evidences are detected and used to definitively estimate the EVM correction:

- $\Delta\alpha(C_L)$  is a linear function;

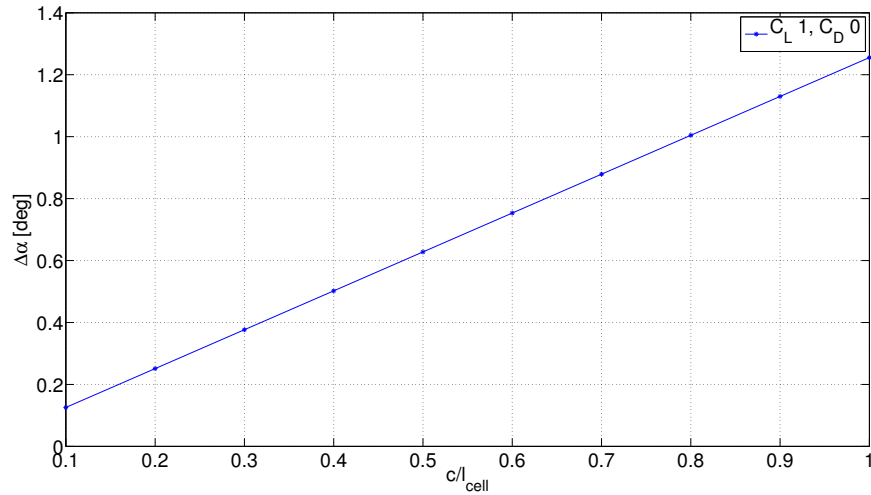
- the correction depends primarily by  $C_L$ , but the influence of  $C_D$  is clearly visible, as an alteration of the slope of  $\Delta\alpha(C_L)$  line;
- the non-dimensional ratio  $c/l_{cell}$  impacts linearly on the  $\Delta\alpha$  value, as shown by fig. 4.21a.

Hence this is the proposed correction:

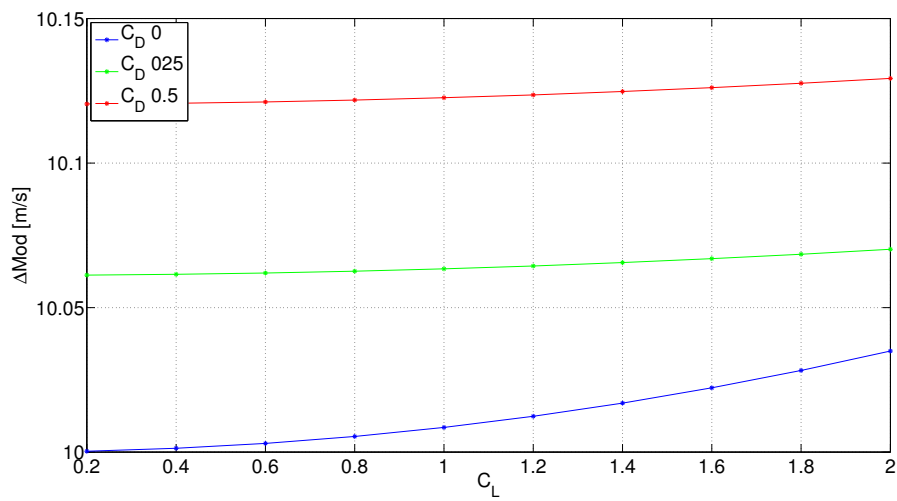
$$\Delta\alpha = \frac{c}{l_{cell}} \cdot (1.2553 - 0.0552C_D)C_L \quad (4.17)$$

An important observation is that any correction is needed for the absolute value of  $\mathbf{U}$ , since the presence of profile induces only a deflection on the incoming flow. Studies have been made also in this direction and confirmed the hypothesis, as can be visible in fig. 4.21b. Of course, must be remind that  $\Delta\alpha$  correction previously presented is inextricably associate to the previous chosen position for the EVM sampling line.





(A) Influence of the parameter  $c/l_{cell}$  on  $\Delta\alpha$  value.



(B) Influence of  $C_L$  and  $C_D$  on the absolute value of  $\mathbf{U}$ . Its scarcity makes it negligible.

FIGURE 4.21: Minor influences of EVM: influence of the parameter  $c/l_{cell}$  on  $\Delta\alpha$  (a) and influence of  $C_L$  and  $C_D$  on the absolute value of  $\mathbf{U}$  (b).

### Validation and performance of the EVM

The fourth and final step of the tuning of the EVM is a first validation of the introduced model. A new test campaign is set-up, considering a stationary case, and as initial condition the incoming flow is characterized by a velocity magnitude of 10 m/s, but different inclinations of the angle of attack are taken into account. The tests are made up to show the robustness of the model, showing the capacity of the EVM to work regardless the way how aerodynamic forces are inserted in CFD numerical equations. In section 4.3.1, the regularization kernel width is found considering known aerodynamic forces; now, this section presents the relationship between the velocity evaluation and the force application models. For different angles of attack, even considering the stall condition, a set of tests has been performed to quantify the benefits given by the EVM adoption. A uniform flow, with a magnitude of 10 m/s and different angles have been tested for the reproduction of the NACA0012 profile via AF. For these simulations both the EVM and the LM have been employed, adopting different kernel widths, as reported in fig. 4.22, 4.23, 4.24.

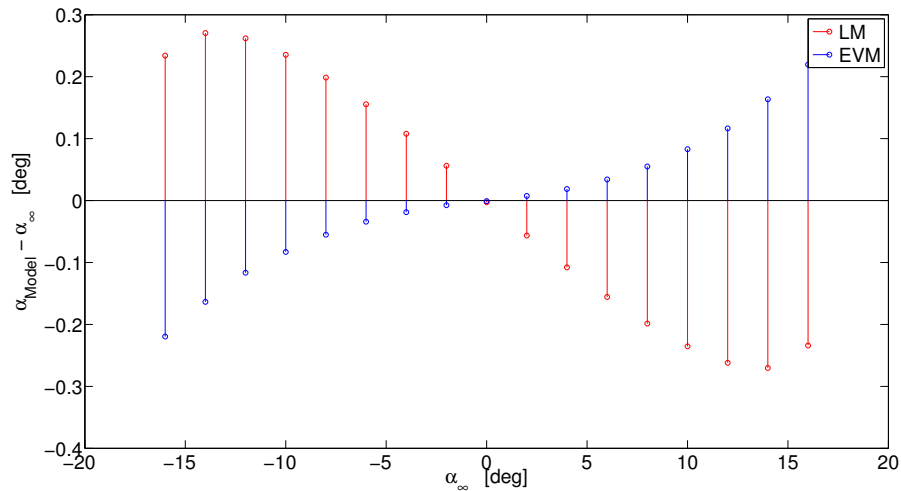


FIGURE 4.22: *Estimation of the undisturbed AOA: the EVM is compared to the LM with a regularization kernel width  $\epsilon = \sqrt{2}l_{\text{cell}}$ .*

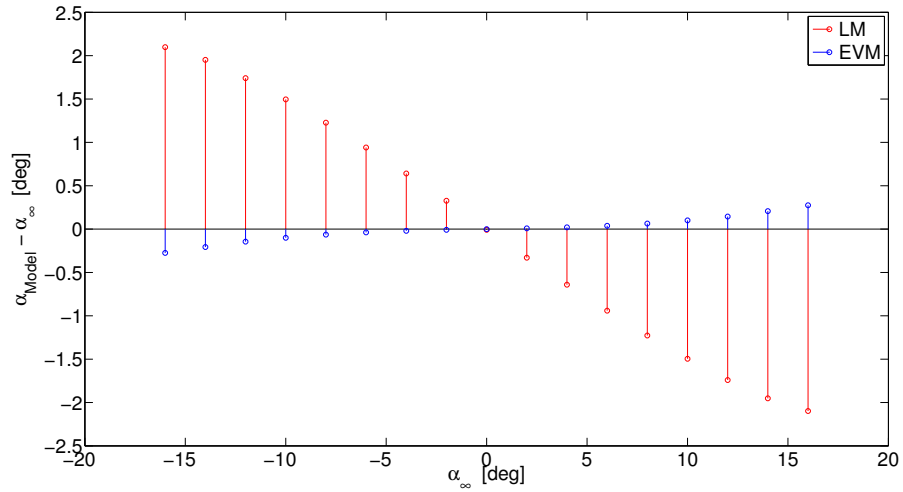


FIGURE 4.23: Estimation of the undisturbed AOA: the EVM is compared to the LM with a regularization kernel width  $\epsilon = l_{\text{cell}}$ .

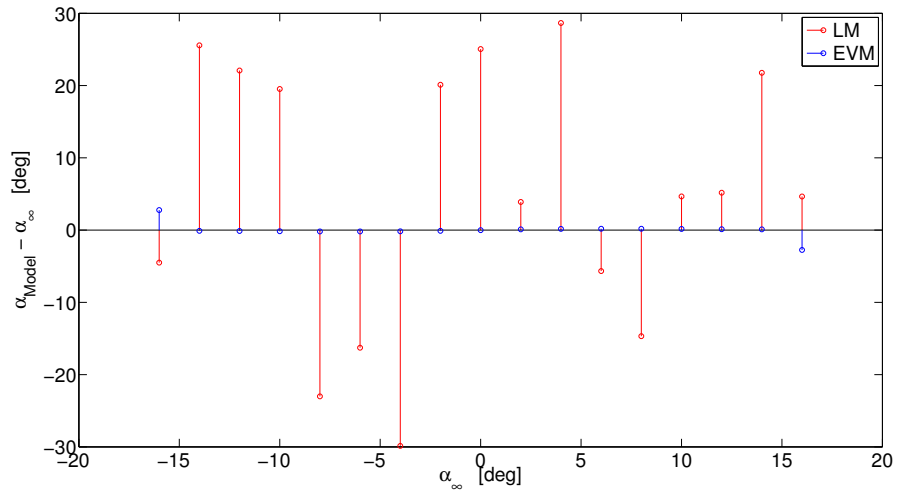


FIGURE 4.24: Estimation of the undisturbed AOA: the EVM is compared to the LM without regularization kernel.

The regularization kernel width  $\epsilon$  of fig. 4.22 corresponds to the value used by Troldborg [17], reported in eqn. (4.9), while  $\epsilon$  of fig. 4.23 is the optimal value found in this work. The EVM allows a specific set-up for each choice of  $\epsilon$  and thus it shows good performances for every value. On the other hand, the accuracy of LM is good for  $\epsilon = \sqrt{2}l_{cell}$ , decreasing rapidly for  $\epsilon = l_{cell}$ , until the total break-down of the model when any regularization kernel is applied. As stated in the EVM introduction, one possible reason for the LM loss of accuracy can be the behavior of the fluid in the area close to the force application point. In fig. 4.25 fluid angle is plotted on an horizontal line containing the force application point. Local sampling of the velocity field means looking at a region characterized by strong gradient in fluid direction. Theoretically, the lift induced velocity should be null exactly at the force application center, but this results to not be completely true in the CFD solution. Moreover, due to the gradient intensity, the angular estimation error can eventually be significant. The EVM, however, samples upstream the force application point in an area distinguished by a smoother angle variation, guaranteeing higher numerical robustness and allowing smaller regularization kernel widths: in our case, passing from the literature value of  $\epsilon = \sqrt{2}l_{cell}$  to  $\epsilon = l_{cell}$ .

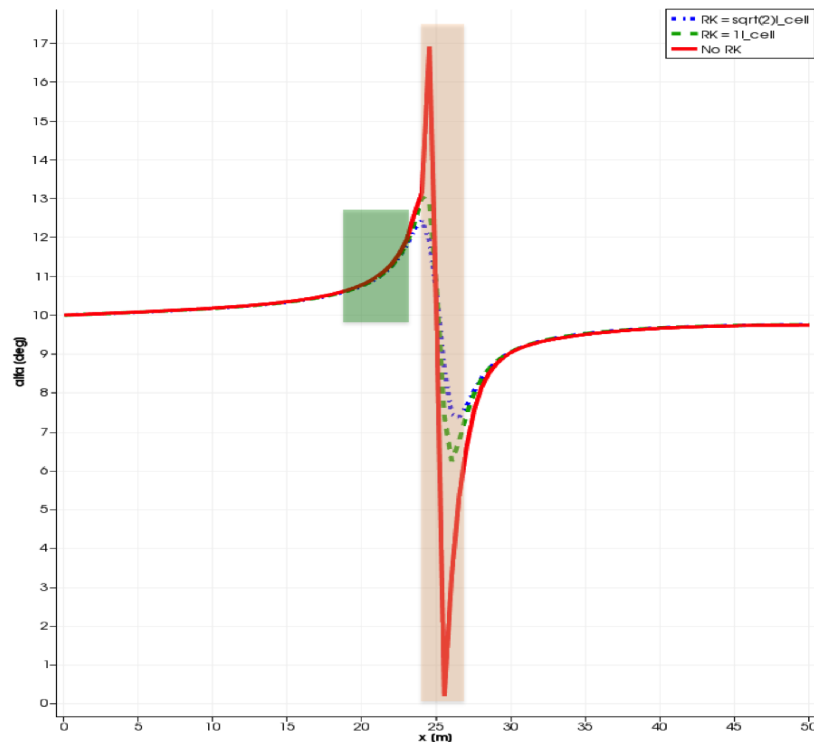
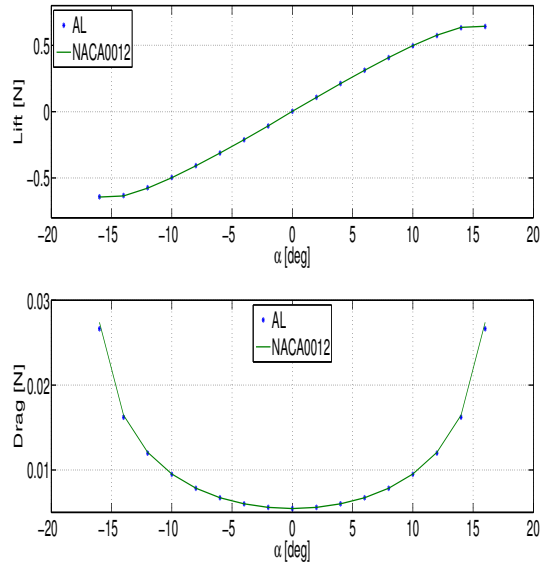
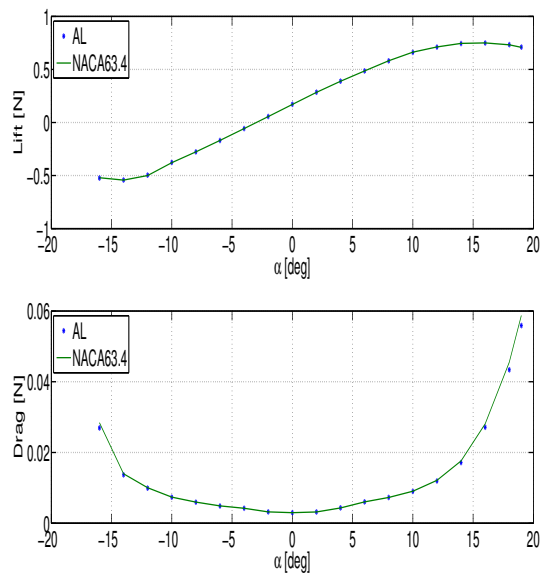


FIGURE 4.25: *Fluid angle sampled on an horizontal line crossing the domain. The high gradient region is due to the profile presence. The light red rectangle identifies the LM sampling region, while the green the EVM one.*

The EVM effectiveness is proven also by the good agreements between forces generated by different NACA profiles and the ones calculated by AF. Fig. 4.26a and fig. 4.26b show that the model works correctly with two distinct type of airfoil, known polar curves simply, because the  $\Delta\alpha$  correction is function of non-dimensional coefficients. NACA0012 is the chosen profile for all the simulations made for the EVM construction and validation and it is a symmetric wing profile. NACA63.4, on the other side, is not symmetric. The polar curves have been supplied by [41].



(A) *AF + EVM reproduction of forces delivered by NACA0012 wing profile.*



(B) *AF + EVM reproduction of forces delivered by NACA63.4 wing profile.*

FIGURE 4.26: *AF + EVM reproduction of forces delivered by different wing profiles.*

## 4.6 Non-stationary test case

Since turbine are normally working in non-stationary condition the EVM formulation has to be tested also for not steady inflow case. The idea is to estimate the amplitude and the frequency representative of the normal time-dependent flow history seen by the blade during its revolution in the atmospheric boundary layer (ABL).

### 4.6.1 Wind time history simulation

ABL statistical properties are well studied and reported in literature and international standardization documents like Eurocode [42]. In particular Eurocode describes the wind as an aleatory variable and tabulates its statistical descriptors, like mean wind speed or standard deviation, function of the height from ground,  $z$ . For stream-wise,  $u$ , lateral,  $v$  and vertical component,  $w$  the mean value,  $U, V, W$  respectively, is prescribed as:

$$U(z) = \overline{u(z, t)} = U_{bas} k_r \log\left(\frac{z}{z_0}\right) \quad (4.18a)$$

$$V(z) = \overline{v(z, t)} = 0 \quad (4.18b)$$

$$W(z) = \overline{w(z, t)} = 0 \quad (4.18c)$$

$$k_r = 0.19 \left(\frac{z_0}{0.05}\right)^{0.07} \quad (4.18d)$$

where  $U_{bas}$  depends on the wind climate in the analyzed area while  $z_0$  is function of the terrain orography as reported in fig. 4.27. The aleatory part of ABL wind is described with the turbulence intensity as:

$$I_{u,v,w}(z) = \frac{\sigma_{u,v,w}(z)}{U(z)} \quad (4.19)$$

Terrain category		$z_0$ m	$z_{min}$ m
0	Sea or coastal area exposed to the open sea	0,003	1
I	Lakes or flat and horizontal area with negligible vegetation and without obstacles	0,01	1
II	Area with low vegetation such as grass and isolated obstacles (trees, buildings) with separations of at least 20 obstacle heights	0,05	2
III	Area with regular cover of vegetation or buildings or with isolated obstacles with separations of maximum 20 obstacle heights (such as villages, suburban terrain, permanent forest)	0,3	5
IV	Area in which at least 15 % of the surface is covered with buildings and their average height exceeds 15 m	1,0	10
NOTE: The terrain categories are illustrated in A.1.			

FIGURE 4.27: Eurocode tabulates  $z_0$  function of terrain orography.

that is known from experimental equations in every direction:

$$I_u(z) = \frac{1}{\log\left(\frac{z}{z_0}\right)} \quad (4.20a)$$

$$I_v(z) = 0.75I_u(z) \quad (4.20b)$$

$$I_w(z) = 0.5I_u(z) \quad (4.20c)$$

On the other side wind turbulence is also a spatial phenomenon, thus also time- and length- scales are necessary for a full description. Time scales,  $T_{u,v,w}(z)$ , are defined in every direction as the auto-correlation  $R_{u,v,w}(z, \tau)$ , integral of wind oscillatory part for a point fixed in space:

$$T_{u,v,w}(z) = \int_0^\infty R_{u,v,w}(z, \tau) d\tau \quad (4.21)$$

that represents the mean duration of wind gusts for a fixed observer. According to Taylor's hypothesis gusts are transported by mean wind speed, therefore the length scale is simply defined as:

$$L_{u,v,w}^x(z) = T_{u,v,w}(z) U(z) \quad (4.22)$$

$$L_u^x(z) = 300 \left(\frac{z}{200}\right)^a \quad (4.23)$$

$$L_v^x \cong 0.25L_u^x \quad L_w^x \cong 0.1L_u^x \quad (4.24)$$



Time and length scales are statical instruments for global ABL characteristics, the specific wind time history is however described by its spectrum, for which different experimental equations have been proposed. Eurocode one is:

$$\frac{f S_u(f)}{\sigma_u^2} = \frac{6.8 \left( \frac{f L_u^x(z)}{U(z)} \right)}{\left[ 1 + 10.302 \left( \frac{f L_u^x(z)}{U(z)} \right) \right]^{5/3}} \quad (4.25)$$

where  $S_{u,v,w}(f)$  is the power spectral density (PSD) of wind fluctuation component in the longitudinal direction. From statistical parameters of wind, the PSD is estimated using (4.25), then it is possible to "synthetically" reproduce a wind single point time-history. Statistical dependence between two points in space can be defined with a power cross-spectral density which describes the relationship in terms of modulus and phase of the two points wind speed. Cross-spectral density is defined through the coherence function as:

$$\gamma_u^2 = \frac{S_u(f, P, Q)^2}{S_u(f, P) \cdot S_u(f, Q)} \quad (4.26)$$

where  $\gamma_u^2$  is the coherence value,  $S_u(f, P, Q)$  is the cross spectral density on two points  $P, Q$  fixed in space. The simplest formulation for coherence is an exponential decay:

$$\gamma_u(\delta, f) = \exp \frac{-C_u^{x,y,z} \delta^{x,y,z} f}{U} \quad (4.27)$$

$C_u^{x,y,z}$  are non-dimensional decay constants estimated via experimental test or set as typical literature value [44] (in [45]). From auto and cross power spectral density multi-points coherent wind time-histories can be generated as harmonic superposition [46] (in [45]), with a numerical harmonic generator whose credits go to T. Argentini (Politecnico di Milano, Department of Mechanical Engineering).

#### 4.6.2 Blade wind relative velocity

The velocity seen by revolving blades can be simulated with a radial grid of wind time-history generator [1], with synchronous sampling, at every time step wind speed is sampled at a different radial point according to blade

angular velocity. In fig. 4.28 is reported a simulative case with 90 points

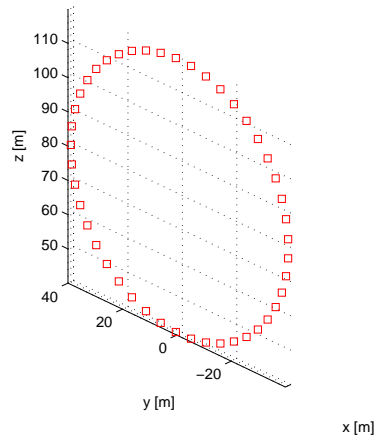


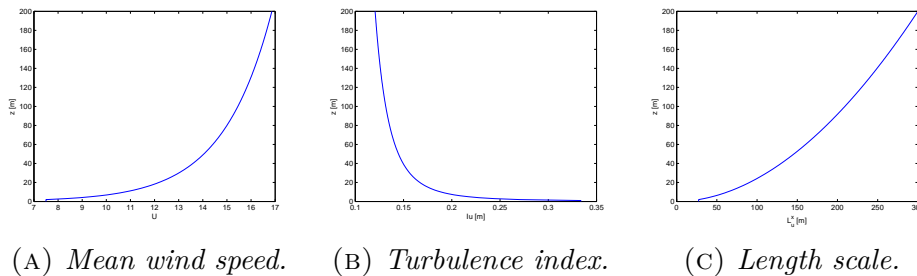
FIGURE 4.28: *Wind simulation points grid: red squares are the radial grid points where wind time-histories are simulated.*

across a circle of 90 m in diameter, representing tip radius of Vestas V90 turbine as described in section 5.1. The turbine nominal angular speed,  $\Omega$ , is 16 rpm (0.2683 Hz - 1.6860 rad/s).

$$d\theta = \frac{\Omega}{N_{grid}} \quad (4.28)$$

$$dt = \frac{d\theta}{\Omega} \quad (4.29)$$

Wind is modeled as a Eurocode cat.II, mean wind speed, turbulence intensity and length scale is calculated as in (4.18a), (4.20a) and (4.22) with  $z_0 = 0.05$  and a reference speed at hub height (80 m) equal to 15 m/s.



(A) *Mean wind speed.*      (B) *Turbulence index.*      (C) *Length scale.*

FIGURE 4.29: *Wind simulation statistical characteristics.*

For these wind statistical parameters different simulations are done at different radial span, the incoming wind speed is studied as seen by a fixed observer to turbine blade. In fig. 4.30 the PSD of incoming wind longitudinal speed is reported. A clear peak is visible at  $1f_{rot}$ : this is due to logarithmic wind profile, where the blade sees a strong variation in wind speed, traveling from the upper to the lowest part of ABL. The other peaks at subsequent multiples of  $f_{rot}$  are instead due to wind turbulence spatial coherence since for a frozen time there exist areas cross by blade where the velocity is relatively high or low depending of gusts shape and characteristics. The  $1f_{rot}$  frequency

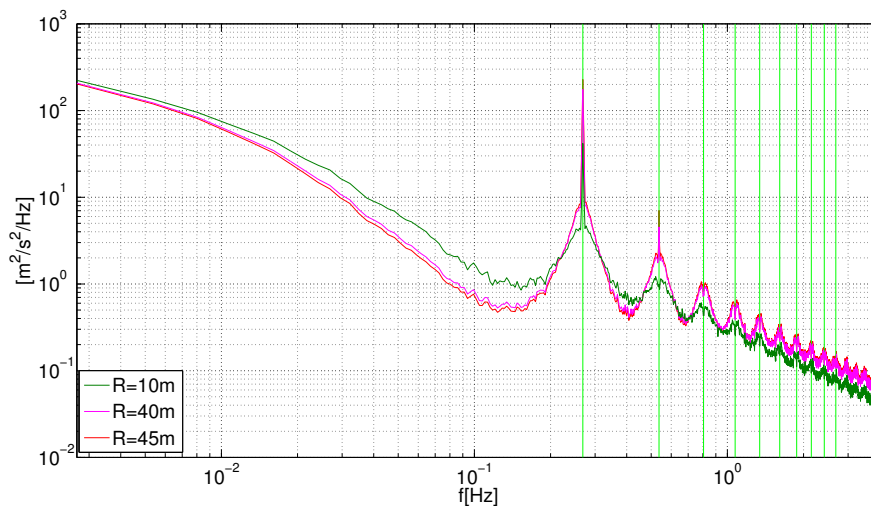


FIGURE 4.30: *PSD of wind seen by blade at different radial span, green line identifies multiples of turbine rotational frequency.*

peak is predominant: this means that the variation in wind speed and angle seen by the rotor in operation in ABL are due mainly to logarithmic mean speed profile. During the revolution in ABL the incoming wind longitudinal component is subject to a periodic oscillation similar to a sine-wave at  $1f_{rot}$ .

### 4.6.3 FRA and AF simulation of airfoil section in oscillating inflow condition

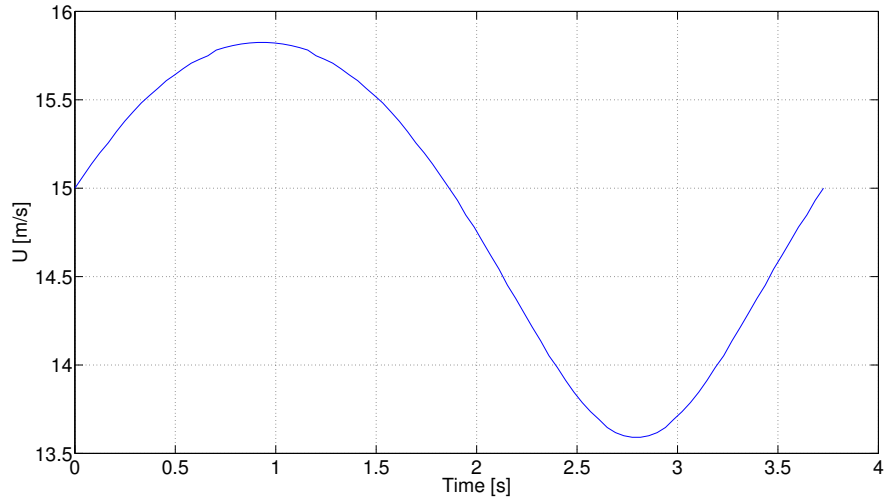
The effect on blade section of this sine-wave can be estimated like in section 4.4.1 on both FRA and AF simulation. First the phenomenon is characterized, different CFD studies [43] have been done on oscillating incoming wind velocity on an airfoil mainly related to the study of pitching blade of helicopters. From the results of this study, the main variables describing the behavior of airfoil under oscillating inflow condition are reported:

$$Re = \frac{cV_\infty}{\nu} \quad (4.30)$$

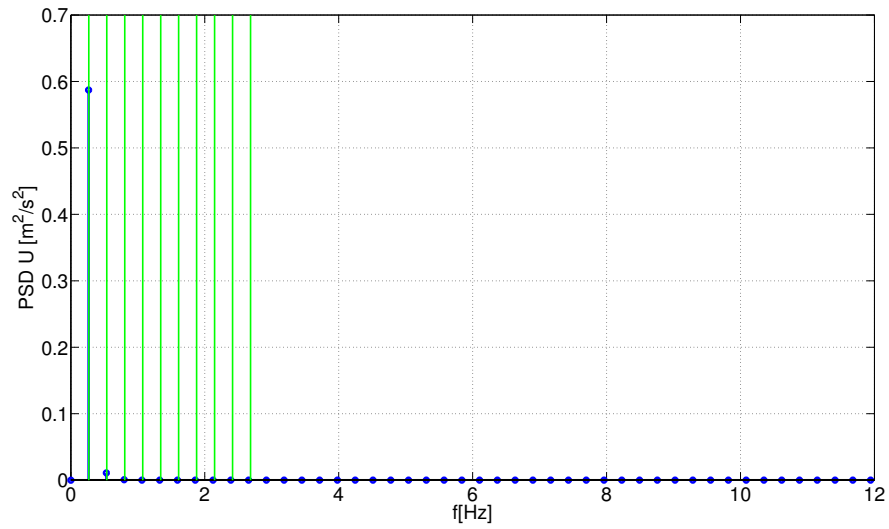
$$\alpha(t) = \bar{\alpha} + \alpha_{amp} \sin(2\pi ft) \quad (4.31)$$

$$k = \frac{\pi fc}{V_\infty} \quad (4.32)$$

where  $Re$  is airfoil Reynolds number,  $\alpha(t)$  is the time variation of angle of attack, in turn described with mean angle  $\bar{\alpha}$  and oscillation amplitude  $\alpha_{amp}$ , and finally the frequency  $f$  and reduced frequency  $k$ . All these four variables are estimated along the entire blade span of the previously cited Vestas V90, for the cat. II logarithmic profile and reported in fig.4.32.

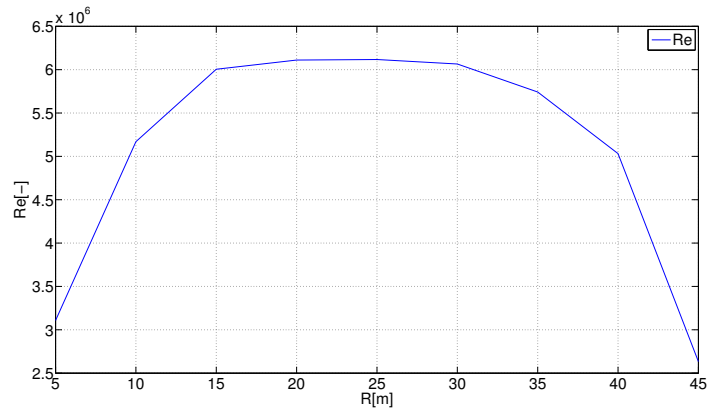


(A) *Blade section wind speed time-history.*

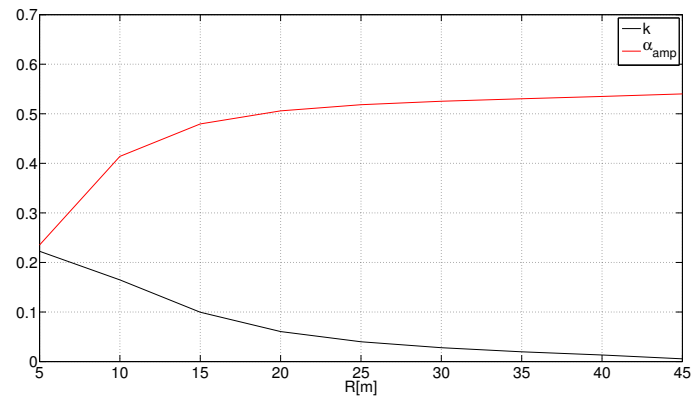


(B) *Blade section wind speed auto-spectra.*

FIGURE 4.31: *Oscillation of blade incoming wind speed due to logarithmic profile for blade point at 40m from hub.*



(A) Reynolds number.



(B) Angle variation amplitude and reduced frequency.

FIGURE 4.32: Reynolds number, oscillation amplitude and reduced frequency of angle of attack are reported along the entire blade span.

One can notice that for almost the entire blade, for a radius greater than 20 m, for both  $Re$  and  $\alpha_{amp}$  a unique describing value can be exerted as representative for the entire blade. For  $k$  the value at radius equal to 20 m is chosen and values are reported in tab. 4.5.

Table 4.5: Blade wind oscillation describing value.

$Re$	$6 \times 10^6$
$\alpha_{amp}$	$0.5^\circ$
$k$	0.05

The boundary conditions of both FRA and AF with EVM simulations are modified, inflow boundary switched from `fixedValue` to `oscillatingValue`, frequency and oscillation amplitude are calculated scaling real values, keeping constant variables of tab. 4.5 and then reported in tab. 4.6.

Table 4.6: FRA and AF oscillating boundaries.

$V_\infty$	10
chord	1m
$k$	0.05
$f$	0.159Hz
$\bar{\alpha}$	$6^\circ$
$\alpha_{amp}$	$0.5^\circ$

Aerodynamic force generated on NACA0012 profile is integrated at every time-step in FRA simulation, similarly force is estimated with EVM in AF simulation, in both three probe lines are placed, one right after the inflow boundary, one in front of airfoil section and the last past the airfoil section as reported in fig.4.33.

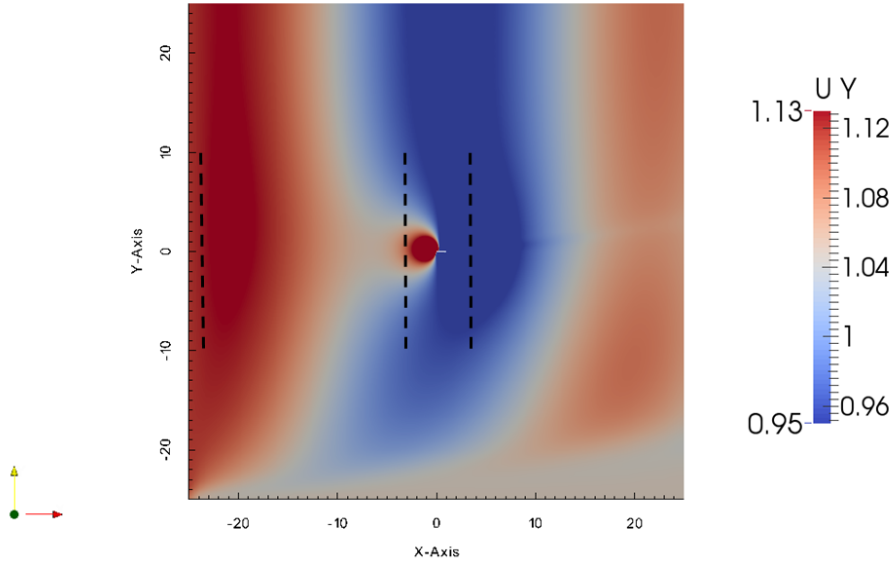


FIGURE 4.33: *The inflow oscillating boundary generates a spatial wave, travelling with mean flow velocity. Black dashes lines are the probes lines.*

Simulations have been carried out with the same set-up as in section 4.4.1 for both FRA and AF, only boundary conditions changed: In FRA simula-

Table 4.7: FRA-AF boundary condition oscillating inlet

boundary	U	p	k	$\omega$
West	oscillatingfixedValue= $\mathbf{V}_\infty(t)$	outletInlet=0	inletOutlet=0	inletOutlet=1
North	inletOutlet= $\mathbf{V}_\infty$	outletInlet=0	inletOutlet=0	inletOutlet=1
South	inletOutlet= $\mathbf{V}_\infty$	outletInlet=0	inletOutlet=0	inletOutlet=1
East	zeroGradient	fixedValue=0	zeroGradient	zeroGradient
Airfoil (only FRA)	fixedValue=0	zeroGradient	kqRWallFunction	omegaWallFunction

tion airfoil boundary conditions are unchanged, the `oscillatingFixedValue` condition allows a time dependent definition of the boundary value reported in (4.33), on West-North-South boundary a inlet-outlet condition is used, this to better handle the oscillating flow as inlet-outlet switches in relation to flow direction from Dirichlet (inflow condition) to Neumann boundary



condition type (outflow condition).

$$\mathbf{V}_\infty(t) = V_\infty \cos(\alpha(t)) \mathbf{x} + V_\infty \sin(\alpha(t)) \mathbf{y} \quad (4.33)$$

$$\alpha(t) = \bar{\alpha} + \alpha_{amp}(t) \quad (4.34)$$

The force integrated in FRA simulation over airfoil boundary and the one estimated by AF simulation are reported functions of time in fig.4.34.

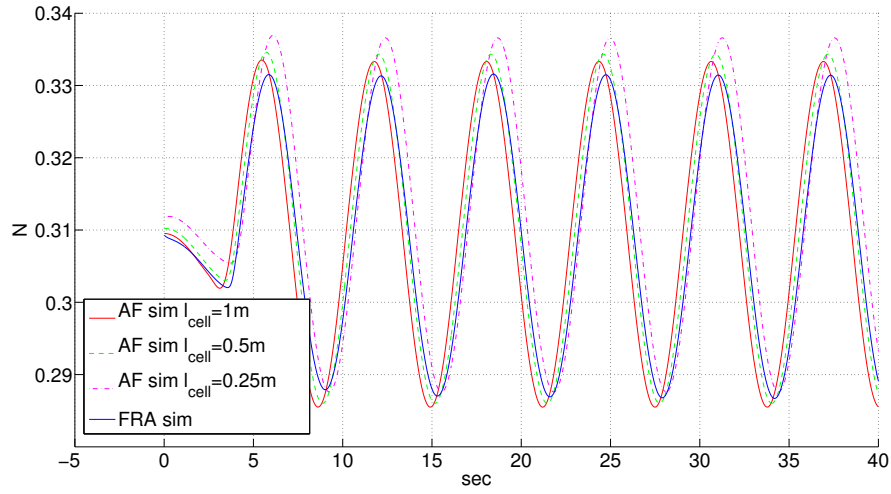
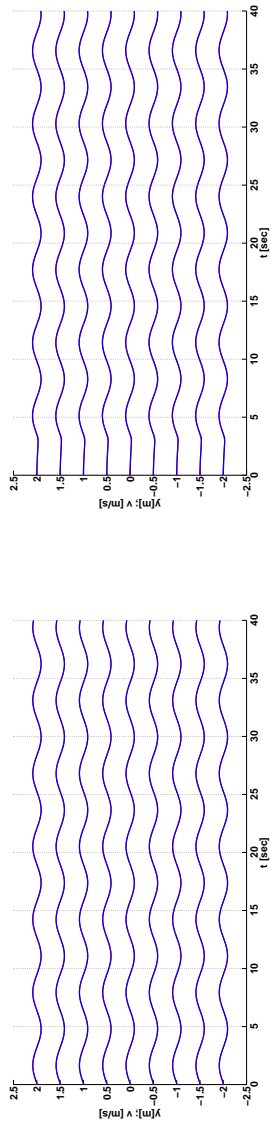


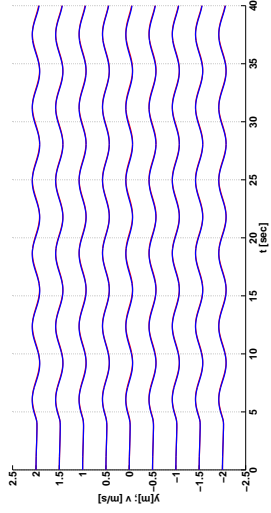
FIGURE 4.34: Force integrated in FRA simulation is compared with AF estimated one for different mesh refinement level.

A small discrepancy is visible and, although it is limited, is higher than in the stationary case. The motivation for this worsening EVM performance is not well understood: it should be remembered that oscillating simulations have an higher level of difficulty then steady state ones and so the possible error sources entering the simulation are numerous. Vertical component of velocity sampled on probes lines is displayed in fig. 4.35, 4.36 and 4.37, for the three AF mesh refinement levels.



(A) Probes on domain entry.

(B) Probes in front of the airfoil position.



(C) Probes behind airfoil position.

FIGURE 4.35: *y*-axis mean data value represents vertical probes position [m], the oscillating part represents the vertical velocity oscillation [m/s].

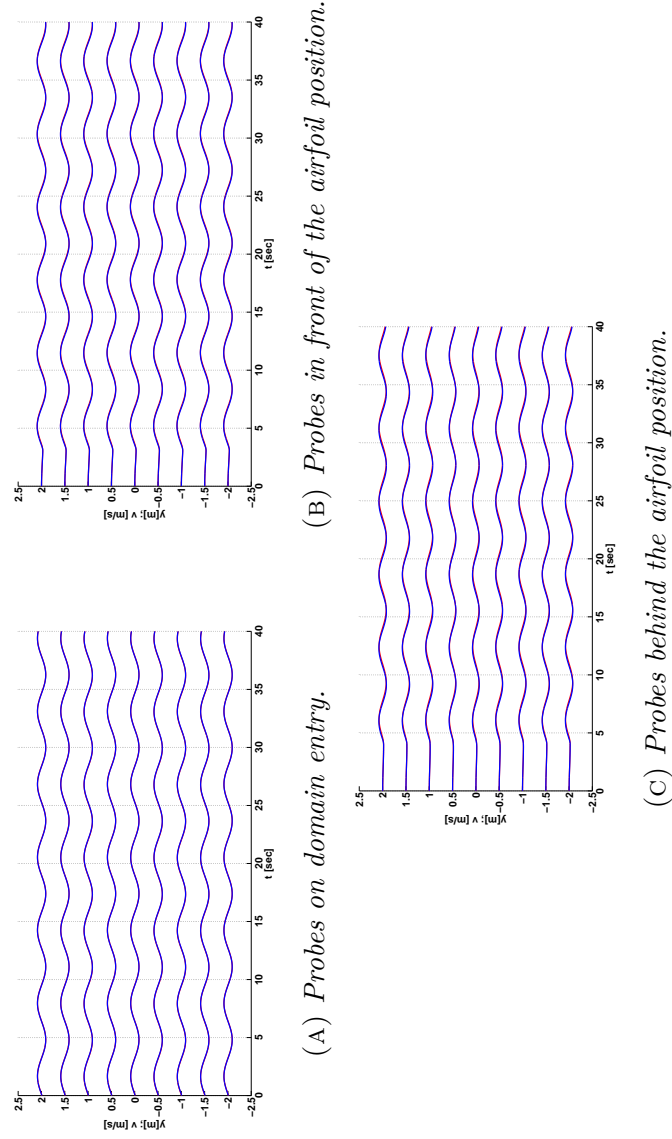
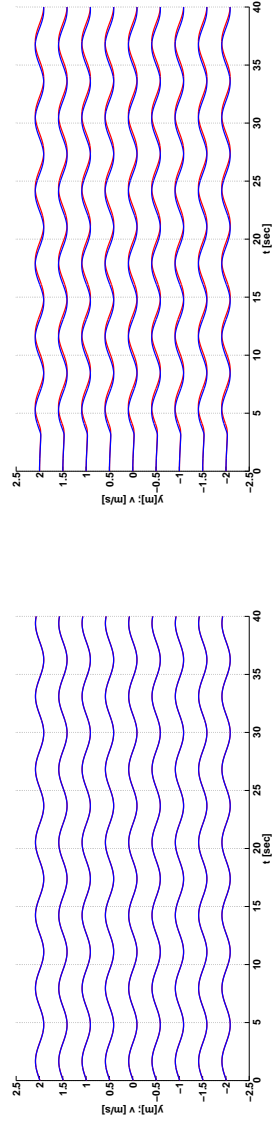
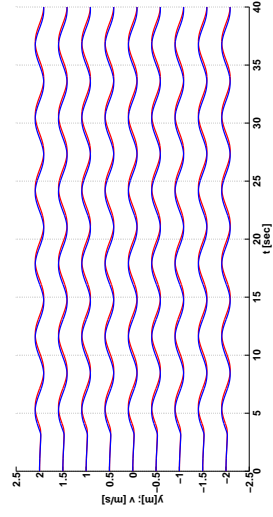


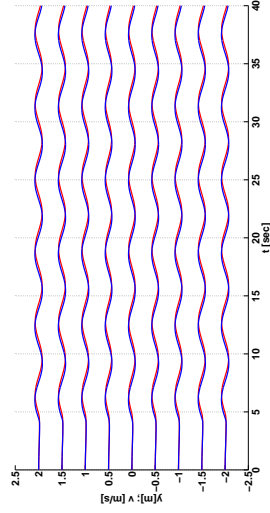
FIGURE 4.36: *y*-axis mean data value represents vertical probes position [m], the oscillating part represents the vertical velocity oscillation [m/s].



(A) Probes on domain entry.



(B) Probes in front of the airfoil position.



(C) Probes behind airfoil position.

FIGURE 4.37: *y*-axis mean data value represents vertical probes position [m], the oscillating part represents the vertical velocity oscillation [m/s].

# Chapter 5

## Wind turbine simulation with Effective Velocity Model

In this chapter the simulation of an horizontal axis wind turbine is presented. Characteristic of this simulation is the actuator line method using the proposed EVM. The performances of the new simulation are compared with the experimental results of a previous test made in the Wind Tunnel facility of the Politecnico di Milano for different TSR values and pitch angles. Also a campaign of sensitivity to the used mesh dimension is carried out and presented. At the end, the implemented theory of the BEM is used as a benchmark for the proposed code results.

### 5.1 Wind turbine of wind tunnel

In 2011 in the Wind Tunnel of the Politecnico di Milano was tested a scaled model of a Vestas V90 3MW wind turbine [47]. This is an horizontal axis, 3-bladed wind turbine with a rotor diameter of 2 m, visible in fig. 5.1. The model was conceived for conducting experimental investigations on the aero-servo-elasticity of wind turbines in the controlled environment of a wind tunnel, as for example for studying the machine response in different operating conditions, the implementation of advanced pitch-torque control laws, the effects of loads induced by wake impingement caused by upstream wind turbines. Furthermore, and this is the reason why this study is very

important to our work, measures conducted on the model can be used for the validation of CFD and aero-servo-elastic codes.

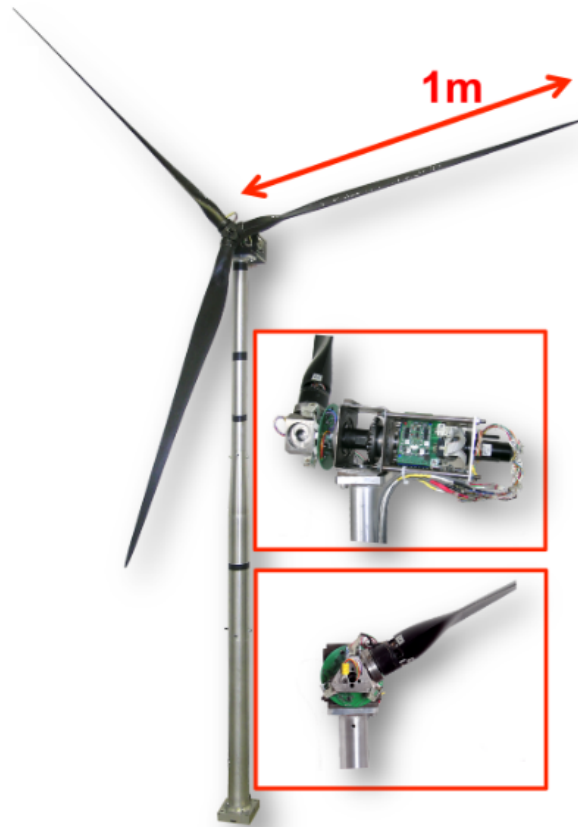


FIGURE 5.1: *Scaled model of Vestas V90 3 MW wind turbine.*

The resulting rated power of the scaled wind turbine is 193.8 W at a rated rotor speed of 367 rpm. The average Reynolds number, which on the V90 is in the range  $4 \div 5 \cdot 10^6$ , on the scaled model is only in the range  $5 \div 6 \cdot 10^4$ . To account for such large differences, the blade was designed using two special low-Reynolds airfoils. The former airfoil was used in the inboard section for  $r/R$  in the range  $0.137 \div 0.423$ , while the latter in the outboard one for  $r/R 0.654 \div 1$ . Not to alter the aerodynamic characteristics of the airfoils, interpolations of the cross sectional shapes were limited to a relatively small transition region between the inboard and outboard sections, i.e. for

$r/R0.423 \div 0.654$  , and at the root region to smoothly deform the inboard airfoil into the blade root cylinder. The blade span-wise chord distribution was geometrically scaled from the original one; on the other hand, to account for the change of airfoils between full scale and scaled blades, the blade twist was modified to yield an optimal span-wise distribution of the axial induction factor.

## 5.2 OpenFOAM solver

Starting from the good matching resulting from the comparisons between the fully-resolved airfoil profile and the 2D AF simulation in terms of loads reproduction and wake similarity, showed in chapter 4, the idea is that is possible to carry over the EVM set-up utilized in the 2D case and use it for the 3D simulation of the wind turbine rotor, in order to have a correct evaluation of the AL line forces for the incoming velocity fields. The employed solver is based on the PISO solver `pisoFoam` yet included in OpenFOAM and then modified following the rules of the AL model and the implementation of the EVM.

The AL technique bases itself on a blade element approach combined with airfoil characteristics. The turbine blades are represented by rotating body forces, and geometrically are described by the position of the two extreme points (run-time updated), in which the first corresponds to the blade-hub connection, while the other one to the blade tip. The discretization of the blades is obtained through the intersections between the ALs and the mesh grid, as visible in fig. 5.2.

The new class `intersectionData`, is created in the solver source folder: its method `findLine`, given two vertices of a line, returns a list filled with the coordinates of intersection points between the mesh and the blade line. Starting from this list, derived lists are the one of the midpoints between one intersection point to one other, the one related to the their distance (so this list represents the segment length of competence of each midpoint), and another one is the list computing the distance from the AL start point. As it could easy deduced, the `intersectionData` class is useful both in identifying the ALs

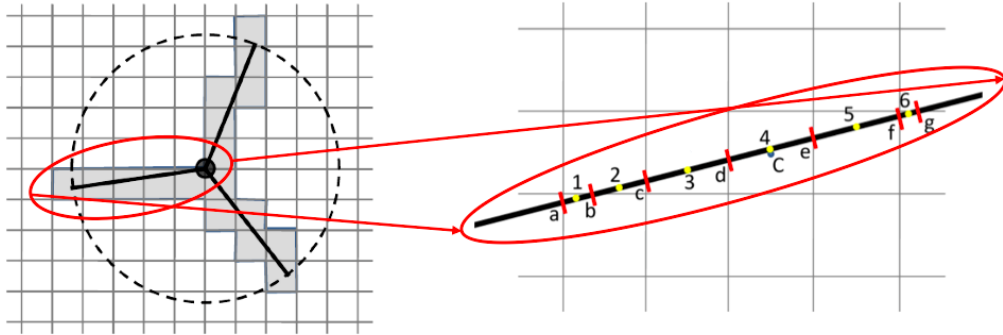


FIGURE 5.2: *Discretization of the blades: yellow points are the AL points representing the blade and insisting on the segments defined by the red dashes.*

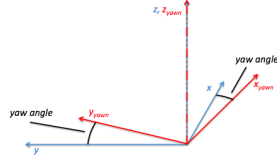
and the EVM sample line. Each point of the AL acts as a single AF point, for which the input data in a dedicated dictionary, called `turbineProperties`, assigning to it the corresponding value of chord length, twist angle and air-foil type. These data are extrapolated by means of interpolation, function of the radial position of the different AL points. The same dictionary contains also some data characterizing the turbine, as the rotational speed, the hub position, the pitch angle. Once these quantities are determined, the solver is responsible for computing the force for each AL point; it must be reminded that the aerodynamic forces lift and drag are defined as prescribed by the BEM theory following the formulation proposed in eqn. (3.18) and (3.19):

Fixing a particular time instant, the force calculation procedure is summarized in the following steps.

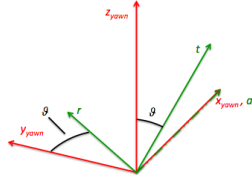
1. The velocity is computed for the single AL point by the solver, applying the proposed EVM. The incoming velocity for an AL point of a given radial position is provided investigating the flow velocity field on the sample line position, averaging the detected values both in term of absolute value and angle and applying the correction (4.17) to estimate the undisturbed flow condition. Then a tensor matrix transforms the velocity value from cartesian to blade coordinates. By this reference system the axial direction is the same of the cartesian system, the radial one is parallel to the blade direction starting from the hub and the



tangential direction is consequence of the right-hand rule. To the force calculation only the tangential and the axial components of velocity are considered.



$$\begin{cases} x_{yawn} \\ y_{yawn} \\ z_{yawn} \end{cases} = \begin{bmatrix} \cos(yaw) & -\sin(yaw) & 0 \\ \sin(yaw) & \cos(yaw) & 0 \\ 0 & 0 & 1 \end{bmatrix} \begin{cases} x \\ y \\ z \end{cases} \quad (5.1)$$



$$\begin{cases} t \\ a \\ r \end{cases} = \begin{bmatrix} 0 & -\sin(\vartheta) & -\cos(\vartheta) \\ 1 & 0 & 0 \\ 0 & -\cos(\vartheta) & \sin(\vartheta) \end{bmatrix} \begin{cases} x_{yawn} \\ y_{yawn} \\ z_{yawn} \end{cases} \quad (5.2)$$

2. The aerodynamic coefficients  $C_L$  and  $C_D$  descend by the EVM application: they are functions of the estimated angle of attack, obtained by the EVM correction. One of the key points of the AL technique is that the forces are not numerically calculated by the CFD simulation of the flow evolution, but they are analytically computed as reported in eqn. (3.18) and (3.19), depending by the aerodynamic coefficients that are stored in different tables for each airfoil type depending by the angle of attack. For the studied case of the Vestas V90 scaled model wind turbine these coefficients have not been extracted from the design profiles, but they are estimated via inverse BEM method as explained by [48]. Fig. 5.3 reports just as example the aerodynamic coefficients of a generic airfoil of the modeled wind turbine.
3. Lift and drag forces are computed according to eqn. (3.18) and (3.19) and they are collected in the volume force vector, expressed in blade coordinates.
4. The regularization kernel is used to smear the force on the cells rep-

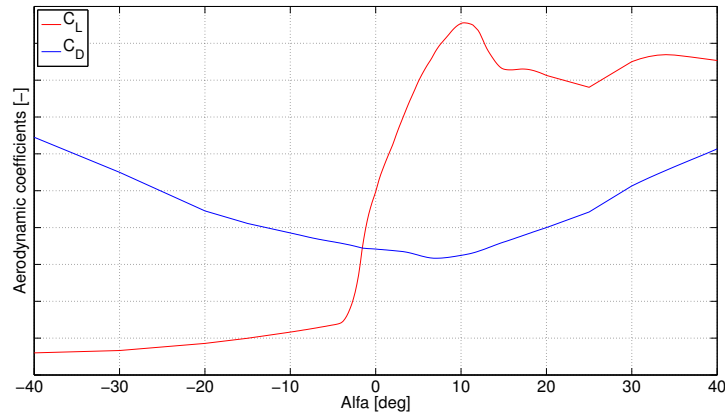


FIGURE 5.3: *Aerodynamic coefficients  $C_L$ ,  $C_D$  of an airfoil of the modeled wind turbine.*

representing the blade and their closest neighbors, following the normal distribution proposed in eqn. (4.7), that provides a cylindrical distribution of the force along the blade, whose width is directly linked to the representative mesh grid dimension adopted for the tested case.

5. At the end, the forces are re-transformed in cartesian coordinates, by means of the antitransformation matrix and the volume force field is updated. Now the modified PISO acts, solving the new equations and providing the new velocity field for the considered time instant.

At the end, it is important also to remark that the developed solver is fully integrated with MPI libraries and it can completely run in parallel processors simulations.

### 5.3 Simulation set-up

In the following the simulation environment, the adopted choices to mesh the domain, to model the turbulence and the turbine, to apply the boundary and initial conditions are explained in detail.

### 5.3.1 Computational domain

In order to directly compare the results provided by the wind tunnel tests on the scaled wind turbine, the control domain reproduces the high speed duct of the Wind Tunnel of the Politecnico di Milano. The duct schematically reproduced in fig. 5.4 measures 4x4 m in section and 20 m in length. The rotor plane is located 5 m downstream the inlet section. The origin of the cartesian system of reference is placed at ground level, on the vertical plane containing the rotor.  $x$  is the axial direction, increasing from inlet to outlet,  $z$  is the vertical direction increasing with the height from the ground and  $y$  is the direction obtained combining  $x$  and  $z$ . The domain is discretized with a structured mesh of cubic cells of 0.1 m as edge dimension. Also a finer mesh, with cells of 0.05 m in edge has been tested and a sensitivity analysis is presented in the following section 5.4.1.

The coarser mesh has the important advantage of requiring very few amount of computational time, however providing good results in terms of performance estimation in terms of thrust, torque, power and wake velocity deficit. On the other side this low resolution does not let to appreciate very well the wake vorticity and its evolution. The studied case adopting the finer mesh confirmed the result computed by the coarse mesh tests adding a more careful reproduction of the wind turbine wake. It is always desirable the usage of mesh as fine as possible, but this target must be always weighted to the available temporal and computational resources.

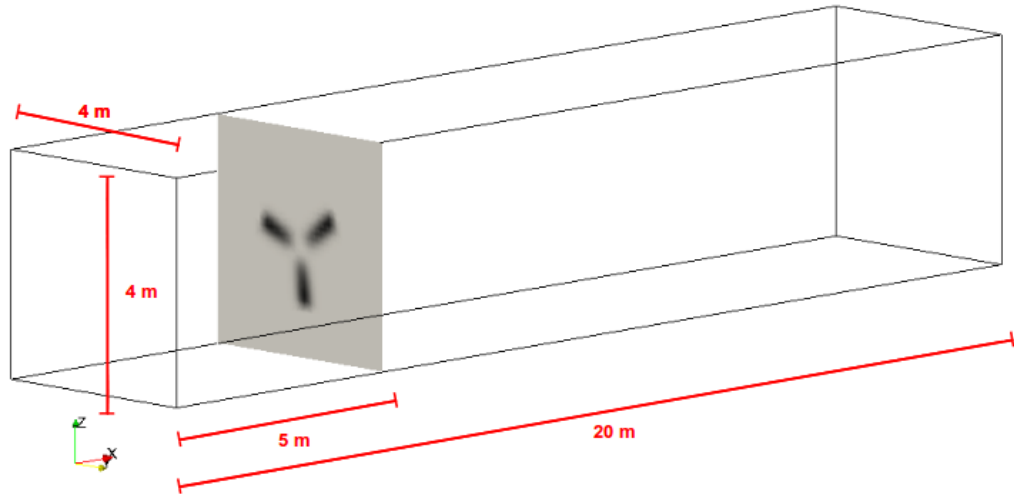


FIGURE 5.4: *The computational domain reproducing the high-speed duct of the Wind Tunnel at the Politecnico di Milano. The rotor plane of the wind turbine is put in evidence.*

### 5.3.2 Turbulence modeling

Usually in CFD-LES, turbulence is created from the boundary layer developed near the walls and by resolving it on a fine mesh. This kind of approach requests small cell sizes and time steps, increasing the computational costs especially under the condition of high Reynolds number. As proposed in [49] to overcome this difficulty, the AL technique does not reproduce the blade boundary layer, and it creates turbulence from the movement of the rotating forces and their interaction with the atmospheric boundary layer investing the turbine without any initialization, as visible in fig. 5.5. To solve the test case, turbulence is modeled following the Smagorinsky model of the LES approach, as explained in chapter 2.

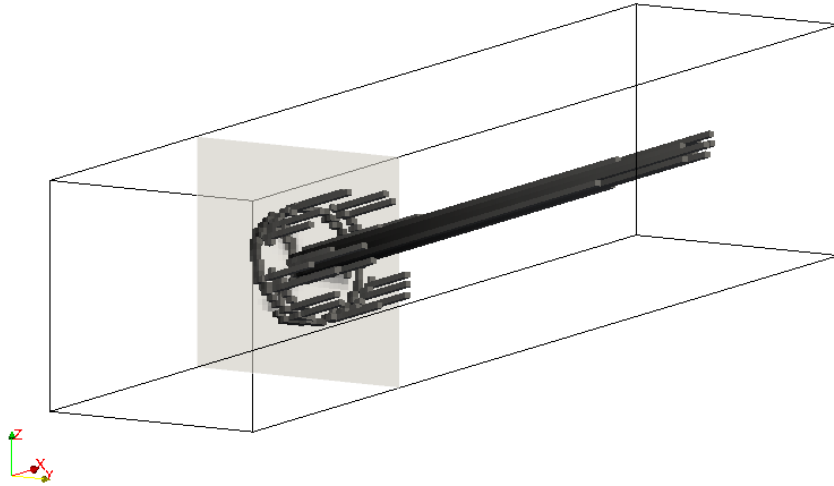


FIGURE 5.5: *Turbulence generates from the blade rotation only (the rotor plane is grey highlighted) and develops in the wind turbine wake.*

### 5.3.3 Turbine modeling

The solver acts calculating the forces delivered by a three different and rotating actuator lines, representing the blades, seen as sequence of AF points. All the data relative to the turbine are collected in a dictionary, including the description of the blade profile for some different values of the radial distance from the hub. For each section of the blade the chord length, the twist angle and the characteristic airfoil are indicated. All the aerodynamic coefficients for the used airfoils are tabulated in several dictionaries called `airfoilProperties`. The modeled turbine has a rotor diameter of 2 m, whose hub is placed at a height 1.9 m from the floor. The high blockage ratio of the tested cases affected the results of the simulations, so in order to strengthen the code validity some more cases have been studied using an enlarged domain and then compared with the results coming from a traditional BEM. This problem is better treated in section 5.6.

### 5.3.4 Boundary and initial conditions

The initial condition consists in a uniform flow entering from the inlet section at a fixed rate; also the rotational speed is constant for all the simulation period and by the way, also the TSR is constant. Different TSR conditions have been tested: according to eqn. (1.3), they are presented in table 5.1. For the ground, the ceiling and lateral sides of the duct is valid the no-slip condition (they are modeled as walls), since the reproduction of the wall boundary layer is not a fundamental issue in this study and would increase significantly the computational cost. The section positioned opposite to the inlet one is considered the outlet, through which the air flows away, as happens in the wind tunnel. At the outlet Neumann boundary condition is imposed. Everywhere an initial condition of pressure equal to the reference one is applied.

Table 5.1: TSR tested values and corresponding rotational and incoming flow velocities

<i>TSR</i>	$\omega$ [rpm]	$V_\infty$ [m/s]
5	35	7
7	42	6
9	42	4.667
11	42	3.818

The simulation is performed for 20 s with a time step of 0.001 s, by the way the Courant number (defined for a cell in eqn. (5.3): it is an indicator that must be lower than 1 to achieve temporal accuracy and numerical stability when running the solver [9]) is always limited during the run.

$$Co = \frac{\delta t |\mathbf{U}|}{\delta x} \quad (5.3)$$

Adopting the coarse mesh, the domain is divided into 320,000 cells and the simulation has been performed across 2 nodes of the Cineca Eurora computer: a total of 32 processors and 12 GB of RAM have been employed. For the finer mesh case, made by 2,560,000 cells 4 nodes of the Cineca Eurora computer were occupied: the total resource request amounts to 64 CPUs and 24 GB of RAM.

The actuator lines lie on a plane, perpendicular to  $x$  axes and placed 5 m downstream the domain inlet wall. The evolution of the flow is calculated in the near wake region only since the domain extends up to 15 m after the turbine.

## 5.4 Turbine performance analysis

Two of the main aims of our thesis work are presented here and in the next section. The validation of the proposed AL model including the EVM, implemented in OpenFOAM following the set-up previous explained, means a correct reconstruction of the loads acting on the wind turbine blades and a good reproduction of the wake. Of course, the sampled data are compared with the wind tunnel experience of [47]. In this section our aim focuses on blade loads and the derived indicators of thrust, torque and delivered power. During the execution of the simulations we collected different performances in order to make us sensible to the turbine behavior and dependance by different simulation parameters set in the input phase of the test. Starting from the force expressed in blade coordinates, the turbine performances are estimated:

1. the turbine thrust is given by the sum of the single contribution of each AL point in terms of axial force:

$$T = \sum_{i=1}^n F_{ax,i,j} \quad (5.4)$$

where  $i$  denotes the index of the  $i$ -th AL point on the blade line and  $j$  represent the number of the blade;

2. the turbine torque is given by the sum of the single contribution of each AL point in terms of tangential force multiplied to the corresponding radial distance from the hub:

$$\tau = \sum_{i=1}^n (F_{t,i,j} r_{i,j}); \quad (5.5)$$

$i$  and  $j$  have the same meaning explained previously

3. the overall power generated by the turbine is:

$$P = \tau \omega. \tag{5.6}$$

Information about thrust, torque and delivered power function of time show the transient period and then the regime is achieved: the performances become stable and the small oscillations are due to the small differences of the area used to compute the forces, from a time instant to one other. As proposed by P. Schito [3], the analysis in the frequency domain shows the correlation between the changes in area and the force variations. Fig. 5.6 reports the power spectral density curve of thrust, torque and blade area signals collected during a simulation lasting 5 s for the  $TSR = 7$  condition. It is clearly appreciable by PSDs graphs that the frequencies responsible for small oscillations of the turbine performances are strictly due to the oscillations of the value of area used for the force calculation. This fact is not a problem to this work: the involved frequencies are in the right side of the spectrum, they are all higher than 9 times the rotational frequency of the simulated turbine.



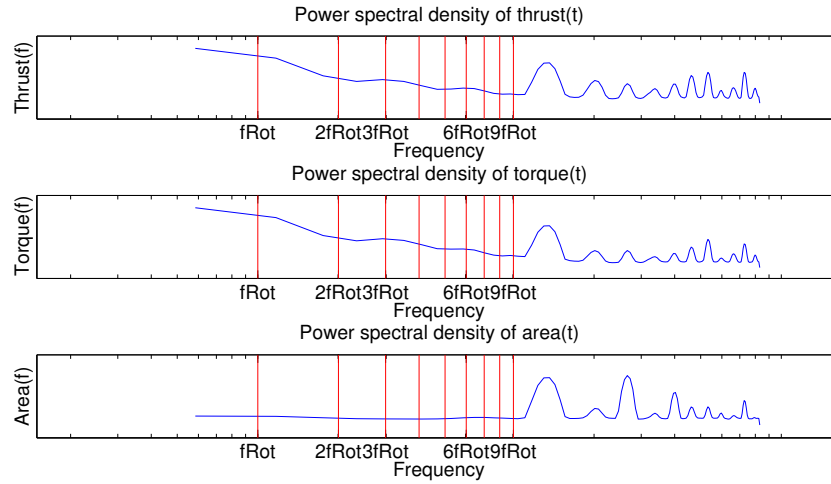


FIGURE 5.6: *Thrust, torque and blade area PSD curves for  $TSR = 7$  case. The red vertical lines indentify the first multiples of the rotational frequency of the wind turbine blades.*

### 5.4.1 Mesh sensitivity robustness

First of all, fixing  $TSR = 7$ , we worked out a comparison between a simulation adopting the coarse mesh made with cubic cells of 0.1 m in edge dimension and the one adopting the cells of 0.05 m. As visible in fig. 5.7 the performances do not suffer the mesh typical dimension exception made for the mentioned oscillations, whose amplitude is however limited. The trends show a transient region lasting more or less 0.8 s and then the regime is reached: turbine performances of thrust, torque and generated power become stable and constant in the time. In order to comply manufacturer's discretion, all the results are presented in non-dimensional form.

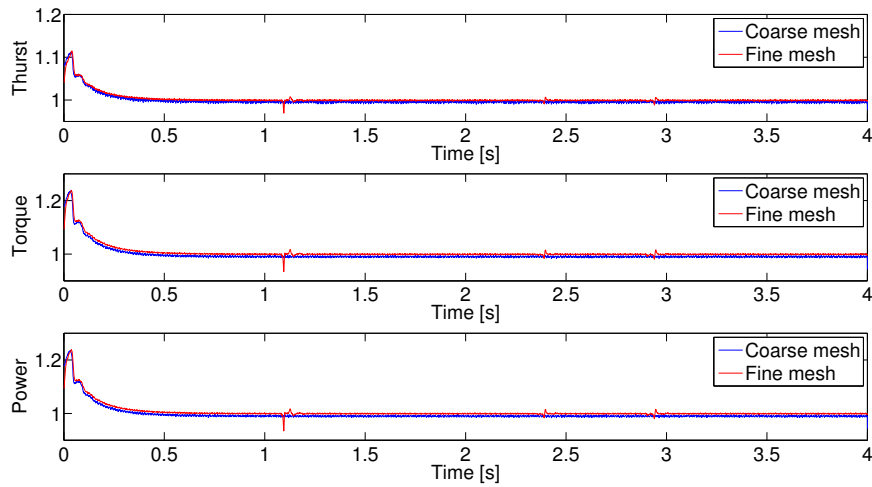


FIGURE 5.7: *Thrust, torque and power measured function of time, for different mesh cases.*

## 5.4.2 Turbine performance analysis under different TSR condition

As proposed in tab. 5.1, our solver has been tested under different TSR conditions, modifying the initial condition of incoming flow and eventually the rotating speed  $\omega$  of the rotor blade. Considering that during these simulation the pitch angle is constant and null, each different TSR condition means that the turbine airfoils work in a condition more or less distanced from the stall. This is particularly evident for the lower values of the TSR tested scale and watching at the first blade sections positioned near the hub, as explained in fig. 1.7, that reports the velocity triangle for a generic section of an AL. Since the contribution of the rotational velocity depends by the radial position, it is clear that near the hub the incoming flow present a higher angle of attack  $\alpha$ , that leads the airfoils to work near the critical stall zone. When entering in the stall region the lift coefficient  $C_L$  shows a sudden decreasing trend that makes the lift force delivered by the observed section very low. Due to the high slope of the lift coefficient respect to the angle, it is reasonable that the most discrepancies between the AL model with EVM

correction and the experimental results happen for TSR values of 5 and 7: this fact could be imputed to some difficulties of the EVM to estimate the angle under high AOA conditions. In particular our model estimates the wind turbine to be just a bit more efficient than the experimental case, so a lower value of thrust and a higher value of torque is detected. Fig. 5.8 shows the regime value of thrust and torque for the tested TSR values and proposes a comparison with the experimental results. The agreement improves as the TSR grows, as consequence of the lower angles of attack distinguish the airfoil working.

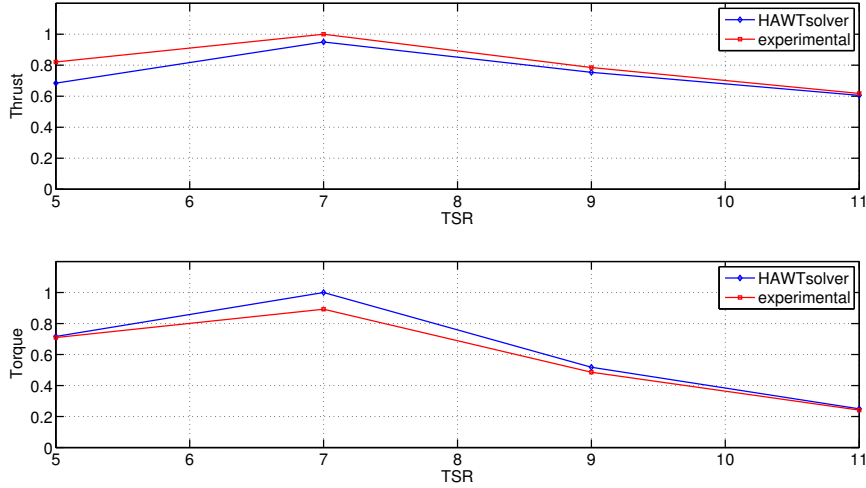


FIGURE 5.8: *Thrust and power for fixed pitch angle (0 deg) generated by the wind turbine as a function of TSR. Comparison between our solver and experimental data.*

Table 5.2 deals with the discrepancies between the simulation and the experimental results in percentage values, computed as:

$$error_{thrust} = \frac{|thrust_{experimental} - thrust_{TSR}|}{thrust_{experimental}} \quad (5.7)$$

$$error_{torque} = \frac{|torque_{experimental} - torque_{TSR}|}{torque_{experimental}} \quad (5.8)$$

Table 5.2: Tested TSR values and corresponding discrepancies between experimental and simulated results in terms of thrust and torque.

<i>TSR</i>	<i>Thrust</i>	<i>Torque</i>
5	-16.6%	-1%
7	-5%	+12.1%
9	-4%	+6.6%
11	-2.1%	+3.3%

### 5.4.3 Turbine performance analysis under different pitch angles

The influence of the pitch angle have been also investigated. A new set of test case involving TSR 7 has been performed varying the pitch angle from a minimum of -5 deg to a maximum of 5 deg. The pitch angle is constant during the simulation and for each case the turbine performances are collected and, when possible, compared with the experimental data.

From figure 5.9 CFD simulations and wind tunnel tests agree quite well, showing a similar trend. Considering the boundary condition of uniform flow at the inlet, it is visible that the achievement of an optimum operating condition requires a pitch angle slightly greater than 0 deg. Even if the solver manifests some difficulties in the exact reproduction of the quasi-flat trend of the torque function of the pitch angle, discrepancies are always limited and decrease increasing the pitch angle. The simulations based on our solver have been tested over a wider range of pitch angle than the experimental tests: focusing on the most negative values of pitch angle, the stall condition is achieved and its negative impact on the performance of the wind turbine is clearly appreciable. As expected, a well-defined decreasing trend characterizes the torque and thus the power generation. Similarly to the previous section about different TSRs, table 5.3 reports the percentage errors between the experimental and the simulation cases, following the definitions provided in equations (5.7) and (5.8).

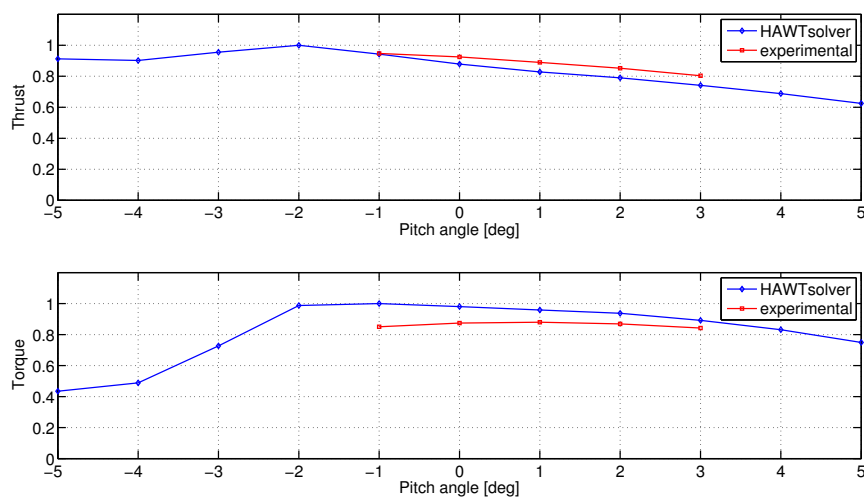


FIGURE 5.9: *Thrust and power for TSR 7 generated by the wind turbine as a function of pitch angle. Comparison between our solver and experimental data.*

Table 5.3: Tested pitch angles and corresponding discrepancies between experimental and simulated results in terms of thrust and torque.

<i>Pitch angle [deg]</i>	<i>Thrust</i>	<i>Torque</i>
-1	-0.4%	+17.6%
0	-5%	+12.1%
1	-6.9%	+8.9%
2	-7.3%	+7.8%
3	-7.7%	+5.8%

## 5.5 Wake analysis

Complementary to section 5.4, this section discusses the analysis of the wind turbine wake. The quality evaluation of the wake is presented in the following subsections where are observed the wake deficit caused by the extraction of energy from the incoming fluid and the vorticity introduced by the blade rotation.

### 5.5.1 Wake deficit

Some measures about the velocity field have been placed downstream the rotor to reconstruct the wake deficit caused by the turbine presence. From fig. 5.10 it is possible to carry out some detailed information about the wake configuration for different non-dimensional distances  $x/D$ , where  $D$  is the rotor diameter. A  $TSR = 8$  is the one used for the comparison. Experimental wake measurements are reported only for half rotor, while LES wake is traced all over the rotor section.

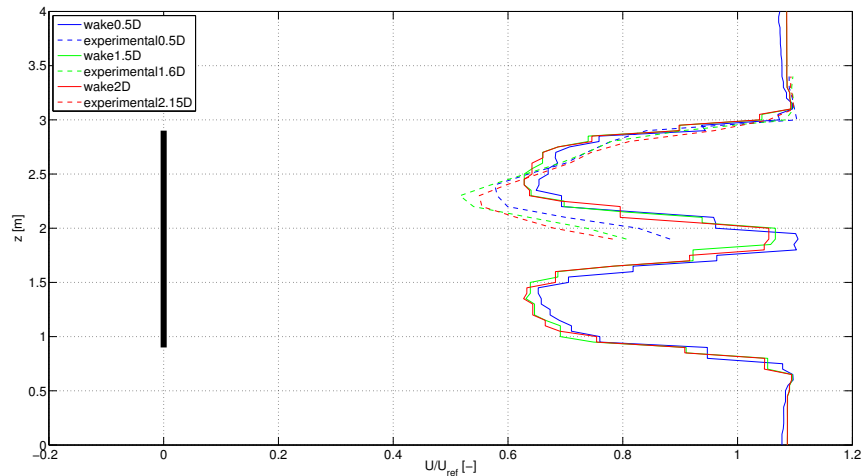


FIGURE 5.10: *Vertical profiles of axial wind velocity in the wake of the wind turbine. Simulation and experimental result are compared probing the velocity field at different distances  $x/D$  downstream of the rotor. The vertical black line on the left represents the turbine rotor section.*

The wake deficit reflects the momentum transferred from the flow to the rotor: it can be stated that they agree quite well even if the distribution of the wake shows some differences in the momentum subtraction. Experimental results indicate that a lower value of wind speed is detected in the region close to the hub than predicted by the CFD simulation, while the trend inverts moving towards the blade tip, where discrepancies decrease. This fact implies a different force distribution on the blade: the wind tunnel test suggests the idea that the root zones are responsible for the most of the force generation, while in the case of CFD simulation the load generation seems to be spread a bit more uniformly. Unfortunately we have not received any measure about the force distribution on the blade in the wind tunnel test experience, but some hypothesis has been elaborated and involve the possibility of add at the code a correction factor to the force value applied in the root region.

At the tip, no blade-tip correction factor is used, differing from [49] and [33], who employ correction factor, justified by *"the tip effect caused by the pressure equalization from the pressure and suction sides at the tip"* [49]. Our code prescribes a regularization kernel to spread the calculated aerodynamic forces that follows a 2D distribution and acts in the plane normal to the blade line direction, so the effect is cylindrical disposition for forces as shown in fig. 5.11. As asserted by Mikkelsen [50], a solver that relies on the actuator line method and solves the full 3D Navier-Stokes equations, loading is applied in an inverse manner respect to traditional BEM approach with the results that the tip correction presents itself from the solution. Using a 3D distribution, the forces are smeared in all directions (of course, also the span-wise one), and as a result, the last point at the tip has less loading than the second point from the tip since each point shares loading with neighbouring points. Moreover, forces are distributed beyond the limit of the actual tip. On a local scale this is inconsistent in the tip region although on a global scale the total amount of applied force is preserved [50]. Using a the 2D approach, even if it is partly unknown the influence of the span-wise discontinuity at the tip (where some wiggles arise and could be avoided by a suitable choice of the kernel width  $\epsilon$ ), the kernel function spreads the force only in the normal blade direction, suggesting the idea that it is not necessary the introduction if the tip-correction factor.

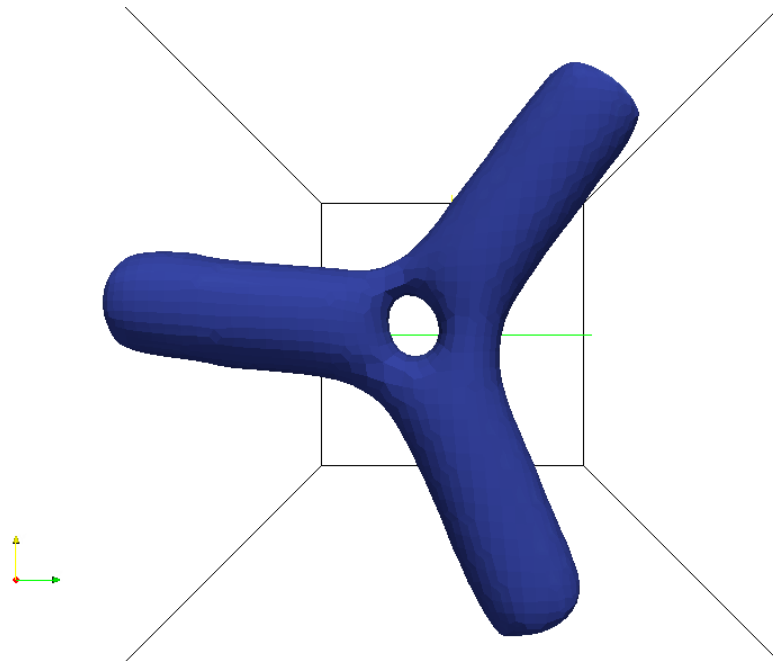


FIGURE 5.11: *The cylindrical volume force distribution is clearly appreciable, loads are not inserted beyond the tip-blade ends as a consequence of the adopted regularization kernel function.*

Some additional considerations about the force distribution along the blade are presented in section 5.6, where is proposed a further validation of the CFD solver code compared to a classical BEM approach.

At this point it is interesting also make two more comparisons on the generated wake. The first one is representative of the evolution of the wake downstream the rotor plane at fixed TSR condition. Subfigures of fig. 5.12 agree in showing that the wake deficit keeps constant in a length of 5 times, while the speed-up of velocity born in the hub region tends to rapidly decrease coming to the original undisturbed value. Looking at the same time at the four subfigures it is evident that increasing the TSR the wake deficit moves towards the blade tip regions, where the tip vortices develop and as a consequence the wake is larger for higher TSR value. On the other side, the second comparison, proposed in fig. 5.13, show the wake generated by different TSR cases and measured at a fixed distance from the rotor plane.



In particular wakes detected at distances equal to 0.5, 1.5, 2 and 5 times the rotor diameter are shown. From these subfigures it is possible to notice that increasing the TSR the wake deficit is higher: this means that if the ratio between the rotational speed of the blades and the undisturbed velocity is higher, the flow will be much more slowed down, the effect is that a low residual of energy in the wind is left.

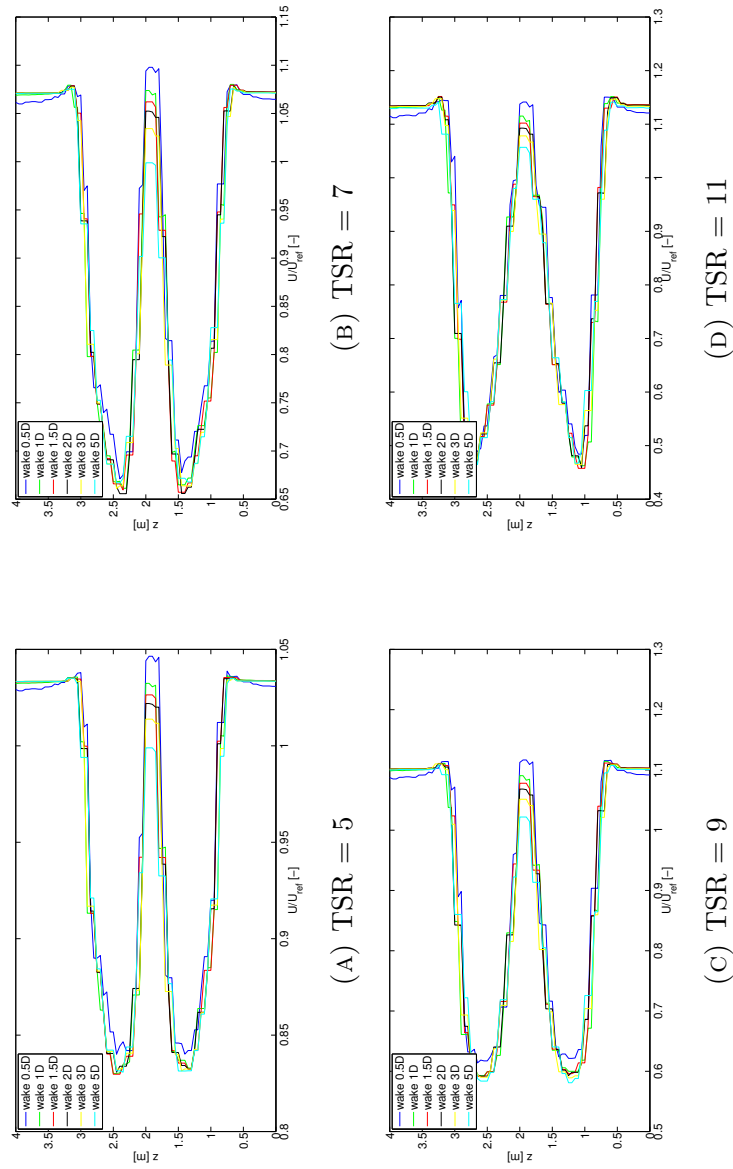


FIGURE 5.12: Evolution of the wake downstream the rotor plane for different TSR conditions. Wakes are detected at different distances from the rotor plane.

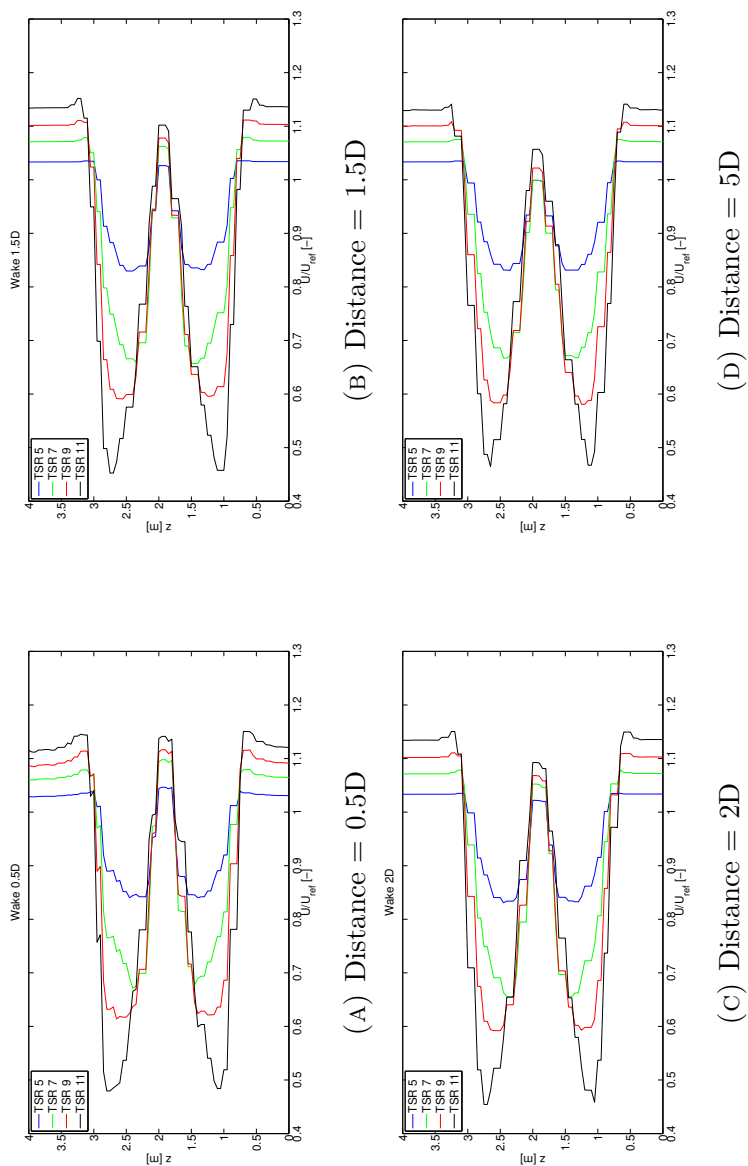


FIGURE 5.13: Wake detected at fixed distance values for different TSR conditions. Distances are measured in rotor diameters starting from the wind turbine rotor plane.

### 5.5.2 Wake vorticity

As stated in 5.3.2 the incoming flow approaching the turbine does not present turbulent structures, so the only perturbations are generated by the presence of the actuator lines representing the wind turbine rotor. The rotating forces generate the vortical structures both at the hub and at the tip of the blades that are subsequently driven downstream by the incoming fluid. Fig. 5.14 identifies the turbulences in the wake, reporting the iso-vorticity surfaces by means of a threshold graphical filter. This kind of visualization is very difficult to be obtained experimentally and it surely helps to make clear the evolution of the flow once encountered the wind turbine blades. Particularly interesting are the dynamics that involve the tip vortices: they are typical vortical structures associated to the finite length of a wing (or in this case, of a blade). At the tip of the wing the flow tends to move from the low-speed high-pressure side (the pressure side of the airfoil) to the high-speed low-pressure side (the suction side of the wing profile) moving externally of the wing; this generates a vortical structure that, for the wind turbine case, traces the path of the blade tips during the turbine operation. At the same time hub vortices develop from the blade root.

Large-eddy simulation makes the wake effects gradually disappear during the flow evolution, since the huge turbulent eddies introduced by the wind turbine rotation progressively loose their energy following the energy cascade principle, explained in [14]. High dissipation causes that the tip vortices are visible only within a distance of approximately 4 diameters behind the rotor plane.

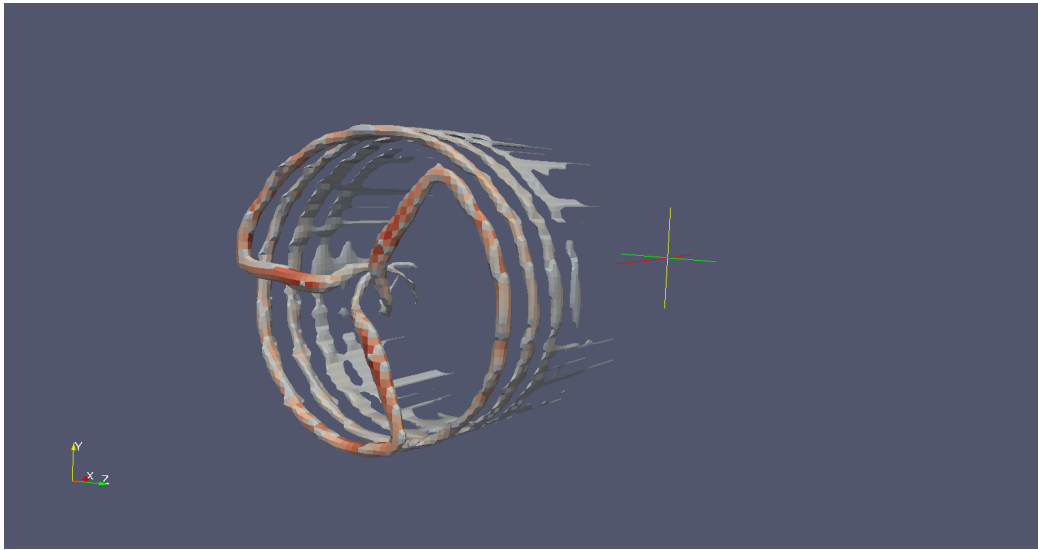


FIGURE 5.14: *Iso-vorticity visualization of the wind turbine wake. The evident wake path is caused by the tip vortices generation, but it is possible to recognize also the hub vortices.*

## 5.6 Comparison between AL solver and BEM approach

In order to reach a better validation of the goodness of the proposed code, some new tests have been performed and compared as a benchmark the results coming from the application of the BEM theory explained in 3.

### 5.6.1 Computational domain

Referring to the dimension of the computational domain reproducing the high speed duct of the wind tunnel at the Politecnico di Milano, it is evident that the high blockage ratio could afflict the simulation: the resulting wake is forced to be narrower since its expansion is limited by the side walls of the domain. In particular considering the normal configuration, the blockage

ratio  $BK$ , defined as:

$$BK = \frac{\text{rotor area}}{\text{domain section}} = \frac{\pi \frac{D^2}{4}}{\text{domain section}} \quad (5.9)$$

is very high, approximately 20 %, being  $D$  equal to 2 m and the duct section 4 x 4 m. In order to extract a more defined comparison between our solver and the BEM, considering that the last one includes the hypothesis of infinite domain, an enlarged computational domain has been designed. A new duct of 8 x 8 m in section is now employed: this leads to a new blockage ratio that is a quarter of the original one, since the section dimensions have been respectively doubled, as visible in fig. 5.15. In this new domain the wake expansion is now free to evolve and to expand, similarly to what happens with the BEM.

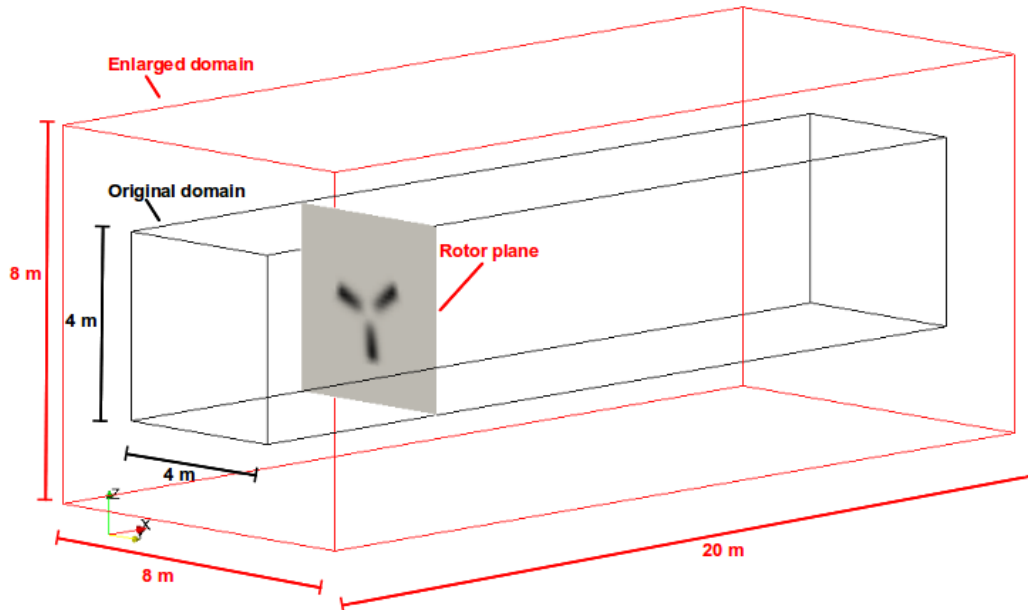


FIGURE 5.15: *Computational domain adopted to compare our solver with BEM vs the original domain reproducing the high speed duct of the Wind Tunnel.*

### 5.6.2 Turbine performance analysis

Here, a more accurate analysis of the blade loads has been worked out, comparing time by time the solver computations in terms of detected and corrected angles of attack for each airfoil section, the corresponding  $C_L$  and  $C_D$  and load for unit length along the blade span, in the axial and in the tangential direction to the blade itself. The tested cases are  $TSR = 7$  and  $TSR = 9$ . Fig. 5.16 and fig 5.17 refer to the first case, and show a good matching between the predictions coming from the BEM approach the application of our solver. In fig. 5.16 the EVM correction of eqn. (4.17) applied to the detected value could be seen. Respect to the BEM this correction, tuned through the studies about the blade section exposed in section 4.5.1, seems to be weaker than needed. The idea is that the correction should be deeper investigated, but some initial faults could be imputed to 3D effects of the blade that are not negligible and afflict the correction and to a coincidence between the rotor plane and the mesh grid. As a consequence of the regularization kernel application, this determines that the forces are applied in a region just a big larger than it could be, both in the upward and in the downward zones. So flow deflection detected by the EVM sampling line is higher. Another element that takes part in the differencing our and the BEM calculations is that for the case of  $TSR = 7$ , some airfoils work very close to the stall. Since the correction is directly linked to the aerodynamic coefficients, it is reasonable that on the quasi-stalled sections of the blade, the estimation of the angle of attack computed by the solver is more difficult to achieve. The intrinsic consequence is that higher is the estimated angle of attack, higher will be the lift coefficient, that primally drives the force generation. Adding also the consideration that the sections where these problems occur are the same where the blade presents its high values of chord, the final conclusion is that the original discrepancies on the angle of attack become amplified differences in the force inserted, as clearly reported by fig. 5.17 for  $r/R$  in the range from 0.3 to 0.5 circa.

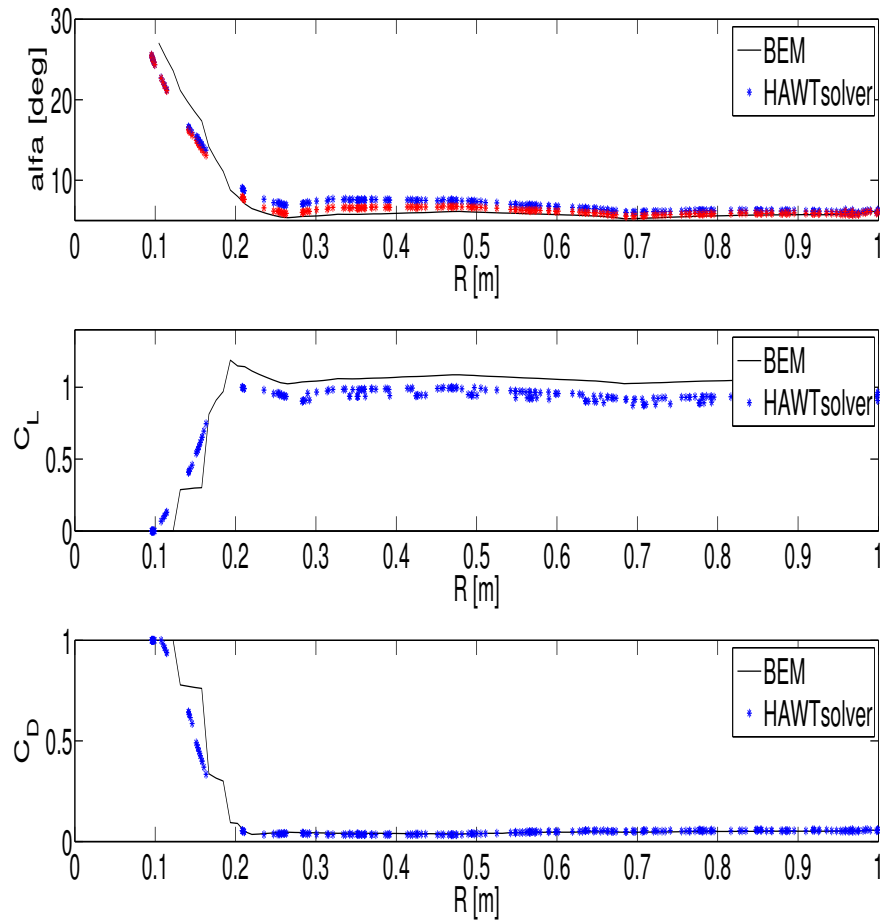


FIGURE 5.16: Detected AOA for  $TSR = 7$  simulation case. In the first plot the red points mark the original detected AOA for every section of the blade, the blue ones refer to the AOA values modified by the EVM correction, while the black line represent the BEM approach. The second and third plots show  $C_L$  and  $C_D$  function of the detected AOA.



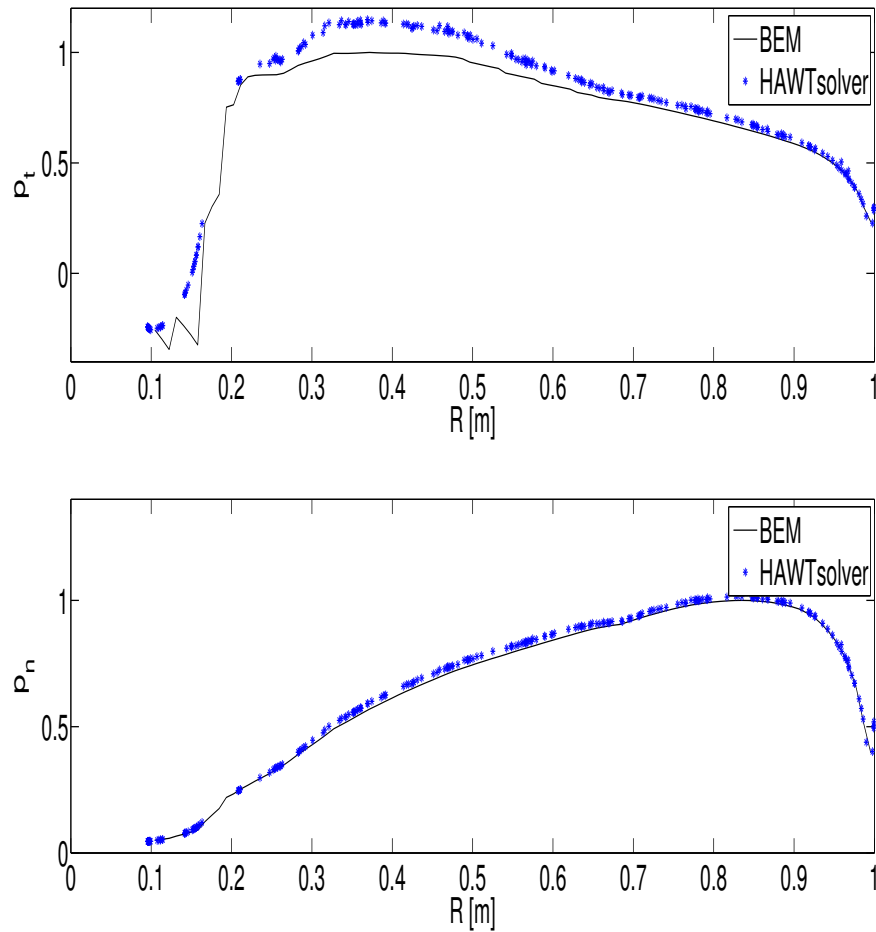


FIGURE 5.17: *Blade loads for  $TSR = 7$  simulation case. The first plot represents the load per unit length vs the blade radial position in the normal direction to the blade. The second plot represents the load per unit length vs the blade radial position in the tangential direction to the blade.*

As said, also  $TSR = 9$  is tested, since it is expected that the stall condition is completely avoided and a better agreement to the benchmark could be reached. Also in this case, as fig. 5.18 reports some differences between the estimated angle of attack employ by the simulation and the one calculated by the BEM. They are sons of the weakness of the EVM correction. Similarly to what happened for  $TSR = 7$ , higher is the AOA, higher will be the blade loading. Fig. 5.19 shows this, but on the other side could be easily concluded that our solver and the BEM approach show for this  $TSR$  value a better agreement than in the other case. Table 5.4 deals with the discrepancies between the simulation and the BEM results in percentage values: even if the errors are quite limited, results depict an overestimation of the wind turbine performances predicted by the BEM.

Table 5.4: Tested  $TSR$  values and corresponding discrepancies between BEM and simulated results in terms of thrust and torque.

<i>TSR</i>	<i>Thrust</i>	<i>Torque</i>
7	+3.1%	+7.9%
9	+4.6%	+15.2%

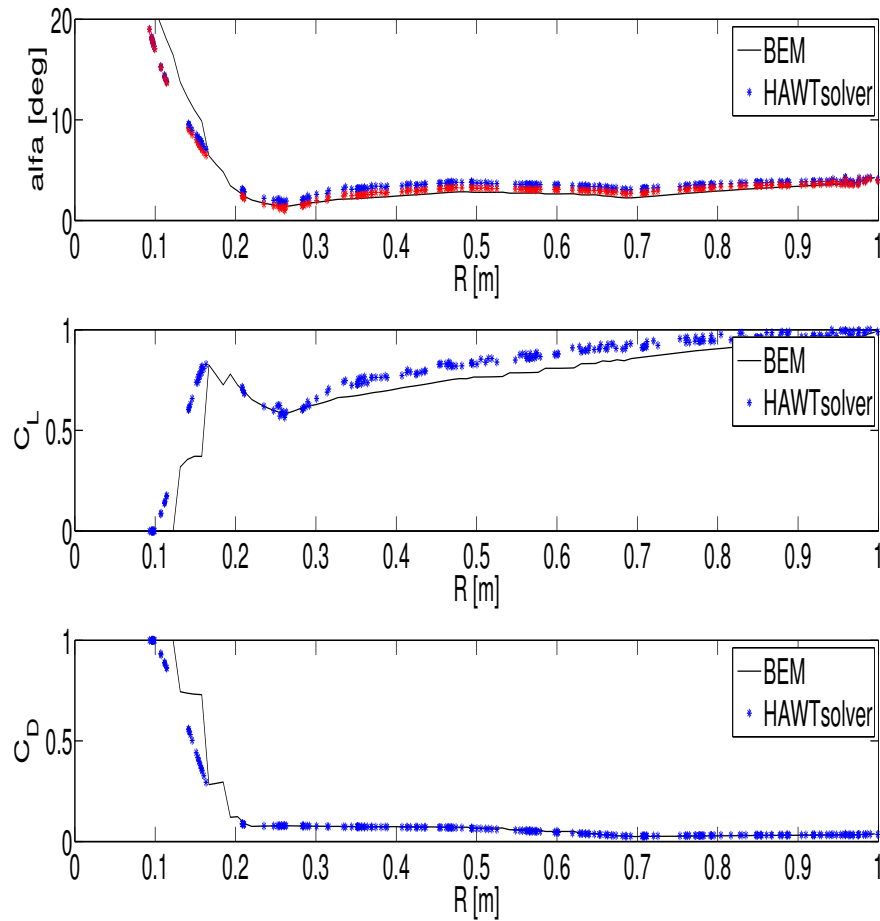


FIGURE 5.18: Detected AOA for  $TSR = 9$  simulation case. In the first plot the red points mark the original detected AOA for every section of the blade, the blue ones refer to the AOA values modified by the EVM correction, while the black line represent the BEM approach. The second and third plots show  $C_L$  and  $C_D$  function of the detected AOA.

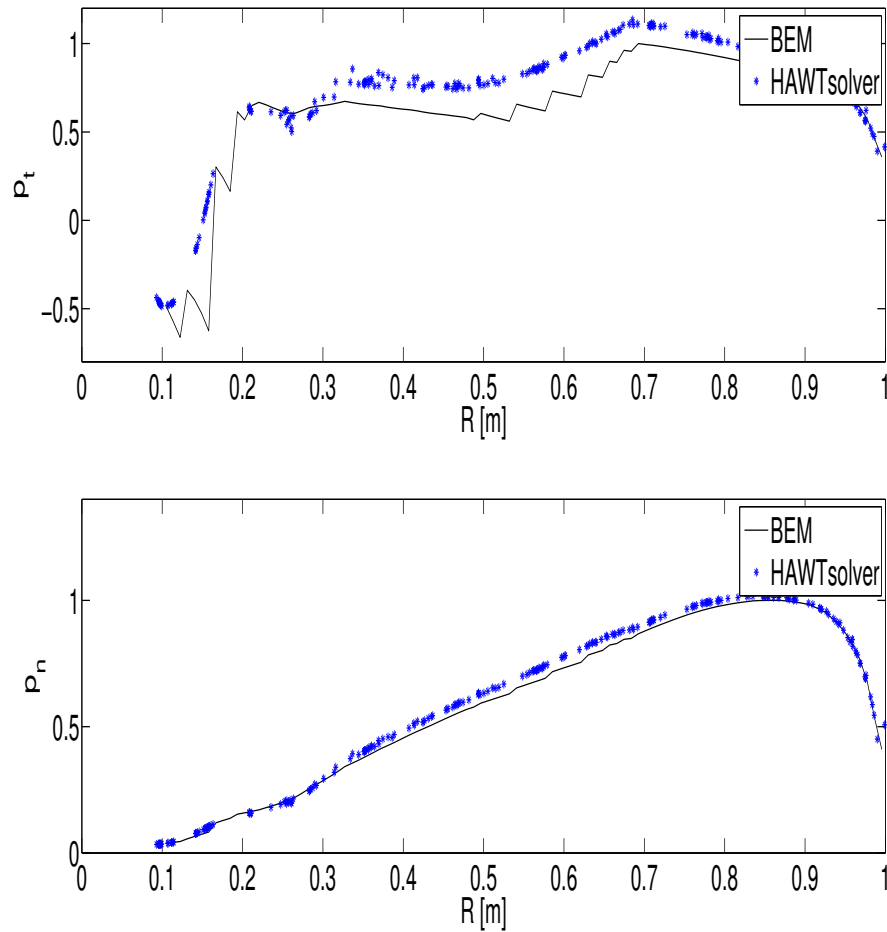


FIGURE 5.19: Blade loads for  $TSR = 9$  simulation case.

The first plot represents the load per unit length vs the blade radial position in the normal direction to the blade.

The second plot represents the load per unit length vs the blade radial position in the tangential direction to the blade.

# Chapter 6

## Conclusions and future efforts

This thesis work deals with the development of the Effective Velocity Model for wind turbines aerodynamics numerical simulation through an Actuator Line approach. It consists in the production of a working CFD code implemented in the open-source environment of OpenFOAM.

The proposed solver follows the fundamentals of the Actuator Line Method introduced originally in 2002 by J.N. Sorensen and W.Z. Shen from Technical University of Denmark [16]. The approach prescribes to not model the blade profiles in the computational domain, but their substitution with equivalent aerodynamic forces, function of the wind velocity. Thus, a correct estimation of the blade relative velocity is of course one of the key aspects of each aerodynamic model: the development of a new method composed the most important aim of the presented work.

As explained, existing codes do not supply a detailed study about the estimation of the relative velocity seen by the blade. Most part of researchers considers the velocity analytically calculated via the Blade Element Momentum or locally sampled. The Blade Element Momentum method suggests that the velocity on rotor plane could be calculated "a-priori", known mean wind inflow speed and relying on the axial and tangential induction factors. Critical aspects emerge when considering a non-steady flow condition, where a unique velocity value can not be representative of the overall incoming flow or considering that the rotating blades of the turbine cross different regions of the Atmospheric Boundary Layer, experiencing a strong variations in ve-

locity value. The alternative takes advantage of the knowledge of the full velocity field resolved by CFD and supports a local evaluation of the velocity relatively to the actual application force point, that induces the fluid deflection. From the bound vortex theory, generated lift defines the circulation intensity around the airfoil profile: existing CFD codes, like Sorensen's Ellypsis 3D or SOWFA of NREL [33], assume the velocity value in the exact vortex centre, i.e. the force application point. The critical issue of the local model consists in the numerical approximations brought by CFD or again, considering a non-steady incoming flow.

Our model arises between the Blade Element Momentum approach and the local model: like the first, velocity is detected upstream respect to the blade, but similarly to the local model, it aspires to catch the effective quantities investing the blade. These are the reasons supporting the introduction of the Effective Velocity Model introduced by the thesis work, based on the previous study of P. Schito from Politecnico di Milano [3]. Relying on the resolved velocity field, the model samples the velocity on a line placed upstream the force application point and perpendicular to the mean incoming flow direction. Velocity values detected on the line are then averaged, in order to obtain an accurate estimation of the true incoming velocity. Once calculated the velocity, aerodynamic forces can be calculated looking at the polar curves of the considered profile.

Initially it is considered the 2-dimensional Actuator Line problem, collapsed in the Actuator Force case. First of all, the validation of the Actuator Force relies on the similitude of the velocity field between the Actuator Force and the fully resolved airfoil simulations. This fundamental point has been good achieved letting the development of the successive work. Then a particular attention has been given to the definition of the regularization kernel function, a useful tool required to limit the non-physical numerical oscillations comparing in the wake of the Actuator Force. Deeper studies could be made in this direction to better understand the origin of this specific behavior and its limitation. At this point the Effective Velocity Model has been showed. The stationary case showed a good agreement between the Actuator Force simulation and the Fully Resolved Airfoil one, used as a benchmark, in terms of inserted force and generated wake. The 2-dimensional configuration

has been tested also under a non-stationary regime, imposing an oscillating flow condition at the inlet. Also in this case the matching between the fully resolved profile and the Actuator Force is clearly appreciable, even if the results are not as good as in the stationary case.

Tests and validations made about the Actuator Force, formed the base for the successive development of the new simulation code funded on the Actuator Line technique for an horizontal axis wind turbine rotor. This code, that contributes to enlarge the strict number of existing Actuator Line OpenFOAM codes, has been completely developed in the OpenFOAM style using C++ programming language. It has been built with particular attention to the objects orientation in order to be highly flexible, allowing for example to be quickly suitable for the simulation of vertical axes wind turbines. The code has been tested looking at different tip speed ratios and pitch angle conditions. Results have been compared both to experimental data coming from the wind tunnel experiences, and to collected outcomes of traditional Blade Element Momentum approach. It has been reached an overall good assonance between the expected and the obtained results, looking especially at the wind turbine performances and reproduction of the wake in the downstream region. This lets reasonable to suppose the goodness of the Effective Velocity Model, core of this thesis work in terms of an increase of the simulation quality.

## 6.1 Future efforts

Future efforts could be made in the direction of a higher validation of the proposed model, in particular referring to an incoming turbulent flow. Both 2-dimensional and 3-dimensional problems should be deeper studied refining the model that tends to predict a bit higher angle of attack inducing a overestimation of the torque and a underestimation of the thrust. It would be desirable the adoption of a very fine mesh to appreciate in detail the behavior and the performances of a modeled wind turbine and the evolution of the wake.

More attention should be also given to the improvement of the code efficiency, actually the solver runs yet on multiple processors, but the algorithm

is not very well optimized. The slowness of the code is due to the high amount of information that involved processors exchange and that could be reduced through a massive effort of optimization.

The last but not the least important effort would be an expansion of the simulation code integrating the aerodynamic aspects, subject of this thesis, with the aeroelastic ones and the structural problems typical of the wind turbines. Taking the advantages of the Effective Velocity Model that samples the velocity close to the blade, for the future it is important to remind that our Actuator Line code could greatly contribute to the development of a new aeroelastic-aerodynamic program, since it allows to record flow deflections function of the wind turbine structure displacements and vibrations. Just to make an example, the NREL plan integrating the SOWFA and the FAST codes [51] is of course a reference, since it proposes a complete tool to simulate the full behavior of wind turbines.







# Bibliography

- [1] Hansen M.O.L., *Aerodynamic of wind turbines*, Earthscan, 2008.
- [2] Leung D.Y.C., Yang Y., *Wind energy development and its environmental impact: a review*, Renewable and Sustainable Energy Reviews, 2012.
- [3] Schito P., Zasso A., Mastinu G., *Large eddy simulation of wind turbines: Interaction with turbulent flow*, Department of Mechanical Engineering - Politecnico di Milano - Milano - Italy, 2012. PhD Thesis.
- [4] GWEC, *Global Wind Report 2013 - Annual market update*, Global Wind Energy Council, [www.gwec.net](http://www.gwec.net), 2014.
- [5] EWEA, *2030*, The European Wind Energy Association, [www.ewea.org](http://www.ewea.org), 2013.
- [6] EWEA, *Design limits and solutions for very large wind turbines*, The European Wind Energy Association, [www.ewea.org](http://www.ewea.org), 2011.
- [7] Manwell J.F., McGowan J.G., Rogers A.L., *Wind energy explained: theory, design and application*, Wiley, 2009.
- [8] Versteeg H., Malalasekera W. *An introduction to computational fluid dynamics*, 2nd edition, Pearson Ed., 2007.
- [9] OpenFOAM, *The Open Source CFD Toolbox*, Version 2.2.2, [www.openfoam.org](http://www.openfoam.org), 2013.
- [10] Anderson J.D., *Computational Fluid Dynamics: The Basics with Applications*, McGraw Hill, 1995.

- [11] Cengel Y.A., Cimbala J.M., *Meccanica dei fluidi*, 2nd edition, McGraw Hill, 2011.
- [12] Von Karman T., *Twenty-fifth Wilbur Wright memorial lecture - turbulence*, Royal Aeronautical Society Journal, 1937.
- [13] Angiolini M., *Funzioni di parete adattive per il modello di turbolenza  $\kappa - \omega$* , Department of Aerospace Engineering - Politecnico di Milano - Milano - Italy, 2012. MSc Thesis.
- [14] Piomelli U., *Large-eddy simulation of turbulent flows. Part 1: Introduction*, Department of Mechanical and Materials Engineering - Queen's University - Kingston (Ontario) - Canada, 2010. Lectures.
- [15] Furbo E., *Evaluation of RANS turbulence models for flow problems with significant impact of boundary layers*, Teknisk-naturvetenskaplig fakultet - Uppsala Universitet - Uppsala - Sweden, 2010. MSc Thesis.
- [16] Sorensen J.N., Shen W.Z., *Numerical Modeling of Wind Turbine Wakes*, Journal of fluids engineering, 2002.
- [17] Troldborg N., *Actuator line modeling of wind turbine wakes*, Technical University of Denmark - Lyngby - Denmark, 2008. PhD Thesis.
- [18] Martinez L., Leonardi S., Churchfield M., Moriarty P., *A comparison of actuator disk and actuator line wind turbine models and best practices for their use*, American Institute of Aeronautics and Astronautics, 2012.
- [19] P.E. Eriksen, Krogstad P.A., *"Blind test" calculations of the performance and wake development for a model wind turbine*, Renewable Energy Journal, 2012.
- [20] Pierella F., *Blind Test 2 calculations for a two wind turbines in tandem arrangement*, Energy and Process Engineering, 2013.
- [21] Wu Y., Porté-Agel F., *Large-eddy simulation of wind-turbine wakes: evaluation of turbine parametrisations*, Boundary - layer meteorology, 2011.

- [22] Sorensen J.N., Carsten W.K., *A model for unsteady rotor aerodynamics*, Journal of fluids engineering, 1995.
- [23] Mikkelsen R., *Actuator Disc Methods Applied to Wind Turbines*, Department of Mechanical Engineering - Technical University of Denmark - Denmark, 2003. PhD Thesis.
- [24] Ivanell S., Mikkelsen R., Sorensen J.N., Henningson D., *Three dimensional actuator disc modelling of wind farm wake interaction*, EWEC, 2008.
- [25] Masson C., Smaili A., Leclerc C., *Aerodynamic Analysis of HAWTs Operating in Unsteady Conditions*, Wind Energy, 2001.
- [26] Ivanell S., Mikkelsen R., Sorensen J.N., Henningson D., *Analysis of numerically generated wake structures*, Wind Energy, 2009.
- [27] IEA Wind, *Final report of IEA Task 29, Mexnext (Phase 1): Analysis of Mexico wind tunnel measurements*, The International Energy Agency, 2012.
- [28] Simms D., Schreck S., Hand M., Fingersh L.J., *NREL Unsteady Aerodynamics Experiment in the NASA-Ames Wind Tunnel: A Comparison of Predictions to Measurements*, NREL, Technical report, 2001.
- [29] P.E. Eriksen, Krogstad P.A., *Experimental Results for the NOWITECH/NORCOWE Blindtest*, Energy Procedia, 2012.
- [30] Schepers J.G., Snel H., *Model Experiments in Controlled Conditions, Final report*, Energy Research Center of the Netherlands, ECN, 2007.
- [31] Porté-Agel F., Wu Y.T., Lu H., Conzemius R.J., *Large-eddy simulation of atmospheric boundary layer flow through wind turbines and wind farms*. Journal of Wind Engineering and Industrial Aerodynamics, 2011.
- [32] Phillips A.B., Turnock S.R., Furlong M.E., *Evaluation of manoeuvring coefficients of a self-propelled ship using a blade element momentum propeller model coupled to a Reynolds averaged Navier Stokes flow solver*, Ocean Engineering, 2009.

- [33] Churchfield M., Lee S., Moriarty P., *Overview of the Simulator for Off-shore Wind Farm Application (SOWFA)*, NREL, 2012.
- [34] Shen W.Z., Hansen M.O.L, Sorensen J.N., *Determination of the Angle of Attack on Rotor Blades*, Wind Energy, 2009.
- [35] Eleni D.C., Athanasios T.I., Dionissios M.P., *Evaluation of the turbulence models for the simulation of the flow over a National Advisory Committee for Aeronautics (NACA) 0012 airfoil*, Journal of Mechanical Engineering Research, 2012.
- [36] Menter F.R., *Zonal two-equation  $\kappa-\omega$  turbulence model for aerodynamic flows*, AIAA Paper 1993, 1993.
- [37] Abbott I.H., Von Doenhoff A.E., *Theory of Wing Sections*, Dover Publishing, New York, 1959.
- [38] Johansen J., *Prediction of Laminar/Turbulent Transition in Airfoil Flows*, Riso National Laboratory, Roskilde, Denmark, 1997.
- [39] Shyy W., Chen M.-H., Mittal R., Udaykumar H.S., *On the suppression of numerical oscillations using a non-linear filter*, Journal of Computational Physics, 1992.
- [40] Shen W.Z., Sorensen J.N., Zhang J.H., *Actuator Surface Model for Wind Turbine Flow Computations*, Proceedings of European Wind Energy Conference, 2007.
- [41] Airfoil Tools, [www.airfoiltools.com](http://www.airfoiltools.com).
- [42] EN 1991-1-4, *Eurocode 1: Actions on structures - Part 1-4: General actions - Wind actions*, European Union, 2005.
- [43] Gharali K., Johnson D.A., *Dynamic stall simulation of a pitching airfoil under unsteady freestream velocity*, Journal of fluid structures, 2013.
- [44] Dyrbye C., Hansen S.O., *Wind loads on structures*, 2ed. Wiley, 1999.

- [45] Argentini T., *Modellazione nel dominio del tempo delle forze aerodinamiche non lineari su impalcati di ponti*, Department of Mechanical Engineering - Politecnico di Milano - Milano - Italy, 2007. PhD Thesis.
- [46] Shinozuka M., *Simulation of stochastic processes by spectral representation*, Applied Mechanics Reviews, 1991.
- [47] Bottasso C.L., Campagnolo F., Croce A., Maffenini L., *Development of a Wind Tunnel Model for supporting research on aero-servo-elasticity and control of wind turbines*, 13th International Conference on Wind Engineering, Amsterdam, The Netherlands, 2011.
- [48] Capponi M., *Analisi e miglioramento delle caratteristiche aerodinamiche di un modello di aerogeneratore per prove in galleria del vento*, Department of Aerospace Engineering - Politecnico di Milano - Milano - Italy, 2011. MSc Thesis.
- [49] Shen W.Z., Zhu W.J., Sorensen J.N., *Actuator line/Navier-Stokes computations for the MEXICO rotor: comparison with detailed measurements*, Wind Energy, 2012.
- [50] Mikkelsen R. *Actuator Disc Methods Applied to Wind Turbines*, Department of Mechanical Engineering - Technical University of Denmark - Lyngby - Denmark, 2003. PhD Thesis.
- [51] Jonkman J.M., Buhl M.L. Jr., *FAST User's Guide*, NREL, [wind.nrel.gov/designcodes/simulators/fast/](http://wind.nrel.gov/designcodes/simulators/fast/), 2005.